# DEPOSITION AND CHARACTERIZATION OF METAL DOPED DIAMOND LIKE CARBON (ME(Ti,Nb)-DLC) FILMS

by

Deniz Uğur

B.Sc. in M.E., Boğaziçi University, 2005

Submitted to the Institute for Graduate Studies in
Science and Engineering in partial fulfillment of
the requirements for the degree of
Master of Science

Graduate Program in Mechanical Engineering

Boğaziçi University

2007

*Anneme, babama ve kardeşime...*

# ACKNOWLEDGEMENTS

Among many thanks, I'd like to express my gratitude to my thesis advisor Prof. Dr. Sabri Altıntaş, who provided me support and guidance all through this project. Besides his academic supervision, he has been an inspiration to me with his insight, experience and wisdom.

I must also thank Prof. Dr. İhsan Efeoğlu for his unlimited support in all the experimental studies of this thesis. Without his supervision in the collaborative research of TUBITAK MAG 105M190 project, it wouldn't be possible to conduct such a detailed study in one year.

Also the contribution of Prof. Dr. Sezai Saraç from Chemistry Department of İstanbul Technical University for helping me to draw qualitative conclusions from XPS spectra is deeply appreciated.

I'll always remember the support of my dear colleagues, who made this study possible by sharing their time and friendship with me. They lifted my mood with their joy and companionship, even in the most desperate times.

Finally to my family... It is for sure that saying "thank you" will not suffice to express my gratitude, but I want to thank them for being there for me in every trouble I face, supporting me in every possible way, sharing my happiness when I succeed and also for always trusting and believing in me when I stumble. This study would never have been successful without their mere presence.

# ABSTRACT

## DEPOSITION AND CHARACTERIZATION OF METAL DOPED DIAMOND LIKE CARBON (ME(Ti,Nb)-DLC) FILMS

In today's world, sustainable development and green technology concepts are pronounced more than ever, which force tighter efficiency measures and implementation of energy saving solutions to every applicable system. Wear and friction causing a significant loss of energy and material, is the foremost important source of efficiency loss. This thesis study was conducted to deposit hard, wear resistant and low friction coefficient thin films on high speed steel substrates to reduce friction and wear. This purpose was accomplished by the growth of diamond like carbon films (DLC) doped with titanium and niobium, by pulsed-dc closed field unbalanced magnetron sputtering (CFUBMS) method. Resulting coating characterizations were carried out in four different aspects, such as; the structural characterization was composed of scanning electron microscopy (SEM) and surface roughness studies, compositional characterization was composed of x-ray diffraction (XRD) and x-ray photoelectron spectroscopy (XPS) studies, tribological characterization was composed of pin on disc (POD) and adhesion scratch tests and finally, hardness characterization was composed of micro and nanohardness measurements. Resulting coatings presented a dense structure, accompanied with slight columnar growth and were seen to have moderate friction values, high wear resistance and high hardness.

# ÖZET

## METAL KATKILI ELMAS BENZERİ KARBON FİLMLERİN (ME(Ti,Nb)-DLC) BÜYÜTÜLMESİ VE KARAKTERİZASYONU

Günümüzde, daha yüksek verimlilik değerlerini ve uygulanabilir her sistemde enerji tasarrufunu öne süren yeşil teknoloji ve sürdürülebilir kalkınma kavramları, eskisinden çok daha fazla vurgulanmaktadır. Ciddi bir malzeme ve enerji kaybına sebep olan sürtünme ve aşınma, verimlilik kayıplarında en önemli kalemi oluşturmaktadır. Bu tez çalışması, sürtünme ve aşınmayı azaltmak maksadıyla yüksek hız çeliği numunelere, aşınma dayanımı yüksek, sert ve düşük sürtünme katsayılı ince filmlerin kaplanmasını amaçlamaktadır. Kaplama için darbeli-dc kapalı alan dengesiz magnetron sıçratma yöntemi kullanılmış, neticede titanyum ve niyobyum katkılı elmas benzeri karbon filmler üretilmiştir. Elde edilen filmlerin karakterizasyonu dört farklı yoldan takip edilmiştir, şöyle ki; yapısal karakterizasyon, taramalı elektron mikroskop (SEM) ve yüzey pürüzlük incelemeleriyle, bileşim karakterizasyonu, x-ışını kırınım ölçer (XRD) ve x-ışını fotoelektron spektroskopisiyle (XPS), tribolojik karakterizasyon, aşınma ve çizik testleriyle ve son olarak sertlik karakterizasyonu da mikro ve nano sertlik ölçümleriyle tamamlanmıştır. Elde edilen kaplamalarda, hafif kolonsal bir büyümenin olduğu yoğun bir yapı gözlemlenmiş, yüksek aşınma dayanımı, yüksek sertlik ve orta seviyede sürtünme katsayısı değerleri ölçülmüştür.

# TABLE OF CONTENTS

# LIST OF FIGURES

# LIST OF TABLES

# LIST OF SYMBOLS/ABBREVIATIONS

| | |
|---|---|
| $\mu$ | Friction Coefficient |
| $\mu$s | Microsecond |
| $K$ | Wear Rate |
| kHz | Kilohertz |
| $L_c$ | Critical Load |
| mTorr | Militorr |
| $R_a$ | Average Roughness |
| V | Voltage |

| | |
|---|---|
| at.% | Atomic per cent |
| *a-C* | Amorphus Carbon |
| a-C:H | Hydrogenated Amorphus Carbon |
| DC | Direct Current |
| Me-DLC | Metal Doped Diamond Like Carbon |
| *ta-C* | Tetragonal Amorphus Carbon |
| ta-C:H | Tetragonal Hydrogenated Amorphus Carbon |
| wt.% | Weight per cent |

# 1. INTRODUCTION

Our everyday life relies on materials in every aspect. Every manufacturing process, engineering system, machine or even the simplest tool is based on the use of materials in one way or another. Most of the time, the critical point of the use occurs in the interaction of two members in contact, highlighting the importance of the surfaces. Since the time of Leonardo da Vinci (1452-1519), who was arguably the first engineer to study friction and wear in detail, surface and coatings technology have become an important branch of modern surface sciences and engineering [18].

While in use, surfaces are prone to different extreme conditions, causing extensive wear, and corrosion. In industrialized countries, 30 per cent of all energy generated is ultimately lost through friction. In the highly industrialized countries losses due to friction and wear are put at between 1 and 2 per cent of Gross Domestic Product [19]. This incredible waste of materials, labor (in terms of effort put on workpieces) and time, led the researchers to look for a solution this issue. This research discipline is terminologically expressed as tribology, which contains the studies of adhesion, friction, lubrication and wear [20]. Focus of tribology is to increase the wear resistance of products and reduce their coefficients of friction, without impairing the characteristic properties (such as strength, toughness, ductility, etc.) of the materials much, or if possible, without impairing at all.

When considering wear resistance, it must always be carried in mind that this is a system dependent property. No matter how much the frictional properties are enhanced against one counterpiece, reached values are prone to change when the material in contact is changed due to different tribochemical processes occurring. Quoting the information supplied by de Hosson, it is possible to summarize the process, such as:

> "As a general rule, wear is determined by the interplay of two opposing properties: ductility and hardness. Wear can be reduced by modifying the surface layer in such a way that it acquires higher ductility, so that greater plastic deformation can occur without particles breaking off. Soft surface layers can be very effective in reducing wear due to delamination. Resistance to wear by abrasion,

> on the other hand, is then low. However, wear can also be reduced by making the surface layer harder. Then again, increasing hardness also means an increase in the elasticity strain limit and a reduction in ductility, leading to a lowering of fatigue resistance and hence to brittle failure. The characteristics of the system (i.e. whether the wear is caused by delamination or abrasion) determine which of the surface engineering methods should be chosen [19]."

To understand this mechanism, it is important to study friction and wear types. Although friction between objects is a matter of everyday experience, a universal agreement regarding what exactly causes friction still does not exist [21].

To the pioneers in tribology, one counts besides Leonardo da Vinci, Guillaume Amontons (1663-1705), John Theophilius Desanguliers (1683-1744), Leonard Euler (1707-1783), and Charles-Augustin Coulomb (1736-1806). These pioneers brought tribology to a standard, and its laws still apply to many engineering problems today. Some of their findings are summarized in the following three laws, applying to dry friction cases:

- The force of friction is directly proportional to the applied load. (Amonton's 1st Law)
- The force of friction is independent of the apparent area of contact. (Amonton's 2nd Law)
- Kinetic friction is independent of the sliding velocity. (Coulomb's Law) [20]

The evolution of friction concept began with the proposal of Desanguliers (1734), stating that adhesion is an element in the friction process. Since friction was independent of the contact area, this hypothesis was directly rejected at first. This conflict was resolved with the introduction of the real area concept (see figure 1.1), where the true area of contact is defined as being composed of a large number of small regions of contact, or asperities, where atom-to-atom contact takes place [20, 1].

In 1950, Bowden and Tabor showed that the force of static friction between two sliding surfaces is strongly dependent on the real area of contact [22]. A very important outcome of their work led to the asperity contact theory of friction, which

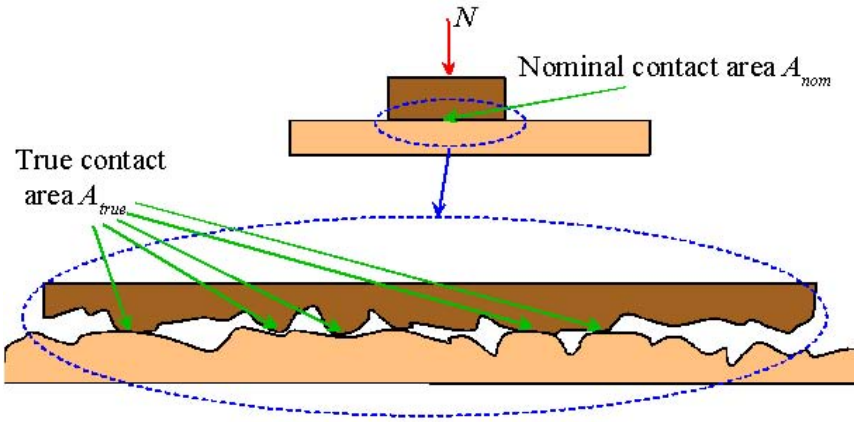


Figure 1.1. Schematic representation of true contact area [1]

is their detailed discussion about adhesive wear. In contrast to abrasive wear, which applies when a hard and rough surface slides against a softer surface, in adhesive wear, asperity junctions plastically deform above a critical shear strength that depends on the adhesive forces of the two surfaces in contact. Assuming that during a frictional sliding process, a fully plastic flow situation arise at all of the asperities, friction is found to change linearly with the applied load, as demanded by Amonton's first Law [20].

Instead of assuming a constant number of asperities as Bowden and Tabor did, Archard assumed a load dependent number of asperities. His theory is visited in detail in Section 4.3.1, while studying the pin on disc wear test procedure. With this assumption, the controversy between the elastic multiple asperity hypothesis and Amonton's first law could be resolved. Greenwood and Williamson further improved the method with a Gaussian and exponential distributions of asperities [20].

Different wear mechanisms are summarized in Table 1.1. In this table, both the causes of wear and methods of preventing them are supplied [13]. In the coatings of this study, as presented in the results chapter, there is a combination of both adhesive and abrasive wear. The former one is the result of the asperity contact under pressure, whereas the latter is due to the wear particles' abrasive effect.

Table 1.1. Common wear mechanisms of HSS cutting tools, their cause and how to fight them [13]

| Wear mechanism | Cause of wear | Counteractive tool properties |
|---|---|---|
| Abrasive wear | Hard particles or other hard phases in the work material remove material by a ploughing action | High matrix hardness, large volume of hard phases, hard coating |
| Mild and severe adhesive wear | High cutting speed generates high tool surface temperatures that facilitate strong adhesion between work and tool materials. The worst situation prevails for tough, ductile and chemically reactive work materials with low thermal conductivity | Smooth surface, sharp edge, high hot hardness, high thermal conductivity, chemically inert (anti sticking) coating |
| Plastic deformation | High cutting speed generates excessive edge temperatures in combination with high loads | High hot hardness, high thermal conductivity |
| Fracture and fatigue | Interrupted cutting, especially in combination with high cutting speed and use of cutting fluid, a tough and ductile work material. Use of insufficiently sharp tool edges | Smooth tool surface, high fracture toughness promoted by a defect free HSS with a fine grained structure of both matrix and hard phases |

Besides the mechanisms of wear, frictional properties are also important. In order to decrease the coefficient of friction, the rationale behind the mechanisms lowering friction must be understood. In a research conducted by Brendle and Colin, in 1991, it was found that during the initial sliding of surfaces of two solid bodies over each other there is a gradual increase in friction force and frictional temperature. In this phase, no material transfer from one surface to the other is observed. Only at the frictional maximum are the particles transferred [23].

In another research conducted by Langlade et al. in 1994, following Brendle and Colins's work, the tribologic properties of two surfaces in contact were more thoroughly studied. It was noted that after the beginning of the formation of the transfer layer, friction force presented a decreasing trend until a stable level is reached. Depending on the type of material, a suitable transfer film is formed which grows to a test condition dependent thickness [24]. After the introduction and explanation of the transfer layer term in the literature, solid lubrication phenomena and characterization of the tribologic properties were much easily provided.

In 2001, Holinski studied the sliding of solid bodies of different materials over each other and found out that the friction layer is formed on the surface of the softer components. This friction layer governed tribological properties like friction coefficient, friction fluctuation, and wear rate. After run-in this transfer layer was found to be in sliding contact with the friction layer of the softer component. By tribological stress and also at higher temperatures diffusion takes place in metals close to the surface, which results in changes of metallurgical structure [25]. These changes lead to fractures and damages at metal surfaces.

It is possible to alter the mechanical and tribological properties, by simply applying hardening procedures on the surface bulk material itself. By employing laser hardening, electron beam hardening and shot peening, the outer shell of a substrate could be hardened, where there exists also other thermochemical treatments, such as nitriding, boriding, carburizing and ion implantation [19].

In a work conducted by Zhiyong He et. al. in 2006, surface modification of $Ti_6A_4V$ by plasma niobium alloying process was carried out, with the purpose of enhancing the corrosion, as well as the oxidation behavior of the substrate. After sputter cleaning, *Nb* atoms were deposited and the *Ti-Nb* alloy layer was formed through the diffusion process of *Nb* in the substrate. In order to get higher surface hardness, carburizing was conducted as post treatment. Since *Nb* possessed infinite solubility with titanium, the modified layer was a solid solution of *Nb* in *Ti* with gradient concentration profile and no distinctive interface between the layer and the bulk of the material. The modified layer, by being coherent and thick (over 50 $\mu$m), provides an effective support to the surface to sustain high normal or shear loads and prevent cracking or spalling [26]. Oxidation resistance by *Nb* alloying is also significantly improved, which is explained by the doping effect of high valence *Nb* ions in crystal, which suppressed the inward diffusion of oxygen and therefore the growth of oxidation layer [27].

The focus of this study whereas, relies on the choice and application of coatings to achieve improved properties on substrates. The selection and design of tribological coatings ensuring both protection against wear and low friction coefficient can be very complex. In fact, three basic aspects must be considered in the selection of a suitable tribological coating:

- The technical function of the moving technical assembly
- The operating conditions, including load, sliding velocity, temperature and nature of the ambient gas
- Expected type of friction, wear and lubrication mechanism [28]

Today, for achieving these purposes, application of hard coatings are practiced. The most basic types of these coatings constitute carbides, borides, nitrides and oxides, which are very hard and possess high chemical and thermal inertness under challenging environments. Some of these materials are tungsten carbide ($WC$), titanium nitride ($TiN$), titanium aluminum nitride ($TiAlN$), niobium nitride ($NbN$), chromium nitride ($CrN$), titanium diboride ($TiB_2$) coatings, whereas there are still an enormous amount of choices of nitrides and carbides combined together that are not be mentioned here.

Currently the most well-known and widely applied of these coatings in the industry is the *TiN* coatings, studied in detail by Arslan and Efeoglu in 2004. *TiN* was stated to demonstrate extreme chemical stability, high corrosion resistance to strong acids along with low wear and is commonly used in cutting tools, sliding applications and semiconductor technology as a barrier layer and for decorative purposes [29]. *TiN* films also display a high resistance against fast wear at high cutting speeds [30].

While *TiN* coatings present 24 GPa of hardness and a coefficient of friction around 0.55, *CrN* coatings present a lower coefficient of friction (cof) (0.3), which is a desired property in low wear coatings, but also a decreased hardness (18 GPa) [6]. *CrN* coatings of nano grain size were investigated by Mayrhofer et al. in 2004, both in single (*CrN*) and dual phase (*CrN*-$Cr_2N$) and found to present extremely improved hardness values (39 GPa), when grain size is lowered [31]. They've also conducted studies on *TiAlN* and *Ti-B-N* phases, with the focus on $H^3/E^2$ ratio, indicator of resistance to plastic deformation. It was evident that decreasing the grain size and forming nanocomposite structures were efficient in reaching higher hardness values and better wear resistances [32].

Regarding *Cr* effect as a dopant, Gassner et al. in 2005, conducted a detailed study on *Cr-C/a-C:H* coatings, where *a-C:H* stands for amorphus carbon. Again in this study, it wasn't possible to combine high hardness with low friction; high hardness (48 GPa) resulted in high cof (0.5) and lower hardness values (10 GPa) resulted in lower friction values (0.15), requiring a further optimization study [33].

*WC* coatings are also widely used for protection against wear, erosion damage, and high temperature oxidation where highly successful applications of thin, vacuum grown *WC* coatings in sliding wear protection for cutting and forming tools is practiced. The drawback of these coatings however is the high friction coefficients they present (0.5 - 0.6) [34]. In a study conducted by Voevodin et. al in 1999, *WC-Co* nanosized agents are investigated and their contributions to strength and wear resistance in other host matrix materials in studied. Used in diamond like carbon matrices, *WC-Co* provided the system to present cof values around 0.2.

There are also $TiB_2$ coatings employed for achieving high wear resistance, with hardness value of around 25 GPa, elastic modulus over 500 GPa, friction coefficient measured as 0.9, accompanied with high thermal and chemical stability [35]. Typical applications of $TiB_2$ include high-performance cutting and forming tools, high corrosion resistance coatings for molten metal containers, and thermal barriers in fusion chemical reactors [36]. Shen et al. in 2006 studied the combined effect of $TiN$-$TiB_2$ nanocomposite (grain size: 4 nm) coatings of enhanced strength and hardness. It was observed that the increase of Boron in the sputtering chamber inhibited $TiN$ growth and promoted the encapsulation of $TiN$ by $TiB_2$, thus limiting the grain growth and increasing the strength [37]. Similar encapsulation was also practiced for metallic nanoclusters in Boron and Carbon nitride thin films, in the study of Babonneau et al., 2006 to yield better wear resistances [38]. There exist further studies on boron carbide ($B_4C$) and boron carbonitride ($B_xC_yN_z$) thin films, reporting 30 GPa and 20 GPa of hardness respectively [39] in the literature.

In a 2003 dated work, hard niobium nitride films were deposited onto high speed steel substrates (std. no. 1.3207 S10-4-3-10) using reactive magnetron sputtering (M.Fenker et. al., 2003). The film thicknesses were measured 2.98 $\mu$m on the average. It was found that, good adhesion with $Lc_2$ values in the range of 60-75 N were obtained for $NbN_x$ coatings deposited at higher nitrogen pressures ($\geq 3.2 \times 10^{-2}$). Reported microhardness values for $NbN_x$ coatings were in the range of 20-45 GPa, whereas in this study, they showed plastic universal hardness in the range of 34000-53000 N/$mm^2$. It was also noted that predominantly (200) oriented $\delta$-$NbN$ coatings exhibit much lower compressive film stresses than (111) oriented coatings (-3 to -5 GPa, compared to -9 to -12 GPa)[40]. There were also researches conducted on $Nb$ and $NbC$ films. In Barzilai's work, it was desired to convert $Nb$ layers into $NbC$ by annealing at different temperatures. Hardest coatings were coated at 50 V of bias, resulting in 13 GPa [41]. It was also given in the literature that $NbC$ layers deposited on AISI M2 steel presented better resistance to wear than on AISI H13 steels [42].

## 1.1. Diamond Like Carbon Structure

Carbon, with the symbol $C$ and atomic number 6, is considered to be "the basis of the chemistry of all known life" due to its abundance in the universe. There are many allotropes of carbon, such as fullerenes, nanorods, amorphous carbon, among which, diamond and graphite forms are the most well-known ones. This group of materials does not really fall within any of the traditional metal, ceramic, polymer classification schemes [43]. Figure 1.2 shows the structures of various allotropes of carbon, which are consecutively;

a) Diamond
b) Graphite
c) Lonsdaleite
d) C60 (Buckminsterfullerene)
e) C540 (see Fullerene)
f) C70 (see Fullerene)
g) Amorphous carbon
h) Single-walled carbon nanotube

In Figure 1.2, the structure of graphite, giving rise to its low coefficient of friction is clearly seen. Graphite has good lubrication performance in air due to its layered structure that allows wear via sliding and shearing of individual layers [44].

Diamond however, is a metastable carbon polymorph, where each carbon bonds to four other carbon atoms and these bonds are totally covalent [43]. The physical properties of diamond make it an extremely attractive material. In addition to being the hardest material known to mankind, diamond provides some of the lowest friction coefficients to sliding tribological interfaces when tested in open air. This combination of extreme hardness (and hence wear resistance) and ultralow friction in one material is very rare in the field of tribology and it renders diamond ideal for a wide range of tribological applications [45], however it must be noted that this tribological behavior is significantly altered when the test environment is changed. The friction coefficient

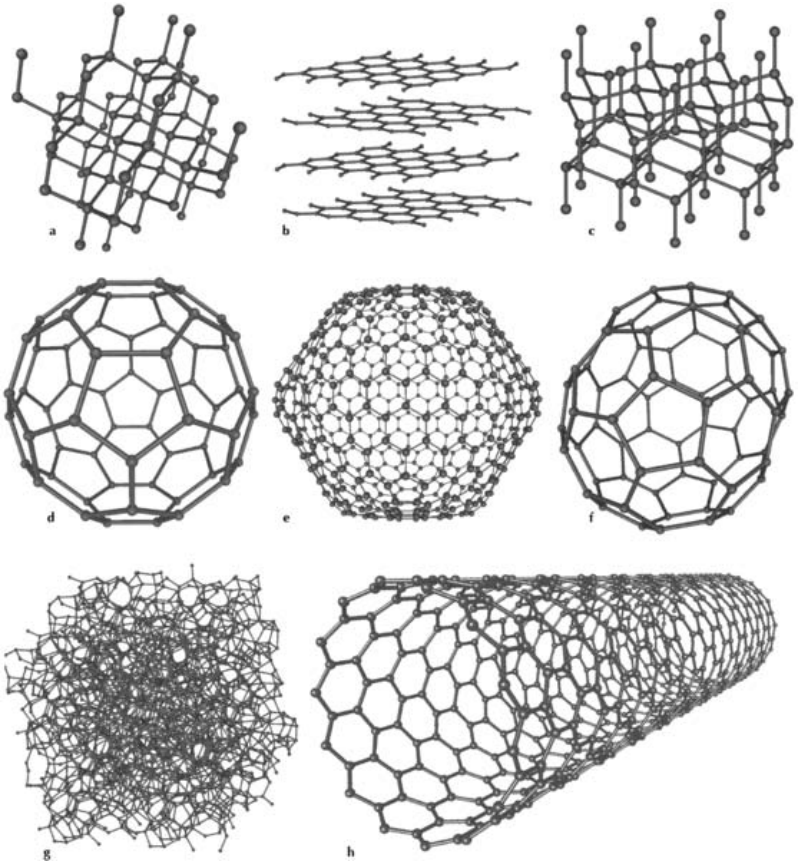

Figure 1.2. Eight allotropes of Carbon, by Michael Ströck [2]

of diamond depends strongly on the environment and is mainly controlled by surface dangling bonds. Diamond has a low friction coefficient in humid air or dry nitrogen, due to a contaminant layer of low shear strength [46].

Diamond, which possesses a very low electrical conductivity, also presents an unusually high thermal conductivity for a nonmetallic material due to the strong interatomic bonds, is optically transparent, shows anisotropic effects and has a high index of refraction. Diamond films are widely applied in industrial machining applications, mechanical seals, MEMS, woodworking tools, tab tools, push pins, high-precision microdrills, surgical blades, wire-drawing dies, and various wear parts that are used against erosion and abrasion (e.g., jet nozzles) [45, 46].

Tribology researchers were amazed with the superior properties diamond exhibits and have been conducting studied on developing structures mimicking diamond films for a long time. These researches gave rise to the development of DLC structures. DLC

films represent a noteworthy example of thin films whose properties can be varied over a wide range of structures and compositions. The tribological behavior of these films strongly depends on the deposition technique [45] and the formation of interfacial transfer layer formed during friction [46]. There is a vast literature published in DLC films area, where DLC films are well known for their outstanding properties such as high hardness approaching that of diamond, high wear resistance and a low friction behavior, accompanied with chemical inertness, infrared transparency, low thermal expansion, high thermal conductivity and high electrical resistivity [11, 47, 48, 46, 45, 49, 50, 51, 52]. This high chemical inertness also provides the DLC structure to be less vulnerable to the chemical attack of aluminum when compared to many other coatings [53, 54]. Another promising property that DLC films demonstrate, is full biocompatibility in medical applications such as soft contact lenses, medical guidewires, catheters and many other implants, such as orthopedic and cardiovascular components [55].

The general term "DLC" describes hydrogenated and hydrogen-free metastable amorphous carbon materials, prepared by a wide variety of PVD and CVD techniques. The DLC terminology is commonly used to designate the hydrogenated form of amorphous carbon films, in spite of containing an $sp^3$ fraction generally smaller than 50 per cent [45]. From a classification proposed by Robertson depicted in Figure 1.3, DLC may be divided into four categories, the *a-C* (amorphus carbon) and *a-CH* (hydrogenated amorphus carbon) with a predominance of $sp^2$ bonds, and the *ta-C* (tetragonal amorphous carbon) and *ta-CH* (hydrogenated tetragonal amorphous carbon) with a predominance of $sp^3$ bonds [3].

First study of thin carbon films start with the research of Aisenberg and Chabot in 1971. They developed an ion-beam deposition technique and used it to deposit thin films of insulating carbon on room-temperature substrates. It was established that the carbon films deposited using this technique were insulating and had the following characteristics similar to that of carbon in the diamond form: (1) transparency, (2) index of refraction greater than 2.0, (3) highly insulating, (4) able to scratch glass, (5) resistant to hydrofluoric acid for long periods of time, (6) at least partially crystalline

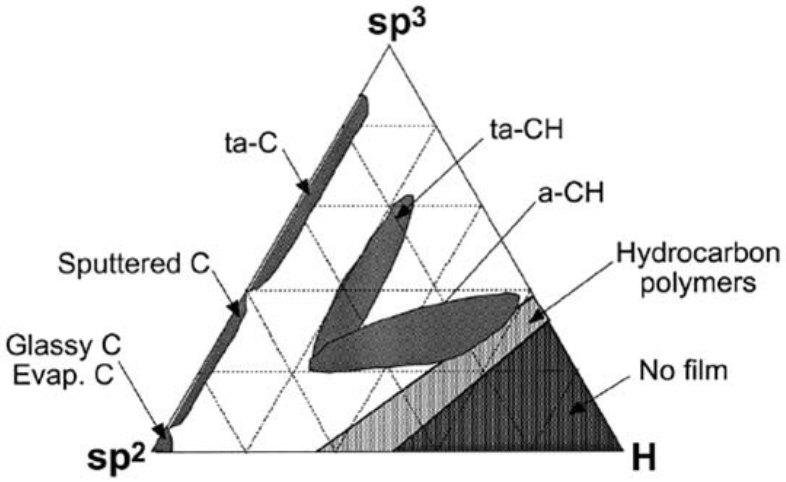


Figure 1.3. Pseudo-ternary phase diagram showing various forms of DLC [3]

and with a lattice constant similar to diamond as demonstrated by x-ray diffraction, (7) dielectric constant between about 8 and 14 (diamond is 16.5). This work is regarded as the first deposition of DLC coatings [56].

There has been loads of research conducted on tribological properties of DLC films with the use of lubricants. In a work of Stallard et al. in 2004, three different carbon-based coatings were tested in three different environments; normal atmospheric conditions, distilled water and a low viscosity oil. Dry testing results were good for all coatings, where in water, hydrogenated coatings suffered from severe wear. Hydrogen presence in these films had a detrimental effect on the wear behavior in water-lubricated conditions. Oil behavior was similar to that observed in dry air [57]. In 2003, Podgornik et. al. investigated the influence of conventional extreme-pressure (EP) and anti-wear (AW) additives on the tribological performance of hard low-friction coatings in the boundary lubrication regime. It was found that the standard EP and AW additives gave up to 25 per cent better frictional and wear properties of DLC coated substrates, as compared to pure Poly-Alpha-Olefin (PAO) oil, where the type of the combination of the additives had a strong influence on the tribological behavior of DLC coated surfaces [58].

It was observed that different DLC films with varying hydrogen contents demonstrated different tribologic behavior under wear and adhesion tests conducted in ambi-

ent air and under gas atmospheres. In 1998, Donnet et. al. investigated the influence of oxygen and water vapor on the tribology of hydrogenated DLC coatings, which exhibited ultra low friction (COF below 0.01) in ultrahigh vacuum (UHV). It was found that, oxygen didn't change the ultra low friction behavior of DLC observed in UHV, on the other hand, water vapor drastically changed the COF at pressures above 0.5 hPa ( RH = 2%) from about 0.01 to more than 0.1. They used a hydrogenated DLC film deposited by PACVD on a silicon wafer of 42 per cent hydrogen content using $C_6H_{12}$ and a carbon $sp^2$ hybridization of 39 per cent. It is proposed that water vapor may be inhibiting the growth of the transfer film, whose thickness does not increase and remains insufficient to allow a COF decrease in the 0.01 range [50].

Erdemir et al. [59], have also reported friction coefficients of 0.005 or less under pure dry $N_2$ or $Ar$ atmospheres, endured for millions of sliding cycles on a pin-on-disc machine for only 1 to 2 $\mu$m thick coatings. They've studied various gas atmospheres and found that due to the higher hydrogen-to-carbon ratio in methane films, causing hydrogen to stabilize the $sp^3$-bonded carbons and provide a much diamond-like character rather than graphite, less frictional scatter and much lower COF's are attained when compared to acetylene deposited films. It is also stated that as long as the source gas is the same, the difference in deposition process didn't seem to cause major differences in tribological performance. Wear being extremely low under dry $N_2$ environment is also noted, compared to open air testing [59].

Investigations on hydrogen-free hard carbon films ($a$-$C$) and amorphous hydrogenated carbon films ($a$-$C$:$H$) under different tribological conditions, such as dry (50 % RH), water and oil lubricated environments were conducted by Ronkainen et al. in 1998. They found that DLC films exhibited a low coefficient of friction in dry sliding conditions. COF ranged between 0.15-0.22. Hydrogen-free coatings had a COF as 0.03 in water-lubricated conditions; however, water lubrication was severe for hydrogenated films causing an early failure. The performance of $a$-$C$:$H$ coatings could be improved with titanium alloying for aqueous environments. Tribological performance of DLC films could be further improved by oil-lubrication up to 10-40 per cent drop of COF [60].

In 2000, Donnet et. al. [48] conducted a more detailed study on the tribological properties of DLC films with different hydrogen contents, where it was stated that there existed a little information on non hydrogenated films, when compared to hydrogenated derivatives. Experiments were performed under ultrahigh vacuum or in an atmosphere of pure hydrogen or argon. High steady state friction (COF: 0.6) is observed for the lowest hydrogenated and mostly $sp^2$ bonded DLC film in UHV. Superlow steady state friction (COF in the millirange) is observed both for the highest hydrogenated film (40 at. per cent) in UHV (due to the weak Van der Waals interactions between flexible carbon chains) and for the lowest hydrogenated film in an atmosphere of hydrogen (10 hPa) [48].

In a following study, conducted by Shi et. al., 2005, the deposition of highly hydrogenated carbon films by modified, inductively coupled plasma (ICP) assisted chemical vapor deposition technique was studied, whose resultant films' hydrogen content approaches 60 at.%. It was verified that higher hydrogen content led to more compliant and softer films [61].

To summarize the effect of hydrogen on tribological behavior of DLC, it is possible to state that superlow friction coefficients could be attained for highly hydrogenated DLC films in UHV conditions. For brief periods following running-in, extremely low friction coefficient values ($\mu \leq 0.01$) are possible to be reached, even better wear and friction coefficients are attained when the counterbody is coated with DLC too [62]. Drawbacks are the drastic increase of friction and wear with the presence of water vapor and the limited lifetime of these coatings under vacuum.

The effect of coating both surfaces of the tribosystem is studied in detail in the research of Kennedy et al. in 2003. Here it was published that the friction between the steel ball and steel flat was reduced by between 75 and 85 per cent (from $\mu \approx 0.5$ to 0.1), if one of the steel specimens was coated with DLC. A further friction reduction to about $\mu = 0.08$ can be attained by coating both sides of a steel/steel couple [63].

On the contrary, for non-hydrogenated DLC films, low friction values could only be attained under hydrogenated and humid atmospheres. Presence of water vapor in the tribosystem is essential for low cof and wear rates of the non-hydrogenated DLC coatings. A prospective method for further decreasing the wear is by letting the tribosystem to run-in initially in ambient air and then pumping down the system to operate under vacuum. By this way, it was even possible to reach friction coefficients of 0.006-0.02 level [64].

When high temperature tribologic behavior of DLC films is investigated, it was found that the wear resistance was poor. A solution was proposed as to increase the bias voltage and decrease the flow rate to improve coating stability and wear resistance [65]. In the study of Konca et al. in 2006, high temperature DLC literature was reviewed. Authors reached the conclusion that, DLC coatings with significant $sp^2$ bonding could maintain low friction at elevated temperatures only if they include a significant amount of hydrogen in their structures. Further information about high temperature effects are supplied in the literature and Konca's work [65, 66].

DLC films exhibit a wide range of structure, composition, and attractive mechanical, optical, electrical, chemical, and tribological properties [45]. Such a wide range of film structures and composition and the diversity of methods used for DLC film deposition, provide the flexibility to tailor their properties according to specific needs and applications. However, there are still many problems, limiting the use and applicability of DLC films. High internal stresses, porous structure and poor adhesion are among the most important of these problems.

To overcome the problems of low adhesion, different coating concepts have been proposed, such as the use of a multilayer coating and a chemically graded interlayer between the substrate and the DLC films [67, 68, 69]. This method was found to be effective in the study of Ueng et al. in 2006 [67], conducted on *Ti/TiN/TiCN* functionally gradient composite interlayers and also the study of Ha et al. in 2006 [68]. Chicot et al in 2005 have proposed that a convenient annealing procedure must be carried out to improve adhesion properties, by stress relieving [70], which was also

practiced by Yu et al. in 2006 [71]. In the same manner, Lattemann et al., 2006 studied a novel deposition method to deposit coatings with decreased internal stress. They've applied a post-annealing treatment in combination with this novel deposition method, of which the whole process enabled to lower the film stress from -29 GPa to -3 Gpa [72]. Still the most common method is the deposition of an interlayer, which is generally done by sputtering *Cr*, *Ti*, *Zr*, *W*, *Nb* or *WC* to coat a thin layer between the coating and the substrate. An interlayer of *Nb* was used to improve the adhesion of diamond-like-carbon (DLC) coatings on stainless steel substrates, which are used in razor blades [73]. In a study conducted by Fan et al. in 2006, the effect of *Si* interlayers were investigated, which were found to increase the adhesion of diamond films to the substrate [74].

## 1.2. Doping the DLC

Doping the DLC films with metal or other targets had been studied for long. The effects of Titanium [75], Tungsten [76] and Tungsten Carbide ($WC$) [77] are stated in the literature clearly. There are also studies on the effect of Niobium dopants [78], but the combined effect of *Ti* and *Nb* was never studied in the literature before.

The results of the doped structures differ to a great extent. In a study conducted by Freyman et al. in 2006, effect of sulfur dopants was investigated. Sulfur doped carbon films exhibited reduced sensitivity towards humidity, which is a promising property to be exploited in DLC application in environments, where the respective type of films are weak at [79].

Wang et al. in 2005 investigated *Cr*-containing DLC films for biomedical applications and found them to exhibit low friction coefficients in simulated body fluid (0.06), along with excellent pitting and corrosion resistance [69]. Xiang et al. also reported 26.66 GPa of hardness and critical load ($L_c$) of 55 N [80] for *Cr-DLC* films. In other studies, the effects of tantalum and nickel in amorphus carbon matrix [81], titanium in amorphus carbon nanocomposite structure [82, 83], and also *Nb-DLC*, *WC-DLC* and *W-DLC* structures were investigated [83].

Although a lot of the research is conducted on Me-DLC coatings, a small portion of these studies employ different target materials. Thus, the aim of the study conducted by K. Bewilouga et. al. in 2000 was to report on Me-DLC coatings prepared by the use of different target materials: *Ti*, *Nb*, *W* and *WC*. Typical oxygen contents of high quality Me-DLC were in the range between 1 and 2 at. per cent, but the coatings Bewilouga et al. deposited contained considerably higher oxygen contents (>5 at. per cent). This is explained by noting that the amorphous carbon network surrounding the metal carbide particles is not so strongly cross linked and can react much more readily with oxygen after venting. Compared to *W-DLC* films with the lowest abrasive wear rates, *Ti*- and *Nb*- DLC films possessed intermediate wear rates. *Nb-DLC* coating in spite of having an intermediate wear rate, offered the lowest friction coefficient and a high performance under adhesive wear loading. Also it was noted that *Nb-DLC* films required no interlayer to achieve very good adhesion [83].

The reason of doping DLC with these elements is closely related to the capabilities of them when used as alloying agents. Alloying traces of *Nb* strengthens tool steels by precipitation strengthening and phase transformation control, also toughens them simultaneously by grain refinement [73]. It is known that the transition metals of group IV to VI are forming hard carbide phases [83], which is a beneficial effect in increasing wear resistance against abrasion. These features were all used for alloying in many applications (such as alloy 718 of Eiselstein), where high hardness, wear resistance, oxidation resistance and stress rupture capability is required. It was the goal of this study to combine these effects in hard and low friction DLC coatings to reach better wear resistance values, as well as to study the further interactions *Ti* and *Nb* carbides, nitrides and possibly carbonitrides.

# 2. SUBSTRATE MATERIAL AND PREPARATION PROCESS

There are 3 different substrate types used in this study; regular glass microscope slides, silicon wafers and M2 high speed tool steels. Glass and silicon wafer substrates were employed for structural characterization methods, whereas M2 is used for tribological characterization and hardness measurements. A coating that does not adhere in use, is by definition "non-functional" [84]. Due to this fact, the interaction with M2 substrate poses the most critical subject in this study and this will be studied in more detail.

M2 steel is denoted as "1.3554" or "1.3343" in DIN norm, "M2 reg.C" in AISI standards and "BM2" in British Standards. Table 2.1 shows the chemical composition of this material.

M2 high speed tool steel is well known with its high red hardness, high wear resistance, toughness and compressive strength (further physical properties of this material is added in Table 2.2). Red Hardness (Hot Strength, i.e. hardness at elevated temperatures) is achieved by the strength of two mechanisms: the matrix must be strong enough at operating temperature to prevent plucking of undissolved carbides from the contact surface and to resist plastic blunting [85, 86]. Below, some of the significant advantages of M2 HSS material are briefly summarized:

Table 2.1. Chemical composition of M2 [14]

| Chemical Analysis % | | | | | | |
|---|---|---|---|---|---|---|
| C | Si | Mn | Cr | Mo | V | W |
| 0.90 | 0.25 | 0.30 | 4.10 | 5.00 | 1.80 | 6.40 |

Table 2.2. Physical properties of M2 at 20°C [14]

| | |
|---|---|
| Density: | 8.10 kg/$dm^3$ |
| Thermal conductivity: | 19 W/(m.K) |
| Specific heat: | 460J/(kg.K) |
| Electrical resistivity: | 0.54 Ohm.$mm^2$/m |
| Modulus of elasticity: | 217×$10^3$ N/$mm^2$ |

- Super sharp cutting edges could be formed; thus easier machining of titanium alloys and less work hardening of austenitic stainless steels & nickel alloys, better quality and tight tolerances of machined parts, lower cutting forces, longer tool life, lower edge temperatures, less power consumption, less tool breakage and a more reliable tool life.
- Highest bend strength of all cutting tool materials; thus a better resistance to edge chipping, an extended cutting depth an increased feed per tooth
- 100 per cent recyclable without any loss in properties
- When coated with low wear-low friction coatings, tribological properties are amazingly enhanced [87]

Main application of this material is seen in taps, twist drills, reamers, broaching tools, metal saws, milling tools of all types, woodworking tools and cool work tools, as well as gear cutting, tapping, milling and drilling applications [14].

Prior to coating, specimens were prepared to reach the minimum surface roughness values that could have been attained in currently used lab facilities of Boğaziçi University and Atatürk University. Surface roughness both has an effect on the surface adhesion properties and on wear properties. This subject is further commented in section 4.1.1. To attain a smooth surface, a series of grinding, polishing, ultrasonic cleaning, microetching and sputter cleaning processes were carried out.

## 2.1. Grinding

M2 type high speed steel substrates that were going to be employed in this research, were coated with $TiB_2$ as a result of the former experiments. Thus, prior to PVD coating of Me-DLC layers, this existing $TiB_2$ coating had to be removed mechanically. To achieve this, a sequential water cooled grinding process was carried out in accordance with the procedure explained in detail by George F. Van der Voort in ASM Handbook volume 9 as [88]:

> "Water cooled silicon carbide paper is preferred. The usual grit sequence is 120, 240, 320, 400 and 600 grit. Finer grit sizes could be used for highly alloyed tool steels in which carbide pullout is a problem. Grinding pressure should be moderate to heavy and grinding times of 1 to 2 min are typical to remove scratches and deformation from the previous steps."

In this research, particular conditions caused the researchers to employ a more detailed grinding process that was composed of 10 steps. Main cause of these problems was due to the pre-existing $TiB_2$ layers, which were extremely hard and resistant to wear. Thus, grinding process had to start with 80 mesh papers and continue until all the existing $TiB_2$ layers are removed. Complete grinding sequence was executed using 80, 100, 120, 150, 220, 400, 600, 800, 1000 and 1200 mesh SiC emery papers of brand, "*English Abrasives*".

Grinding machine was a Metaserv 2000 Grinder / Polisher. Process was carried out using the machine for especially lower mesh grinding processes (i.e. using coarser emery papers), with a constant flow of water. However, as the emery papers got finer, especially for 1000 and 1200 mesh papers, it was required to switch from machine operated processes to manual processes to avoid the curved marks constantly being left on the substrates as a residue of the machine grinding. Since leaving no residual marks is aimed but unfortunately could not be achieved, under these circumstances, linear grinding marks were favored on the substrate surface rather than the curved marks. Curved structures were seen to be more harmful while performing tribologic characterization tests. Preferred direction for these marks was also set beforehand as parallel to the ordinate axis of the specimens with respect to their alignment in the

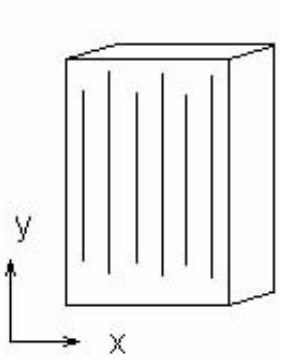


Figure 2.1. Preferred direction for the residual grinding marks

coating chamber (see Figure 2.1), to prevent further confusions while carrying out wear and adhesion tests.

## 2.2. Polishing

After the major grinding process was completed, specimens were polished to reach better surface roughness values that is required for enhanced adhesion of the coatings to the substrate. Machine used in this process was a Struers DAP-5 model device. Polishing was carried out using three successive steps; on which 0.5$\mu$m, 0.1$\mu$m and 0.05 $\mu$m sized $\alpha$-Alumina powders ($Al_2O_3$) were employed. This powder was applied in a slurry form, using tap water as the matrix. General polishing procedure was explained and summarized by George F. Vander Voort in ASM Handbook volume 9 as [88]:

> "A lubricant or extender, compatible with the diamond abrasive should be added to moisten the cloth and minimize drag. Wheel speeds of 150 to 300 rpm and moderate pressures should be used. Polishing times of 1 to 2 min are usually are adequate."

By trial and error, it was found that a polishing time of 150 to 180 seconds yielded the best results. With once in every 30 seconds in an alternating order, water and alumina slurry was poured to the polishing environment. The wheel speed was held in the range specified by Van der Voort as mentioned above. Dosage of the slurry was approximately 2-3 drops per polishing turn and 50-100 ml of water was poured

for each wetting and cleansing turn. If the water poured is lower than this amount, embedded alumina particles are observed under the optical microscope, which points to a lubricant deficiency. These particles led to surface irregularities after the coating deposition, which in turn became potential threats for scratch tests.

## 2.3. Ultrasonic Cleaning

After the grinding and polishing procedures were completed, specimens were washed under running water and then dried with paper towels. To provide an intense cleaning that removes fingerprints and attached alumina particles, an ultrasonic cleaning procedure was carried out. Ultrasonic cleaning instrument was a BUEHLER brand Ultramet 2005 model device. First ten minutes of the ultrasonic bath was done in ethyl alcohol, and the remaining ten minutes was carried out in trichloroethylene.

## 2.4. Microetching

After the specimens were ground, polished and then ultrasonically cleaned, a further microetching process was carried out, both to maximize the cleansing process and to provide a better surface roughness measure.

When the specimens were investigated, it was noted that on the surface of the pieces, there existed valleys and hills caused by the 1200 mesh emery grinding process. Although re-polishing was done, some of these irregularities were persistent. By microetching, it was aimed to diminish these valleys and hills; in the ideal case, removing them completely. Also surface asperities would now be homogenized by the chemical removal of a material layer from the surface.

The etchant was selected again by referring to the article of George F. Vander Voort in ASM Handbook [88]. Since it was written as, “Nital is generally used for tool steels regardless of the anticipated microstructural constituents”, the etchant was selected to be nital. However, when etching times and the concentration was considered, there wasn’t a rule stated clearly to be used.

> "Etching times are difficult to generalize, because of the wide range of tool steel compositions and because heat treatment can markedly alter etch response. Trial and error will determine the degree of surface dulling necessary to obtain the correct degree of etching"[88]

Initially the etchant was prepared as 5% nital and 30 seconds etching time was used. The results of this etching was insufficient, so the concentration was increased to 15% nital. Composition of the etchant was 12.5 ml of nitric acid ($HNO_3$) in 67.5 ml of ethyl alcohol. Etching time was again set as 20 seconds and after this time is elapsed, the substrates were deeply washed, first with ethyl alcohol and then with plenty of cold running tap water. After microetching, samples were dried using a high power blow dryer. They were then mounted on the rotating sample holder and were placed into the sputtering chamber to proceed with the sputter cleaning process.

## 2.5. Sputter Cleaning

Sputter cleaning is the ultimate cleaning method to remove the residues and oxide layers on the surface of the substrates in the atomic scale. Sputter cleaning by itself is not used as a cleaning method, but is used as a more sophisticated surface preparation method before the coating procedure is held. The effect of sputter cleaning is explained in a work (Okolo et al., 2004) as effective in the removal of carbon impurity atoms and adsorbed oxygen impurity atoms [89].

Arc discharges can lead to the ejection of droplets of material from the target which cause defects in the growing film. The damaged area on the target becomes a source of further arc discharges, which cause an increasing frequency of arcing, and prevent stable operation [90]. By the removal of the trace amounts of hydrocarbons that could be present on the samples, the microarcs occurring in the system could be eliminated.

In the first set of coatings, sputter cleaning was carried on for 40 minutes under Argon plasma, with very low values of current applied to the targets. Reason of this current application is to prevent the "poisoning" effect, which happens when the

sputtered impurities and contaminants, torn from the samples, get stuck on the target materials. Results of this effect is experienced as a strong reduction of the sputter rate and unstable process parameters [91]. Due to the prior conducted microetching, sputter cleaning process was carried out for 30 minutes in the second run.

# 3. FILM GROWTH METHOD

To deposit thin films, there are lots of methods, whose resulting coatings differ significantly due to varying process specific parameters and conditions. The basic sputtering process, in which materials are evaporated from the solid state by bombarding their surfaces with energetic ions, has been known and used for many years [92]. With the advance in technological methods, different deposition methods came forward. Commonly implemented deposition methods of DLC films could be summarized as, ion-beam deposition, electron cyclotron resonance microwave plasma chemical vapor deposition (ECRMPCVD), direct current (DC), radio frequency (RF) magnetron sputtering, plasma-enhanced chemical vapor deposition (PECVD) and cathodic arc deposition [6-11].

Although CVD was the most widely implemented DLC film manufacturing method until 1990's, nowadays this method is outran by physical vapor deposition (PVD) methods, providing much lower deposition temperatures. Temperatures around 1000°C is required for CVD processes, whereas films with better microstructures are attained with PVD, with around 500°C.

For the coating purposes of this study however, the "Closed Field Unbalanced Magnetron Sputtering" device of Teer Coatings Company (UK Patent No 2 258 343, USA Patent No 5 556 519, European Patent No 0 521 045) was used. Development of the CFUBMSIP intended to increase the ion current density in magnetron sputter ion plating. The major stage in the development of the system was the idea of using unbalanced magnetrons in an arrangement whereby neighboring magnetrons are of opposite magnetic polarity. Using this arrangement, the deposition zone in which the substrates are located is surrounded by linking magnetic field lines. This traps the plasma region, prevents losses of ionizing electrons and results in significant plasma enhancement [93]

The deposition can be carried out using high density plasma of low energy bombarding ions. This results in deposition of very dense, non columnar coating structures with low internal stresses. The use of a low bias voltage during deposition also allows deposition of coatings with dense structures at low temperatures. Also as the current to the magnetrons is increased there is a corresponding increase in ion bombardment; hence the ratio of ions to neutrals within the system is kept approximately constant. This ensures that the quality of the coatings produced by the system is independent of the deposition rate [93].

Use of the CFUBMS system also allows coatings with graded properties to be produced. Thus, both the coating / substrate interface and the coating surface properties can be optimized, so that a very high performance coating can be produced with excellent coating-to-substrate adhesion [90]. Further information about the process is available in the study of Arnell and Kelly, in 1999 [90], and also in the technical description of the patents, cited above. Also information about the target materials and the quality of the sputtering process is supplied in detail by Waibel and Friz, 2006 [94].

Although CFUBMS provides a significant increase in the high density plasma captured, still there exist problems due to the decreased coating rate and microarcs. Arc discharges can lead to the ejection of droplets of material from the target which cause defects in the growing film, as mentioned in the previous chapter. The damaged area on the target becomes a source of further arc discharges, which causes an increasing frequency of arcing, preventing stable operation [90]. It is possible to avoid these issues by pulsing the substrates.

In a continuous DC-driven discharge, the cathode potential is always kept negative, whereas in a pulsed DC-driven discharge the potential on the target is periodically modulated, at a pulsing frequency typically between 20 and 350 kHz. For a certain reverse time, a part of each pulse, a positive reverse voltage, is applied; this phase is subsequently called the reverse phase and typically accounts for 10-50% of each pulse. The remaining 90-50% is then called the duty phase, or simply duty [95].

It was shown that pulsing the magnetron discharge at medium frequencies (10-200 kHz), when depositing highly insulating materials, can stabilize the discharge, almost eliminating arcing and the formation of defects in the film [96]. Furthermore, deposition rates during pulsed reactive sputtering approach those obtained for the non-reactive sputtering of pure metal films [97].

## 3.1. Coating Process

There were two runs of coatings, in which the same structure was grown, but under different coating parameters, since a thicker coating was required in the second set. First coating procedure, which was conducted on 4/10/2006 was denoted as 41006 and second, on 17/1/2007, was denoted as 1717. Through both runs of Me(Ti,Nb)-DLC coating process, target configuration was held same, consisting of one niobium target and three titanium targets. The configuration of the system could be represented as seen in Figure 3.1.

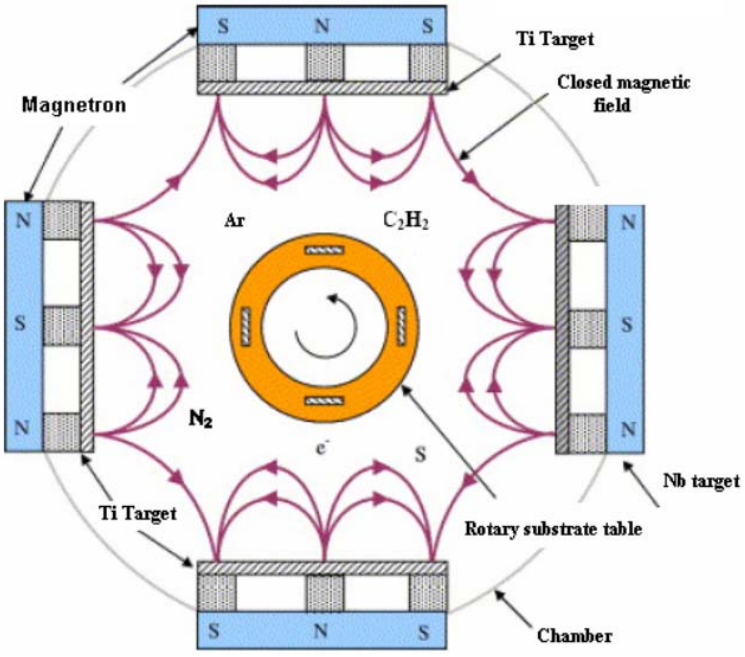


(a) Schematic representation of CFUBMS coating system

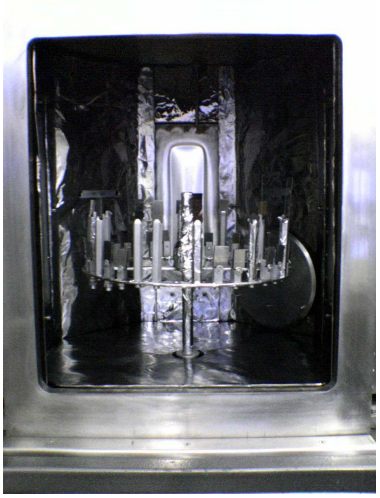

(b) Actual image

Figure 3.1. CFUBMS coating system

Table 3.1. General information about coating process

| | |
|---|---|
| Substrate material voltage (-V) | 75 |
| Working Pressure (Pa) | 0,35 ($2,5 \times 10^{-3}$ Torr) |
| Target Currents (A) | Ti:6, Nb:1,5 |
| Frequency (kHz) | 175 |
| Duty time ($\mu$s) | 2,5 |

The general information pertaining to the coating process is supplied in Table 3.1. Start pressure was set to be $2 \times 10^{-5}$ Torr in the first run and $1.9 \times 10^{-5}$ Torr in the second run. The gases used in the chamber in the various stages of the process was Argon (being Gas 1), $N_2$ (being Gas 2 and Gas 3) and $C_2H_3$ (being Gas 4) and they were same again for both processes. The parameters of the process are given in the table 3.2 in detail. Second coating procedure lasted slightly longer than the first one, which is consistent with the fact that the second set of coatings (with 2.5 $\mu$m of thickness) were apparently thicker than the first set coatings (1,5 $\mu$m of thickness).

In order for the coating thickness and chemical composition (stoichiometry) to be uniform, the substrate materials are put in rotational motion, in the chamber, in the course of deposition. The axis of this rotation is the centerline of the chamber and the rotational speed is set to be around 4 revolutions per minute. This revolution motion also has a critical role on the prevention of brittle film formation and early delaminations [98].

After the sputter cleaning process is completed, deposition of the titanium interlayer to enhance the adhesion of the coating to the substrate is initiated. In the first run, a Ti interlayer was coated on the substrates for 2 minutes and in the second run, this process took 10 minutes. Thus, a thicker adhesion promoting layer was coated in the second run. Figure 3.2 shows a snapshot from the interlayer coating process.

Table 3.2. Coating process parameters in detail

| **Date**: 4/10/2006 | | | | | | | | | | | | | | | | | | **Run number**: 41006 | | | | | |
|---|---|---|---|---|---|---|---|---|---|---|---|---|---|---|---|---|---|---|---|---|---|---|---|
| **Targets/Strength/Polarity** | | | **A** | | | **B** | | | **C** | | | **D** | | | **dc-bias** | | | **Pulsed-dc** | | | | | |
| | | | **Ti** | | | **Nb** | | | **Ti** | | | **Ti** | | | | | | **Set Values** | | | **Read Values** | | |
| **Time** | **Cycle stage** | **pressure** | **volt** | **kw** | **Amp** | **volt** | **kw** | **Amp** | **volt** | **kw** | **Amp** | **volt** | **kw** | **Amp** | **volt** | **kw** | **Amp** | **T:µs** | **F:kHz** | **Volts** | **Volts** | **Amp** | **W** |
| **09:25** | Ion cleaning | 2,0 | 248 | 0,030 | 0,15 | 279 | 0,028 | 0,10 | 250 | 0,038 | 0,15 | 268 | 0,038 | 0,15 | 1000 | 0,18 | 0,16 | | | | | | |
| **10:05** | Ti coating | 2,5 | | | 6,00 | | | 0,15 | | | 6,00 | | | 6,00 | | | | 2,5 | 175 | 75 | | | |
| **10:07** | TiN | 2,5 | 347 | 2,080 | 6,00 | 88 | 0,020 | 0,17 | 356 | 2,110 | 6,00 | 435 | 2,600 | 6,00 | | | | 2,5 | 175 | 75 | 75 | 2,02 | 156 |
| **10:17** | TiC+Nb | | | | | | | | | | | | | | | | | | | | | | |
| **10:27** | TiCN+Nb | | | | 6,00 | | | 1,00 | | | 6,00 | | | 6,00 | | | | | | | | | |
| **10:40** | DLC | 2,0 | 365 | 2,200 | 6,00 | 397 | 0,600 | 1,50 | 366 | 2,200 | 6,00 | 426 | 2,560 | 6,00 | | | | | | 75 | 75 | 1,56 | 116 |
| **11:05** | DLC | 2,0 | 404 | 2,400 | | 447 | 0,670 | | 413 | 2,470 | | 480 | 2,890 | | | | | | | | | | |
| **11:25** | OFF | | | | | | | | | | | | | | | | | | | | | | |

| **Date**: 17/01/2007 | | | | | | | | | | | | | | | | | | **Run number**: 1717 | | | | | |
|---|---|---|---|---|---|---|---|---|---|---|---|---|---|---|---|---|---|---|---|---|---|---|---|
| **Targets/Strength/Polarity** | | | **A** | | | **B** | | | **C** | | | **D** | | | **dc-bias** | | | **Pulsed-dc** | | | | | |
| | | | **Ti** | | | **Nb** | | | **Ti** | | | **Ti** | | | | | | **Set Values** | | | **Read Values** | | |
| **Time** | **Cycle stage** | **pressure** | **volt** | **kw** | **Amp** | **volt** | **kw** | **Amp** | **volt** | **kw** | **Amp** | **volt** | **kw** | **Amp** | **volt** | **kw** | **Amp** | **T: µs** | **F: kHz** | **Volts** | **Volts** | **Amp** | **W** |
| **14:10** | Ion cleaning | 2,0 | 258 | 0,052 | 0,20 | 278 | 0,055 | 0,20 | 261 | 0,052 | 0,20 | 283 | 0,057 | 0,20 | 1000 | 0,16 | 0,18 | | | | | | |
| **14:40** | Ti coating | 2,5 | | | 6,00 | | | 0,20 | | | 6,00 | | | 6,00 | | | | 2,5 | 175 | 75 | | | |
| **14:50** | TiN | 2,5 | 346 | 2,070 | 6,00 | | | 0,20 | 345 | 2,058 | 6,00 | 420 | 2,520 | 6,00 | | | | | | | 75 | 2,70 | 206 |
| **15:00** | TiC-Nb | | | | 6,00 | | | 0,20 | | | 6,00 | | | 6,00 | | | | | | | | | |
| **15:00** | TiC-Nb-N | | | | 6,00 | | | 1,50 | | | 6,00 | | | 6,00 | | | | | | | | | |
| **15:35** | DLC | 2,0 | 412 | 2,470 | 6,00 | 447 | 0,680 | 1,50 | 420 | 2,500 | 6,00 | 496 | 2,970 | 6,00 | | | | | | | 75 | 2,30 | 165 |
| **16:40** | OFF | | | | | | | | | | | | | | | | | | | | | | |

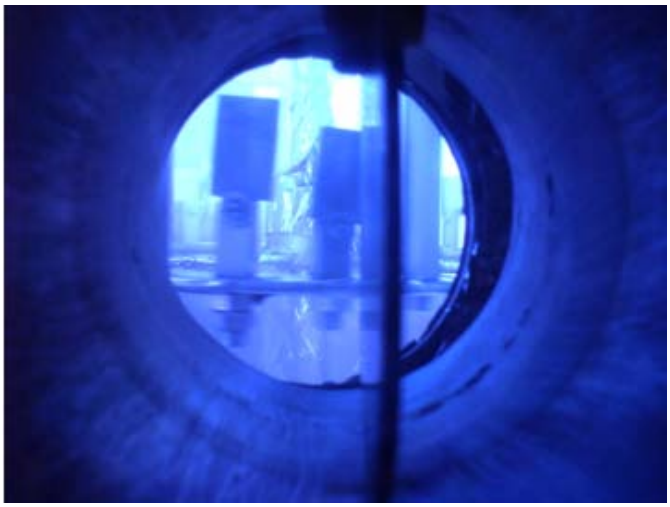

Figure 3.2. Deposition of the Ti interlayer, M2 substrates seen in rotation

Following the deposition of the interlayer, nitrogen gas is admitted to the chamber in a controlled manner and the growth of $TiN$ phase is initiated. Growth of this phase takes around 10 minutes and while the deposition is being carried out, the pressure is set around 2.5 mTorr level. A slight coloration towards pale blue is observed (see Figure 3.3). After the growth of $TiN$ layer, a slow and controlled intake of $C_2H_2$ into the coating chamber is initiated.

Figure 3.3. TiN growth phase, to the back, glass substrate seen in rotation

Entry of $C_2H_2$ is provided such that the weight percent of the gas is gradually increased from 20 wt.% to 55 wt.% over 20 minutes. With $C_2H_2$ intake, it is desired

to grow $TiC$ with the help of the carbon in $C_2H_2$, where the grown $TiC$ will be doped with $Nb$. To provide this doping process, current applied to $Nb$ target is also gradually increased. By this was, $Nb$ targets are forced to be sputtered and then accumulated on the substrate material. It must also be noted that there is significant amount of Nitrogen present in the chamber, which causes a wide variety of phases available, ($TiN$, $NbN$, $TiCN$, $NbCN$, etc.) which will be discussed thoroughly in the XRD analysis part.

When the plasma is investigated, it is noted that the increasing amount of $C_2H_2$ turned the plasma color from pale blue to pale pink (see Figure 3.4) and eventually when 55 wt.% of $C_2H_2$ is attained, the chamber is completely turned into pink (see Figure 3.5).

After all the carbide layers are coated and 55 wt.% of $C_2H_2$ is attained, the parameters are adjusted to yield a DLC coating. In both of the processes, pressure level of the chamber is set to be 2 mTorr. Average coating time of DLC layers were around 45-65 minutes.

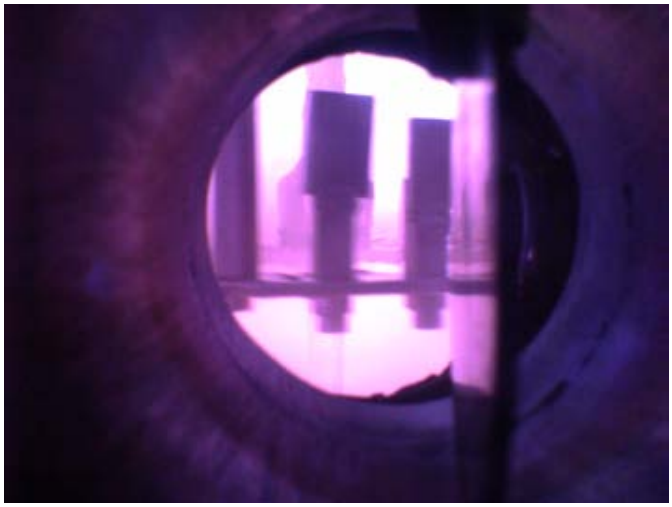

Figure 3.4. Snapshot from TiC(N)-Nb coating process

The quality and the features of the coatings deposited with PVD methods are highly process and environment dependent. One of most important parameters among others is the coating deposition temperature, which determines the film growth pat-

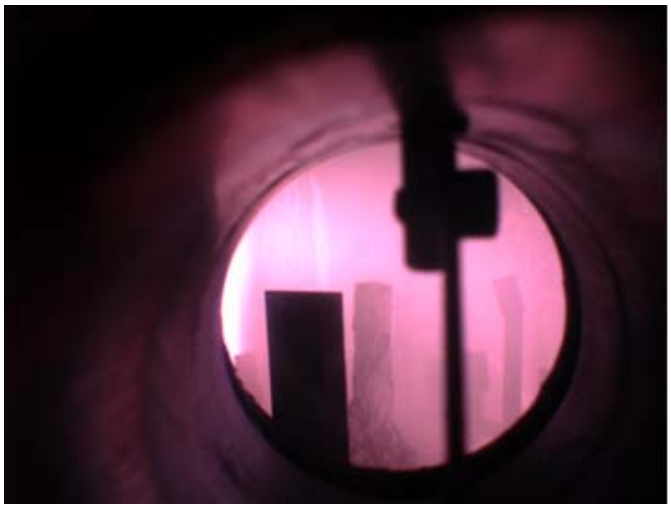

Figure 3.5. Snapshot from DLC coating procedure

tern. After examining thick coatings of $Ni$, $Ti$, $W$, $Al_20_3$, and $ZrO_2$, Movchan and Demchishin in 1969 divided the $T/T_M$, scale into three zones [99], where $T$ is the temperature of the coating process and $T_M$ is the melting temperature of the coating:

- Zone I ($T/T_M < 0.25$-$0.3$), consisting of tapered crystallites with domed tops, which increase in width with temperature. These crystallites were also separated by voids [100]
- Zone II ($0.25$-$0.3 < T/T_M < 0.45$), consisting of columnar grains with smooth material surface
- Zone III ($T/T_M > 0.45$), consisting of equiaxed grains and a bright surface.

Later, Thornton added a third axis for sputtering pressure [4] and another zone to the zone model for sputter deposited films. This is a transition zone between regions 1 and 2. This zone is very similar in appearance to Zone 1 but because of the elevated temperature, the surface diffusion rate of the adatoms is sufficient to make the microstructure smoother and more dense than Zone 1 [28].

When the coating temperatures employed in this study are considered, it is expected that the coating structure will have Zone I character (see Figure 3.6). Thermocouple readings were around 300°C on the substrates in the course of coating process. This temperature being low is actually the advantage of PVD coatings over CVD pro-

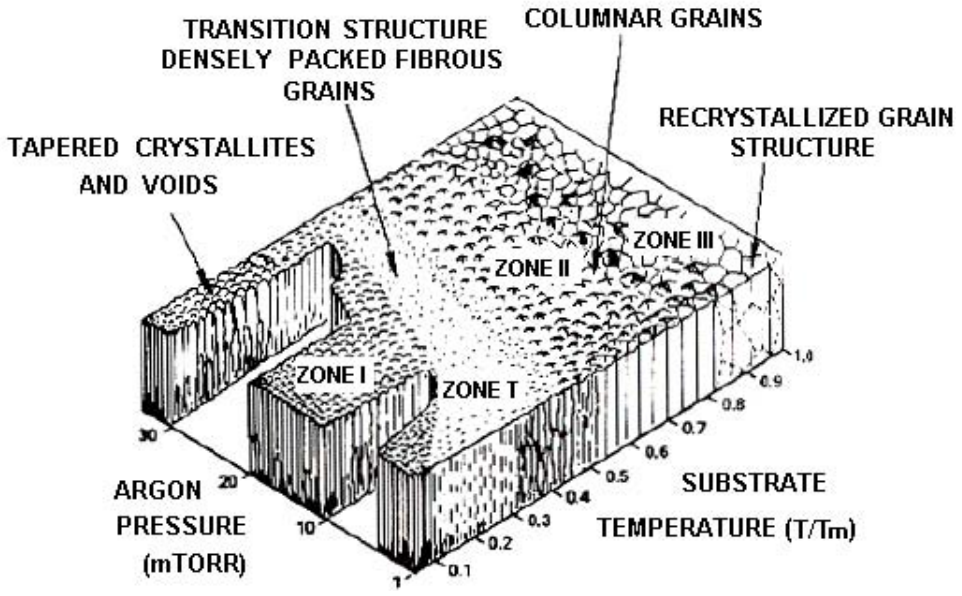


Figure 3.6. Thornton Structure Zone Model [4]

cedures, on the contrary causing a slightly more columnar structure with voids. The open, columnar structure is a result of low adatom surface diffusion which is unable to compensate for the shadowing of the intercrystalline valleys by the crystalline peaks. The crystalline columns are often polycrystalline in nature with individual grains being small and equiaxed [28].

To summarize, the steps of the coating process which have been detailed above, were completed in 2 hours for the first run and 2.5 hours for the second run. The coatings were then employed in the characterization studies, which will be detailed in the succeeding chapters.

# 4. EXPERIMENTAL WORK

After the deposition of the coatings was completed, characterization and testing procedures were initiated. Characterization of the coatings were conducted to determine the process-dependent properties in four different aspects. These were mainly about structural characterization, compositional characterization, tribological characterization and hardness measurements.

## 4.1. Structural Characterization

First aspect, being the structural characterization, was carried out by employing roughness examinations using surface profilometers and atomic force microscopy (AFM). Characterization is then continued with scanning electron microscopy (SEM). Aim of these studies is to get a measure of roughness and also determine important growth features of the coatings.

### 4.1.1. Surface Roughness

Surface as a term, could be defined as a boundary between a workplace and its environment [101]. In this study, it should be noted that there are two surfaces of importance. First one is the apparent top cover, serving as the "functional surface", that is defined as the surface required to perform the function related to the users perception of the equipments quality [15]. Second important surface however, is the surface located at the interface which plays a crucial role in the adhesion characteristics of coating-substrate couples.

Results of many researches, conducted to investigate the dependency of coating properties on surface roughness values suggest that, films prepared on the smoother surfaces exhibit better adhesion (higher critical load) and relatively higher hardness values [102, 103, 104, 105].

Surface roughness also affects microstructure due to the depositing films replication of the underlying topography; smooth surfaces will lead to a more uniform and fine grain structure, while rough surfaces lead to a more columnar microstructure with peaks, valleys and other defects act as preferred growth sites [28]. Another effect of roughness is noted on the dispersion of results in instrumented indentation testing. Smooth and well-polished surfaces are preferred for reproducible and reliable results [106].

In spite of these facts, an interface roughened on a scale of feature size somewhere between monolayers and the thickness of the deposited film may enhance adhesion performance in several ways [107]:

- A roughened surface will actually have geometrically enhanced contact area over work of adhesion will be effective. The perceived work of adhesion will be increased approximately in the proportion to that area.
- If the interface is extensively and deeply convoluted, the film may adhere by simple mechanical interlocking after the style of Velcro®.
- Asperities or roughness of the interface can cause pinning of an interface fracture and thereby inhibit propagation of that fracture [107].

For the measurement of the roughness values both before and after the coating process, a Mitutoyo Surftest SJ-301 model Surface Profilometer is employed. Atomic Force Microscopy (Quesant Q-scope 350) was also used for one sample on glass substrate. This AFM device belongs to Boğaziçi University R&D Lab facility and was bought with a DPT grant. At the time of the research, the device was not fully utilized, since the technical person in charge hasn't been given a training about the device. Still his help about determining many features of the coating surfaces is appreciated.

### 4.1.2. SEM Studies

For the theory of scanning electron microscopy, a brief introduction is supplied from the technical report of Allen Sampson from Advanced Research Systems [108].

Initially, a beam of electrons is generated by the scanning electron microscope in vacuum. That beam then is collimated by electromagnetic condenser lenses, focussed by an objective lens, and scanned across the surface of the sample by electromagnetic deflection coils. The primary imaging method following the scanning process is by collecting secondary electrons that are released by the sample. Secondary electrons are detected by a scintillation material that produces flashes of light from the electrons. The light flashes are then detected and amplified by a photomultiplier tube. By correlating the sample scan position with the resulting signal, an image can be formed, which is strikingly similar to what would be seen through an optical microscope. The illumination and shadowing show a quite natural looking surface topography [108].

Scanning electron microscopy is a useful instrument for investigating coating properties, such as the growth structure, coating defects, surface characteristics, coating thickness determination, etc. Scanning Electron Microscopy investigations of the coatings were carried out in Erzurum, with a Jeol 6400 model SEM device.

## 4.2. Compositional Characterization

Compositional characterization of the coatings were carried out by X-Ray Diffraction (XRD) and X-Ray Photoelectron Spectroscopy (XPS) tests. It was aimed to determine the constituents of the coatings, as well as binding structures and crystallinity.

### 4.2.1. XRD Studies

Diffraction occurs when a wave encounters a series of regularly spaced obstacles that are capable of scattering the wave and that have spacings comparable in magnitude to the incident beam's wavelength. Furthermore, diffraction is a consequence of specific phase relationships that are established between two or more waves that have been scattered by the obstacles. A sample to be diffracted could be expressed as two parallel planes of atoms, which have the same $h$, $k$ and $l$ Miller indices and are separated by the interplanar spacing $d_{hkl}$. [43]

Assuming a parallel, monochromatic and coherent beam of x-rays with wavelength $\lambda$ is incident on these two planes at an angle $\theta$, there exists a simple expression relating the x-ray wavelength and interatomic spacing to the angle of the diffracted beam, known as Bragg's Law. Here n stands for an integer [43]

$$n\lambda = 2d_{hkl}\sin\theta \tag{4.1}$$

For a monocrystalline sample, this relation is fulfilled for a number of discrete directions in space, so that a pattern of spots can be observed, which is formed by the reflections at planes with different orientations. In a polycrstalline sample, the orientations of the crystallites form a continuous distribution and diffraction rings, instead of spots, are observed. X-Ray diffractometry is used for crystal structure and interplanar spacing determinations, probing distributions of crystalline phases in a thin layer (thickness 20-200nm)[109]

Studies in this research were carried out with Rigaku-2200 D/Max model X-Ray diffractometer. The type of X-Ray, scanning the substrate and the coating was a Cu-$K_\alpha$ source with $\lambda = 1.5405°$ wavelength, powered up to 30 kV and 30 mA. The goniometer in this setting was a RINT 2000 wide angle model head, equipped with a standard sample holder, where a filter was not used.

The system had an automatic monochromator with a divergence and scattering slit of 1/2 degrees. Receiving slit was set to be 0.15 nm. Scanning mode was continuous with a scan speed of 1 degree/minute. Each scan step was set to be 0.05 degrees. Scan range was set to be spanned from 15 to 100 degrees. Theta offset and sample rotation values were both 0 degrees. System settings were kept constant for analyzing both the substrate material and the Me-DLC coating lying atop.

When thin film coatings are analyzed in XRD, it is possible to observe both signals transmitted from the coating and also signals coming from the substrate lying below. Due to this fact, before diffracting the coating, a proper XRD survey for the substrate material was done to determine the peaks that belong to the substrate and

eliminate these while assessing the spectra.

Common second phases observed in wrought heat resistant steel alloys are metal carbides $MC$, $M_{23}C_6$, $M_6C$ and $M_7C_3$, where $M$ represents one or more metallic elements. The effects of carbide formation could be interpreted by different approaches. First of all, grain boundary carbides, when properly formed, strengthen the grain boundary, prevent or retard grain boundary sliding and permit stress relaxation. Another benefit is seen when fine carbides are precipitated in the matrix. These carbides lead to a strengthening mechanism, which is observed due to precipitation strengthening. Third, these carbides can tie up certain elements that would otherwise promote phase instability during service. Thus, they are desired elements for strengthening the structure. However, if carbides are precipitated as a continuous grain-boundary film, in this case material properties will be seriously degraded and this structure is not desired [110]. In order to interpret the XRD spectra properly, a brief explanation about the widely observed carbide phases shall now be supplied.

$MC$ type carbide is most frequently titanium carbide; other types such as niobium carbide, tantalum carbide or hafnium carbide are less common. Titanium carbide has some solubility for other elements, such as nitrogen, zirconium and molybdenum. Metal carbides are usually irregular in shape or cubic. They can be preferentially colored by certain etching processes [110].

$M_6C$ carbide is generally rich in molybdenum or tungsten, but other elements such as chromium, nickel or cobalt may substitute for it to some degree. It is the most commonly observed carbide in the cobalt base superalloys and in nickel base alloys with high molybdenum and/or tungsten contents. In wrought alloys, it may precipitate at the grain boundaries in a blocky form or intergranularly in a Widmanstätten pattern and can be preferentially stained by certain etchants. As for $M_7C_3$, additions of such elements as cobalt, molybdenum, tungsten or niobium to nickel base alloys prevents formation of $M_7C_3$ [110].

Another phase that occurs is the Laves phase, which is a tcp phase having a $MgZn_2$ hexagonal crystal structure with a composition of the $AB_2$ type. Typical examples include $Fe_2Ti$, $Fe_2Nb$ and $Fe_2Mo$, but a more general formula is $(Fe, Cr, Mn, Si)_2(Mo, Ti, Nb)$. Excessive amounts will impair room-temperature tensile ductility; creep properties are not significantly affected [110].

There are also nitride phases present in the coatings studied. Nitrides are commonly observed in superalloys containing titanium or niobium as titanium nitride (most common) or niobium nitride. Nitrides are quite hard and will appear in relief after polishing. They have some solubility for carbon and may be referred to as *Ti(C,N)*, *Nb(C,N)* and so on. The usual amounts present in superalloys generally have little influence on properties [110].

### 4.2.2. XPS Studies

X-ray photoelectron spectroscopy, also known as also electron spectroscopy for chemical analysis (ESCA), works by irradiating a sample material with monoenergetic soft x-rays causing electrons to be ejected. Operation mechanism is similar to that of Auger electron spectroscopy, (AES) [111]. Relative concentrations of elements can be determined from the photoelectron intensities [112]. The density of states, in the valence band, the valence band structure and the position of the core levels can be related to the chemical binding of the atoms ejecting the electrons. Thus, XPS is suited to measure the elemental and chemical compositions of the top 5 nm of a sample [109].

Identification of the elements in the sample can be made directly from the kinetic energies of these ejected photoelectrons. The basis of photoelectron spectroscopy is based on the equation;

$$h\nu = \frac{1}{2}m{v_c}^2 + q\Phi + E_b \tag{4.2}$$

where "$\nu$" is the frequency of the incoming quanta (later dubbed as "photons" by Lewis [113]), $h$ is the Planck's constant, $\frac{1}{2}m{v_c}^2$ is the kinetic energy of the outgoing photo-

electron of mass $m$ and velocity $v$, $q$ is the reference charge, $\Phi$ is the work function of the emitting material and $E_b$ is the so-called "binding energy", expressed against the Fermi level of the material [114].

Table 4.1. Working specifications of the PHOIBOS XPS analyzer

| | |
|---|---|
| Analysis Method: | XPS |
| Analyzer: | PHOIBOS HSA 3500 150 R5e [HWType 30:14] MCD-9 |
| Analyzer Lens: | Medium Magnification |
| Analyzer Slit: | 5:7x20-2: open |
| Scan Mode: | Fixed Analyzer Transmission |
| Dwell Time: | 0.1 |
| Excitation Energy: | 1486.61 |
| Pass Energy: | 50 |
| Bias Voltage: | 90 |
| Detector Voltage: | 3000 |
| Eff. Workfunction: | 4.31 |

As noted in the researches (Paik, 2005) [115], analysis of the obtained raw spectra begins with the removal of the background scattering present in the core spectra. This background arises from inelastic scattering of the electrons during transport to the surface and has a characteristic step-like shape. The background signal leads to a distortion of the true spectrum (which is known as the primary excitation spectrum) and has stimulated much activity on how to remove it from the spectra [115]. To avoid this background effects from interfering, Shirley background subtraction method was employed in the analysis of XPS results of both Me-DLC sets [116].

XPS measurements of this research were carried out in METU Central Lab R&D-Training Center and Gebze Institute of Technology (GYTE). These institutes provided the spectra of Me-DLC coatings on glass and M2 substrates, but further information about the binding nature or peak fitting of the results were not supplied. Thus results

are only interpreted by the author qualitatively, referring to the articles published in this subject. Device used for this analysis was a Specs brand PHOIBOS 100/150 model analyzer whose working specifications are given in Table 4.1.

## 4.3. Tribological Characterization

Thin films or coatings on solid substrates constitute a critical part of many manufactured products, including semiconductor devices, coatings to protect against wear and corrosion, optical components, magnetic recording heads and discs, etc. In such applications, qualities such as strong adhesion, low wear and stability of the interface are extremely important [107]. Monitoring of these qualities are carried out by employing pin on disc tests and scratch tests.

### 4.3.1. Pin on Disc Tests

Pin on disc tests are conducted with Teer brand POD-2 computer controlled pin on disc testing system and main scope of this procedure is to measure wear and friction properties of thin coatings. Testing is carried out using a fixed ball counterpart against a coated test piece to measure the tribological properties of a coating [117]. Standard counterparts are 5mm diameter WC-Co balls, whereas other ball materials are available too. By measuring the amount of coating that is left, the coating wear rate can be determined. A schematic representation of the system is shown in Figure 4.1

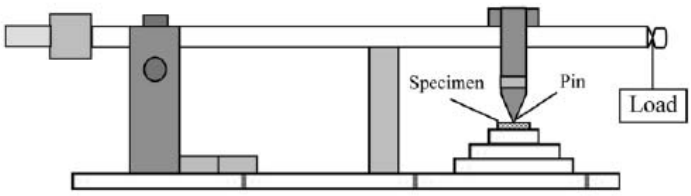


Figure 4.1. Schematic representation of the pin-on disc test configuration [5]

There are two main standards referring to the pin-on-disk tribotest; DIN 50 324 “Testing of friction and wear” and ASTM G 99 - 95a, “Standard test method for wear testing with a Pin-on-Disk apparatus”. Both ASTM standards determine the amount

of wear by measuring appropriate linear dimensions of both specimens (ball and disk) before and after the test, or by weighing both specimens before and after the test. In practice, linear measures are often preferred since mass loss is often too small to measure precisely [6]. The detailed representation of the pin-track contact is shown in Figure 4.2, where $F$ is the normal force applied, $r$, ball diameter, $R$, radius of the wear track and $w$, rotational speed of the ball.

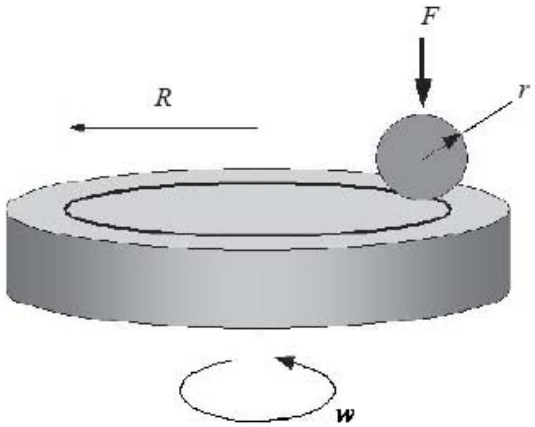


Figure 4.2. Typical ball-on-disk setup [6]

Assuming that there is no significant pin wear, the volume loss of the disk is given by [6]:

$$V_{coating} = 2\pi R[r^2 \sin^{-1}(d/2r) - (d/4)(4r^2 - d^2)^{1/2}] \tag{4.3}$$

Here $V_{coating}$ denotes the disk volume loss ($mm^3$) and $d$, width of the wear track (mm). The disk volume loss calculated in this manner may have certain error due to variations around the wear track, accumulations of debris and plastic deformation. A stylus profilometer is often used to measure the cross-sectional area of the wear track in several places around the track. This provides a more accurate measure of the disk volume lost when multiplied by the track length.

Wear rate could be calculated by measuring the volume of coating worn out, by examining the wear profile, as shown in Figure 4.3. The steps of the calculation begins

with the determination of the wear length, $L$ in mm.

$$L = (2\pi r).w.t \tag{4.4}$$

where t is the total duration of the test in seconds.

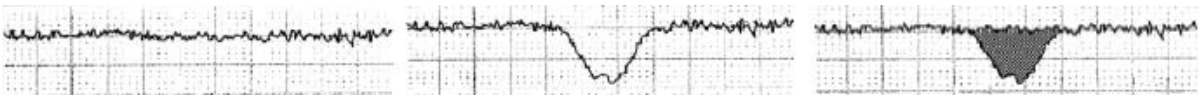

Figure 4.3. Profiles before (left) and after (middle) test with worn coating (right) [5]

Then based on the observations from the wear profile (like shown in Figure 4.3), wear volume is calculated.

$$V_{coating} = A(2\pi r) \tag{4.5}$$

where A denotes the area read from the profile.

By using the volume of the coating worn, it is possible to determine the abrasion wear rate (K) [118] with the equation:

$$K = \frac{V_{coating}}{F.L} \tag{4.6}$$

After the determination of the wear volume, wear coefficient (k) could be calculated using the Archard's equation for wear:

$$V_{coating} = k\frac{LF}{H} \tag{4.7}$$

Where (k) is the dimensionless wear coefficient and H is the hardness of the softest element in the system.

### 4.3.2. Scratch Test

Scratch tests are one of the most important elements in the tribological characterization studies. In this test, a controlled scratch is performed, with specific loads, loading rates and scratch lengths. By generating a scar, the plastic deformation resistance, adhesive properties of the films on that specific substrate and friction coefficients could be measured [7].

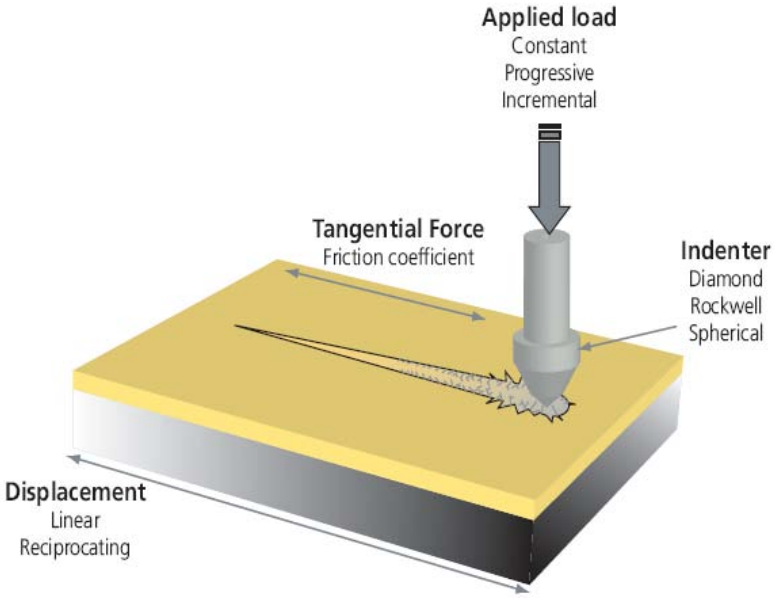


Figure 4.4. Schematic representation of adhesion scratch testing procedure [7]

The tip, either of diamond or sharp metal, is drawn across the coated surface under constant, incremental or progressive loading cycles. At a certain critical load, the coating will start to fail. The critical load value could be stated as the smallest load at which the coating is damaged, by a definition provided by Takadoum and Bennani in 1997 [103]. There are different terminologies corresponding to critical loads, as $L_{c1}$ meaning the first point of coating damage and $L_{c2}$, the point of complete coating failure. In this study, the only critical load value is the one used to describe the total coating failure.

The critical loads are very precisely detected by means of an acoustic sensor attached to the load arm and can be correlated with observations from a built-in optical

microscope. The critical load data is used to quantify the adhesive properties of different film - substrate combinations. In addition to acoustic emission, the Scratch Testers measure the applied normal force, the tangential (friction) force and the penetration depth. These parameters, together with the acoustic emission, constitute a unique signature of the coating system under test [119].

This test depends critically on the elastic properties of the film and substrate, the nature of the stylus, the thickness of the film, etc [107]. Scratch tests, pertaining to this study were conducted with RST CSM Revetester device in Atatürk University, with the specifications given in Table 4.2. Indenter is a Rockwell diamond tip, with radius 200 $\mu$m (Serial no: P-234), which is a common type used for coating thicknesses in the range of 0.130 $\mu$m [84].

Table 4.2. Scratch testing process specifications

| Test Type: | Linear Progressive |
|---|---|
| Begin Load (N): | 0.2 |
| End Load (N): | 80.2 |
| Loading Rate (N/min): | 100 |
| Speed of the tip (mm/min): | 10 |
| Scratch Length (mm): | 8 |

## 4.4. Hardness Measurements

Hardness, with its conventional physical meaning, is the mean contact pressure that results in a condition of a fully developed plastic zone [120]. This value has a crucial effect on both the friction properties and the wear rates. In the scope of current study, a high hardness value is always desired. However high hardness is usually accompanied with a high friction coefficient and increased wear in the tribological behavior [33]. Thus, while putting efforts to increase hardness, frictional behavior should be closely monitored to prevent departure from optimum coating parameters.

There exists extensive information about the hardness values reached in the indentation tests of thin coatings. Among these, the studies of (Hainsworth et al., 1998), (Kassavesitis et al., 2006), (Galvan et al., 2006), (Fischer-Cripps et al., 2006) and (Cekada et al., 2006) prevail [121, 122, 123, 120, 124]. Below added are the specific information pertaining each hardness measurement procedures.

### 4.4.1. Microhardness Measurements

Microhardness measurements were carried out in an environment of 25°C ambient temperature and 68% relative humidity in accordance with the standards, ASTM C 1327-03 and E 384-05a. Indenter tip was chosen to be a standard diamond Vickers type indenter, and the hardness values of both the substrate and the coating were measured with the same equipment and identical settings. Tests were conducted under 25, 50, 100, 200, 300, 500 and 1000 gf of loads. The hardness value of the substrate material (M2 type high speed steel) was measured as 750 HV.

It is of great importance that the indent depth, which is created as a result of the hardness measurement procedure, remains within the 1/10 of the total coating thickness to prevent substrate effects from interfering with the measured value [125]. If this is not provided, measured hardness value will be affected by the substrate effect due to the deformation behavior of the coating being affected by the substrate.

When hardness profiles of substrate-coating couples are considered, it is possible to talk about two different configurations. “Case I” occurs when a softer coating is deposited on a harder substrate, whose configuration could be schematically represented as in Figure 4.5a. It should be noted that the measured hardness of the surface increases as the indentation depth gets deeper. This is the effect of the harder substrate lying beneath the soft coating, presenting a beneficial effect. Hardness evolution for Case I is shown in Figure 4.5b.

The other configuration of substrate-coating couple is seen when coating material is harder than the substrate material, “Case II”. In this case, hardness evolution

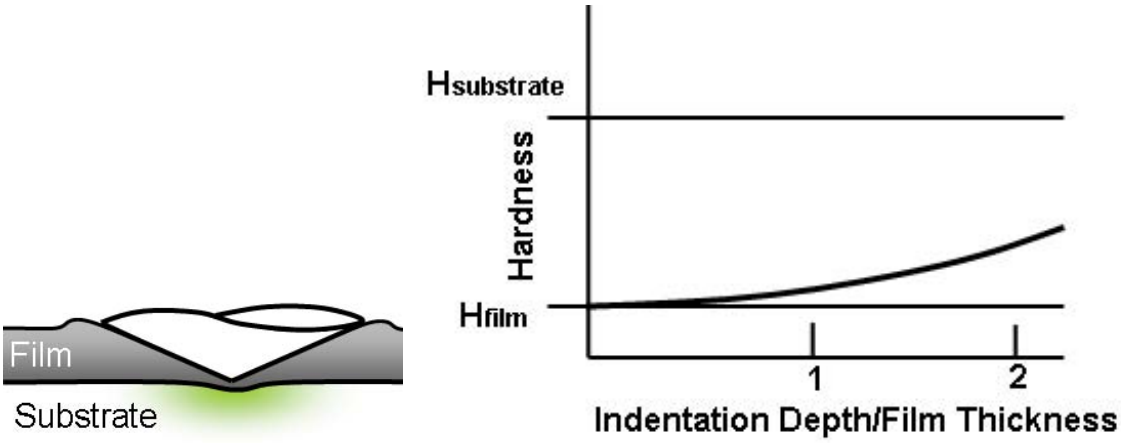


(a) Schematic representation (b) Hardness evolution

Figure 4.5. CASE I: Soft coating on a hard substrate [8]

is reversed and underlying material is expected to have a detrimental effect on the measured hardness value. This configuration could also be represented as shown in Figure 4.6a. As the load gets higher, the measured hardness value would get closer and closer to the actual substrate material hardness, which is practically reached when the entire coating thickness has been traveled by the indenter and a fresh substrate surface is reached. This hardness evolution behavior is shown in Figure 4.6b.

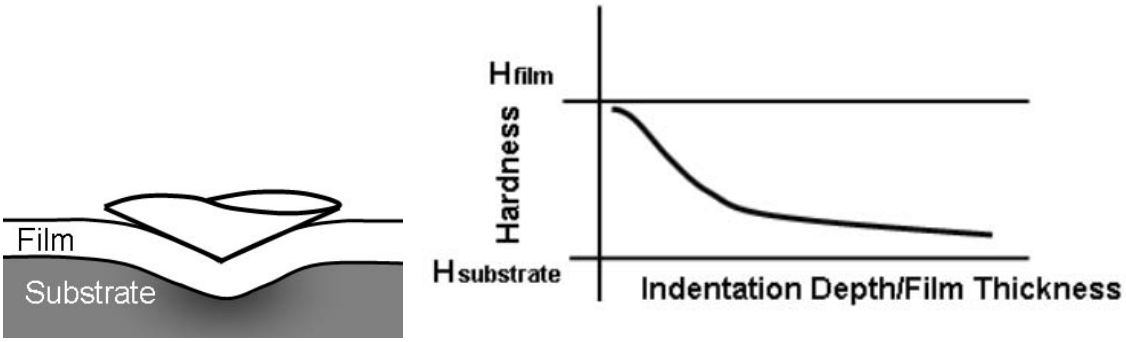


(a) Schematic representation (b) Hardness evolution

Figure 4.6. CASE II: Hard coating on a soft substrate [8]

In the course of this study, under all circumstances, coating material is expected to have a higher hardness value than the substrate material. Thus, it was expected that the evolution of hardness will demonstrate the behavior of Case II configuration.

### 4.4.2. Nanohardness Measurements

This test was carried out to determine the hardness of the coating materials in a much reliable manner when compared to microhardness measurement procedures mentioned in Section 4.4.1. The device used for this purpose is the nanohardness testing system manufactured by CSM Instruments Company. The indenter used through the process was a V-F-34 code diamond Vickers model one. The speed of indenter approach on the coated specimens was set to be 2000 nm/minutes. Loading was performed in a linear manner and data recording was held with a frequency of 10 Hz.

During nanoindentation, as the load is increased, indenter sinks into the material due to elastic and plastic deformation. Unlike conventional indentation hardness tests, the size (and hence the projected contact area) of the residual impression for nanoindentation testing is too small to measure accurately with optical techniques. The depth of penetration together with the known geometry of the indenter provides an indirect measure of the area of contact at full load, from which the mean contact pressure, and thus hardness, may be estimated [12].

Plastic deformation is responsible for the permanent shape change, causing the final imprint to reflect the indenter geometry. This deformation causes the depth $h_c$. Elastic deformation results in an additional component of the displacement, such that the surface displaces downward at the edge of the contact by an amount $h_s$ [126]. If the load is held constant, the indenter continues to sink into the material due to time dependent deformation (i.e. creep) [9]. Thus, pause length of the indenter on the coating was determined as 2 seconds to prevent the creep effects from occurring.

Parameters seen on Figure 4.7 and Figure 4.8 denote the following values;

$P_{max}$ : Maximum applied force
$h_{max}$ : Maximum indentation depth
$S$: Contact Stiffness
$h_c$ : Indentation contact depth

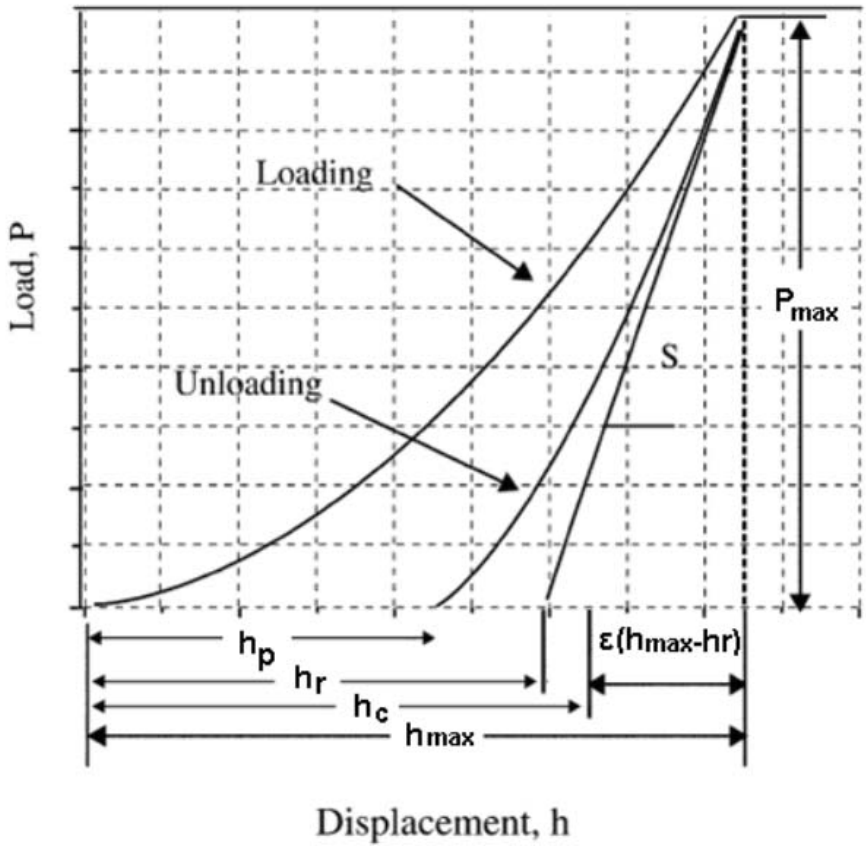


Figure 4.7. Graph denoting the indentation depth variation with load [9, 6]

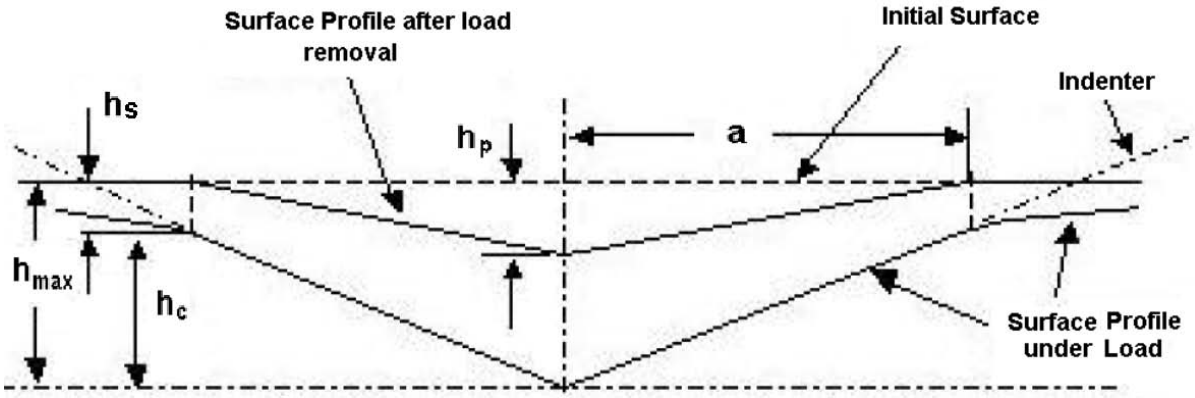


Figure 4.8. Cross section of an indent during nanoindentation [6]

$h_s$ : Downward surface displacement at the perimeter of the contact

$h_p$ : Plastic depth

$h_r$ : Depth of residual impression

a : Radius of the contact circle [9, 6, 126, 12]

Effective hardness and elastic modulus values, taken into consideration to characterize the coatings in this study are the Indentation Hardness $H_{IT}$ and Indentation Modulus $E_{IT}$ values. Calculation of these values from the load and unload curves is performed by the instrument itself, and is based on the famous Oliver and Pharr method [127]. Oliver and Pharr found that the unloading curve follows a simple power law, such as:

$$P = A(h_{max} - h_p)^m \tag{4.8}$$

where $h_{max}$ corresponds to the total depth, which is the sum of $h_c$ and $h_s$. Also, $A$ and $m$ stands for material constants.

Next, contact stiffness is defined as the slope of the initial portion of unloading curve (see equation 4.9) and the contact depth is found to be the range extrapolated from the initial stages of unloading curve [126] (see equation 4.10)

$$S = \frac{dP}{dh} = mA(h - h_p)^{m-1} \tag{4.9}$$

$$h_c = (h_{max}) - (\epsilon)(\frac{P_{max}}{S}) \tag{4.10}$$

Here $\epsilon$ is a geometric constant based on the indenter geometry. For an equivalent conical indenter (e.g. a Vickers or Berkovich indenter with an equivalent conical apex angle of 70.3°), $\epsilon$ is 0.75 [120]. Calculation of $H_{IT}$ to characterize the hardness is done using the formula:

$$H_{IT} = \frac{P_m}{A_p} \tag{4.11}$$

where $P_m$ is the maximum applied load, and $A_p$ is the projected contact area [10].

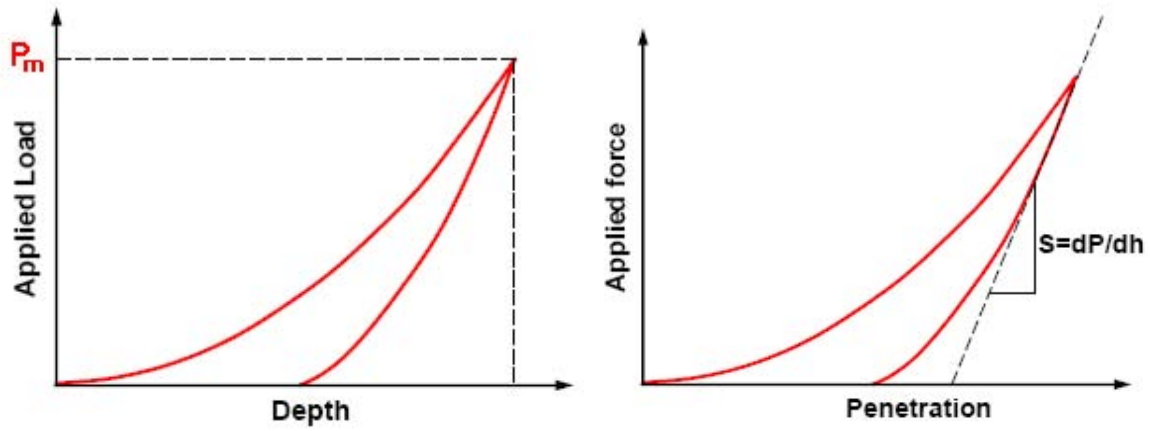


(a) $H_{IT}$ calculation curve (b) $E_{IT}$ calculation curve

Figure 4.9. An example of the load-unload curve for $H_{IT}$ and $E_{IT}$ calculations [10]

Calculation of the modulus is again done by using the unloading curve. Indentation elastic modulus $E_{IT}$ is calculated from the contact stiffness, $S$ (see eq. 4.9) and the projected contact area $A_p$ is determined from the contact depth [10, 127]. Figures 4.9a and 4.9b provide sample load-unload curves for the determination of indentation hardness and elastic modulus values respectively. Reduced modulus (${E_{IT}}^*$) is calculated first, by the relation:

$$ {E_{IT}}^* = \frac{\sqrt{\pi}}{2} \cdot \frac{S}{\sqrt{A_p}} \tag{4.12} $$

Then ${E_{IT}}^*$ is further used for the calculation of the indentation elastic modulus by;

$$ \frac{1}{{E_{IT}}^*} = \frac{1-\nu^2}{E_{IT}} + \frac{1-\nu_i^2}{E_i} \tag{4.13} $$

where the symbols denote the following values:

$E_i$: Elastic modulus of the indenter

$E_{IT}$: Elastic modulus of the subject coating

$\nu_i$: Poisson ratio of the indenter

$\nu$: Poisson ratio of the coating [10]

# 5. RESULTS AND DISCUSSION

Characterization studies were carried out in accordance with the procedures explained in experimental work chapter. For this purpose, research facilities of Boğaziçi University, Atatürk University, İstanbul Technical University, Gebze Institute of Technology and Middle East Technical Univesity R&D Lab was employed. Results of the characterization studies are presented below.

## 5.1. Structural Characterization

Coatings deposited in both runs were gray in color, shiny and visually quite attractive. It is known that some of the wear resistant coatings, such as $TiN$, is coated on parts due to its golden color, just for decorative purposes [29]. Just like this case, DLC coatings of this study could be applied on parts, not only serving wear resistance and such purposes, but also providing a bold look.

### 5.1.1. SEM Results and Discussion

SEM observations were carried out to observe the thickness and structure of the deposited films from fracture surfaces.

5.1.1.1. Thickness Measurements. Thickness of the coatings were measured from the fractured surfaces of Me(Ti,Nb)-DLC coated silicon wafer substrates (see Figure 5.1). Coatings of Run 1 were found to have a thickness value of 1.5 $\mu$m and Run 2, 2.5 $\mu$m.

5.1.1.2. Coating Structure. As explained at section 3.1, expected film growth mode was Zone I type, according to Thornton's classification. In accordance with the theory, domed topes with columnar structures are observed. However voids were not observed between columnar features.

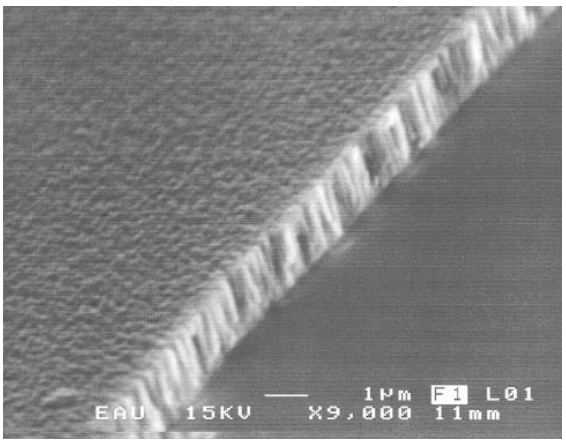


(a) Run 1 (1.5 $\mu$m)

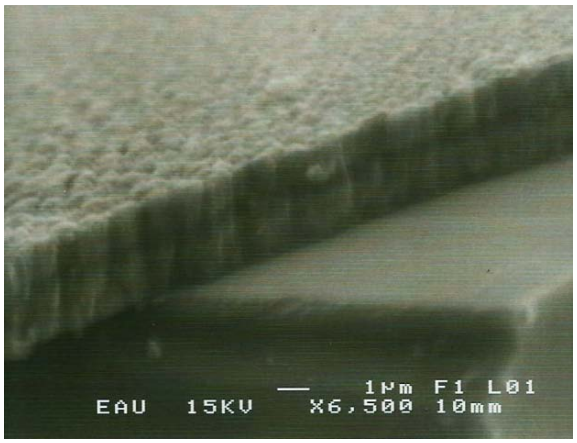


(b) Run2 (2.5 $\mu$m)

Figure 5.1. SEM crossection image of Me(Ti,Nb)-DLC coatings

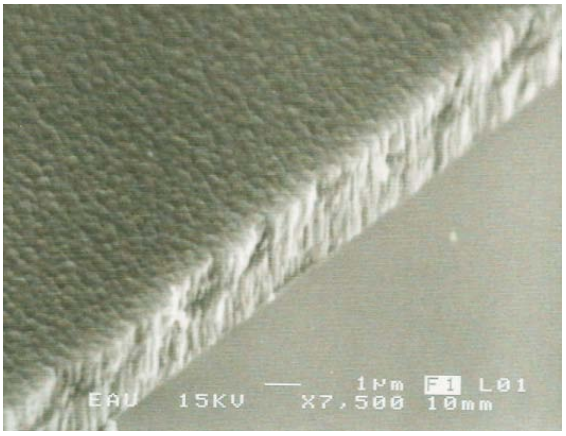


(a) 7500 magnification

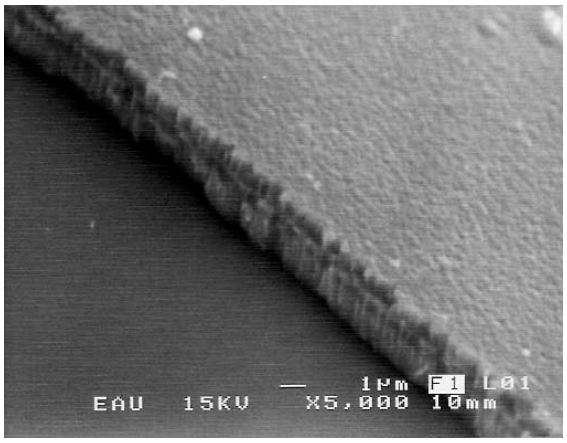


(b) 5000 magnification

Figure 5.2. SEM images of Me(Ti,Nb)-DLC coatings

### 5.1.2. Roughness Results and Discussion

Substrate materials, as mentioned before, were composed of 3 different materials; M2 high speed steels, glass slides used in microscope studies and silicon wafers. Glass slides and silicon wafers were used in the as-manufactured manner; polishing or etching or any sort of substrate preparation operations were not carried upon them.

The default surface roughness regarding the glass slides is shown in Figure 5.3. Roughness parameters seen on the roughness measurement outputs denote the values given in 5.1. It is seen that the $R_a$ roughness of glass samples are 0.01 $\mu$m on average and are quite smooth, when compared with M2 HSS samples. It should be noted that

the y axis magnification of this surface profile output is 100 times.

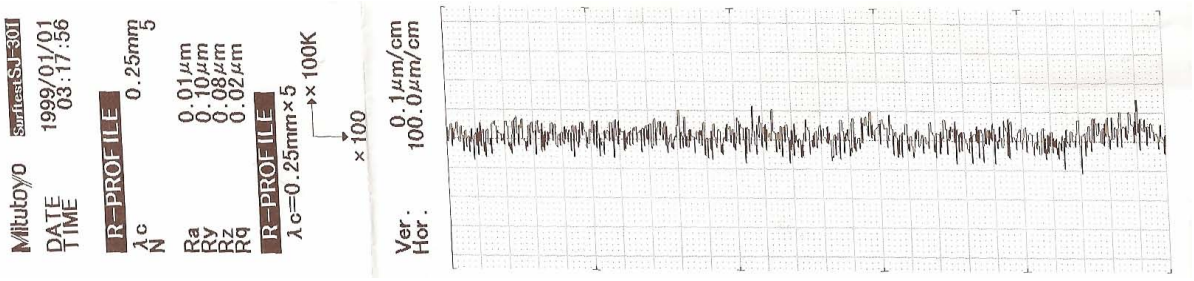


Figure 5.3. Glass substrate, roughness before coating deposition $R_a$=0.01$\mu$m

Table 5.1. Roughness Parameters [15, 16]

| Parameters | Description | Standard |
|---|---|---|
| $R_a$ | Roughness average | BS 1134 ISO 4287 DIN 4768 ANSI B46.1 |
| $R_y$ | Maximum roughness depth | BS 1134 ISO 4287 DIN 4762 |
| $R_z$ | Mean peak to valley roughness | DIN 4768 |
| $R_q$ | RMS roughness average | ISO 4287 DIN 4762 |

Other type of substrate was M2 high speed steel. It was noted before that there were two different sets of coatings, first called as Run 1 coatings with 1.5 $\mu$m of thickness and second set called as Run 2 with 2.5 $\mu$m thickness. In these runs, samples were prepared with different surface roughnesses. In Run 1, samples were prepared to reach $R_a$=0.08 $\mu$m .

Since resulting coatings of the first run were possessing moderate adhesion values, in the second run, it was desired to attain better surface roughness values. To achieve this, substrate grinding and polishing sequences were repeated twice and each sample was individually checked before initiating the coating procedure. Also in the second sample preparation process, an additional microetching was employed. Resulting surface roughness profiles for the samples of coating Run 2 are as follows:

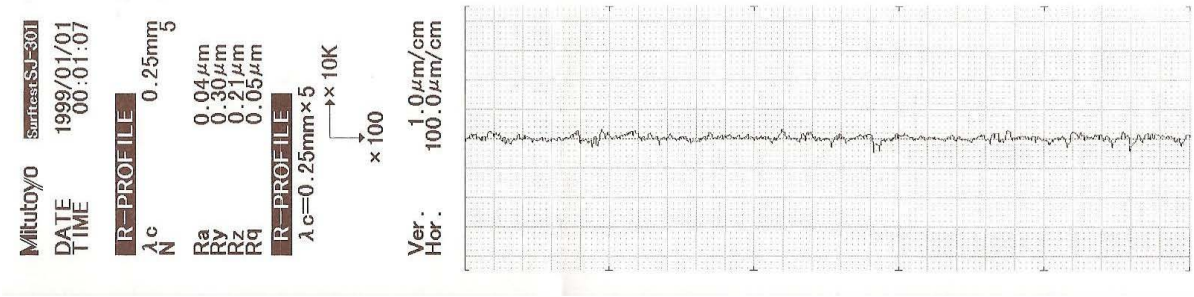


Figure 5.4. M2 HSS substrate, surface roughness before Run 2 $R_a$=0.04$\mu$m

Here it is seen that the surface roughness (with $R_a$=0.04 $\mu$m), is quite improved when compared to the first run. Consequences of this improved surface roughness will be apparent once wear profiles are examined and critical loads for adhesion tests are gathered. For easier comparison with glass slides, below added is the same profile in Figure 5.4, with y axis magnification increased to 100 times. Although the roughness values were improved, still they are out of league when compared to glass slides. As mentioned in section 4.1.1, roughness might indeed prove beneficial in improving adhesion of the interlayer and these results should not be discouraging.

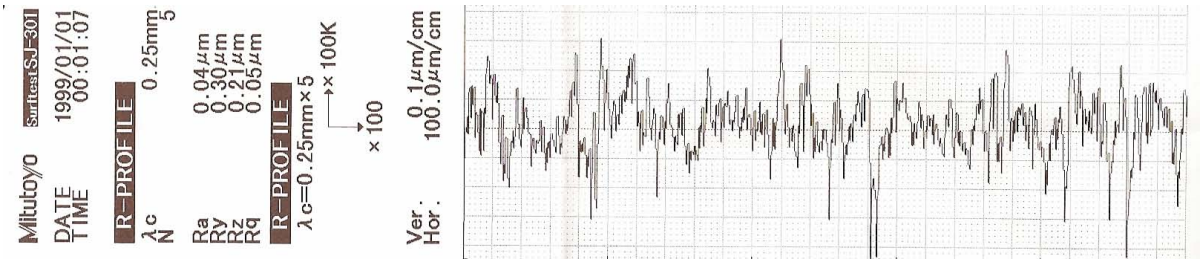


Figure 5.5. Same profile in Figure 5.4, increased y axis magnification

When surface roughness evolution after the coating process is considered, we see a tendency to increase. This is in agreement with the literature [11], which could be quoted as;

> "In the beginning of the deposition, the DLC film roughness tends to increase, becoming larger than the original roughness of the substrate surface. But as the DLC film grows thicker, the roughness growth decreases. This is mainly due to filling of the valleys (check Figure 5.6)... Note that this roughness behavior, occurs only for thin DLC films, that is, for d<200 nm. For thin films the dynamic

growth process depends critically on the initial substrate roughness [128]... However, for thicker films [129, 130] memory of the initial substrate roughness is lost and the film roughness increases with film thickness."

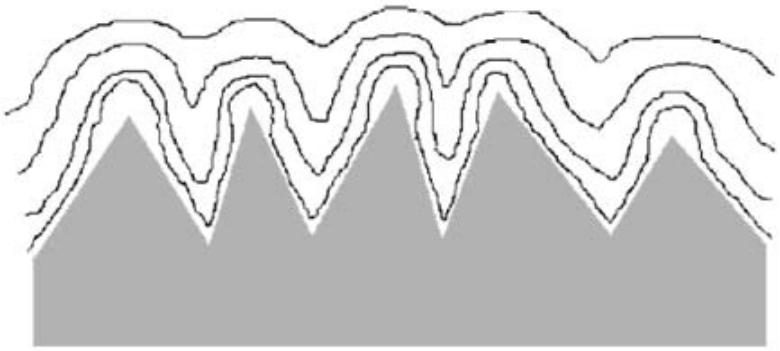

Figure 5.6. Illustration of a rough substrate with the successive DLC depositions [11]

It was noted before that, there were two runs in this study. Both runs, with 1500 nm and 2500 nm of average film thickness will be considered as thick films with the classification of Salvadori et al., 2006 [11]. Results the coatings, exhibiting an increase of roughness after the completion of the coating process, are presented below and are in accordance with the investigations of Salvadori et al. in 2006 [11], Barabasi in 1995 [129] and Kardar et al.in 1986 [130].

For Run 1, roughness evolution showed that the measured $R_a$ value increased from 0.08$\mu$m to 0.09$\mu$m after coating deposition. Below added are the surface roughness profiles of the coatings for Run 2. As a reminder;

- Glass substrate: initial roughness: 0.01$\mu$m
- M2 HSS Substrate: initial roughness: 0.04$\mu$m

Here it should be noted that the resulting roughness value is increased up to $R_a$=0.11 $\mu$m from 0.04 $\mu$m for the M2 substrate in Run 2, whereas the roughness increase for Run 1 M2 substrates were limited with an increase from $R_a$=0.08 $\mu$m to 0.09 $\mu$m. This result shows that increasing coating thickness is a significant parameter in surface roughness evolution, since it caused a twofold increase in roughness when the coating thickness is increased from 1.5 $\mu$m to 2.5 $\mu$m.

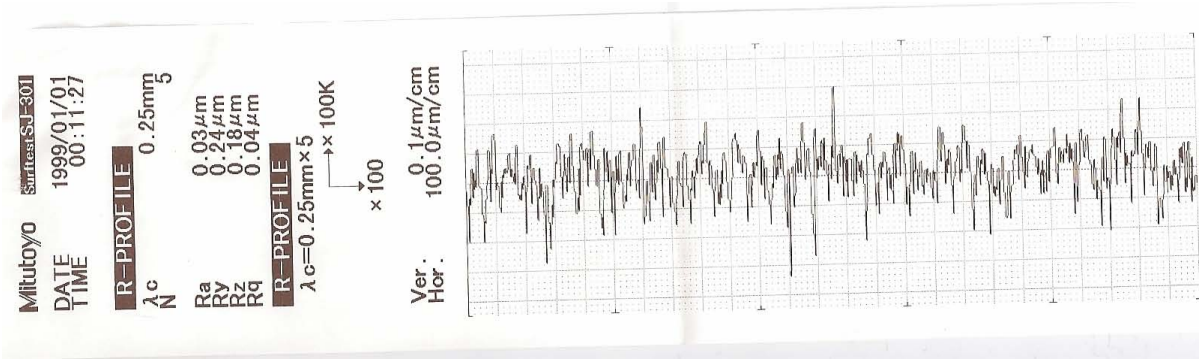


Figure 5.7. Me(Ti,Nb)-DLC coating on glass, roughness $R_a$=0.03$\mu$m after Run 2

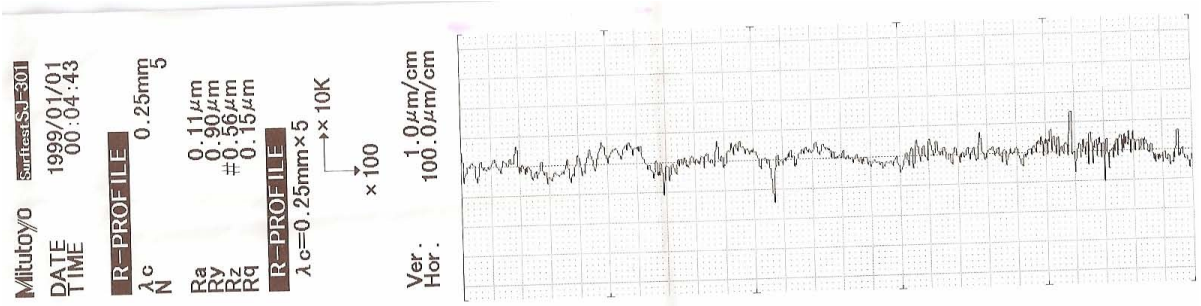


Figure 5.8. Me(Ti,Nb)-DLC coating on M2, roughness $R_a$=0.11$\mu$m after Run 2

It is stated in the literature that, when DLC is deposited on a smooth surface such as the silicon substrate with low roughness, very small hills and valleys are formed and the roughness remains approximately constant with film thickness [11]. In our case, coating thickness is over 1000 nm and validity of this statement is not for sure. Further experiments should be carried out to determine the roughness evolution of Me-DLC on Si substrates, however surface roughness measures regarding the silicon wafers or coated Si samples are not supplied in this study.

A more precise surface roughness study is conducted by employing Atomic Force Microscopy. Atomic force microscopy (AFM) is a non-destructive proximity scanning probe technique used to profile a small area of a sample surface to a very fine depth resolution. A sharp tip mounted on a flexible cantilever is scanned over the sample surface of a few microns square area by piezoelectric drive circuitry [131]. Scanning was done with tapping contact mode, patented technique of Veeco Instruments. To provide a brief information regarding the tapping mode and AFM working principles, PhD Thesis work of Chowdhury is referred.

> "In the tapping mode, the tip is vibrated at its resonant frequency and is scanned over the surface. Interaction with surface morphology causes a modulation in the vibration of the tip. The vertical motion of the tip flexes the cantilever, and the amount of deflection is detected by the reflection of a laser beam focused on the back of the cantilever. As the tip is deflected, the reflection angle of the laser is changed, which is measured in a position sensitive photodetector system consisting of two side-by-side photodetectors. The tip deflection information is then amplified and used to form an image by scanning in the same way as the surface is scanned by the tip. The data can be presented as a 2-dimensional height profile and can be processed to determine a variety of information such as surface roughness [131]."

Tapping mode also eliminates lateral shear forces that reduce image resolution and damage samples [132]. Observations were carried out by scanning a $20\mu m \times 20\mu m$ area of Run 2 Me(Ti,Nb)-DLC sample coated on glass. As a result of the scanning, surface topography seen in Figure 5.9 is generated.

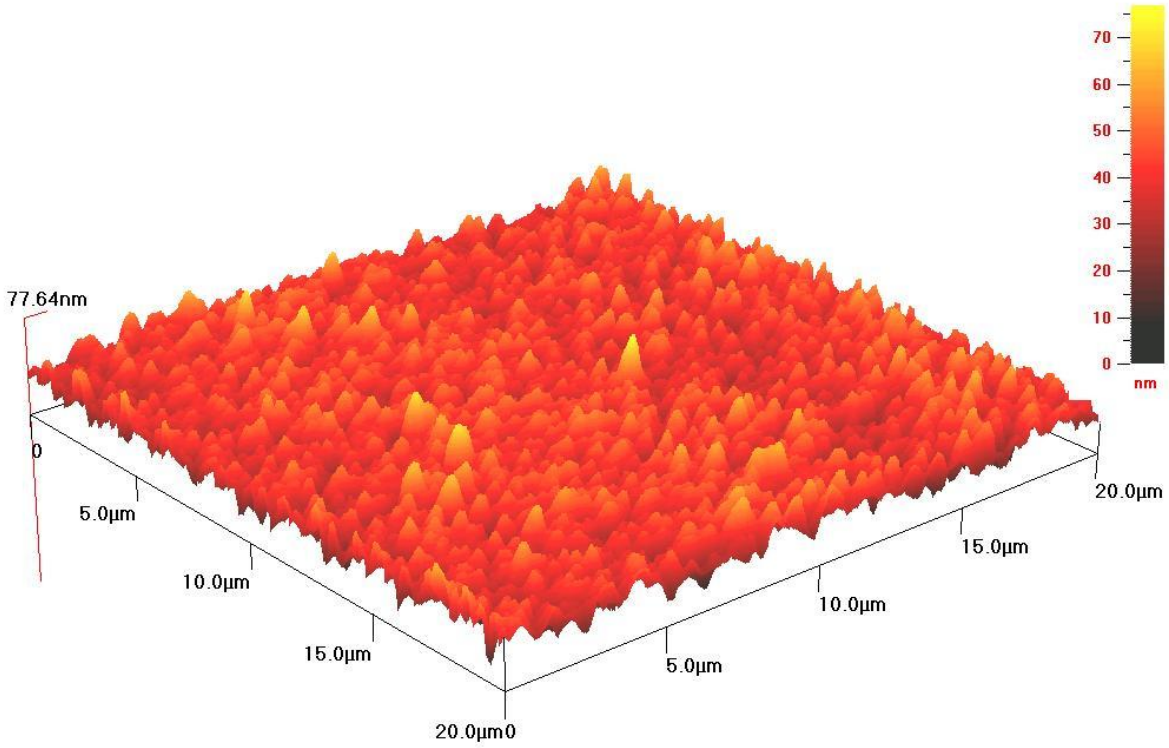


Figure 5.9. Surface topography generated by AFM scanning procedure

There are many supplementary information supplied by AFM scanning other than the surface topography. Aim of these data is to give an insight of the surface structure and support these findings with numerical data for comparison. In Figure 5.10 the histogram of the scan is added.

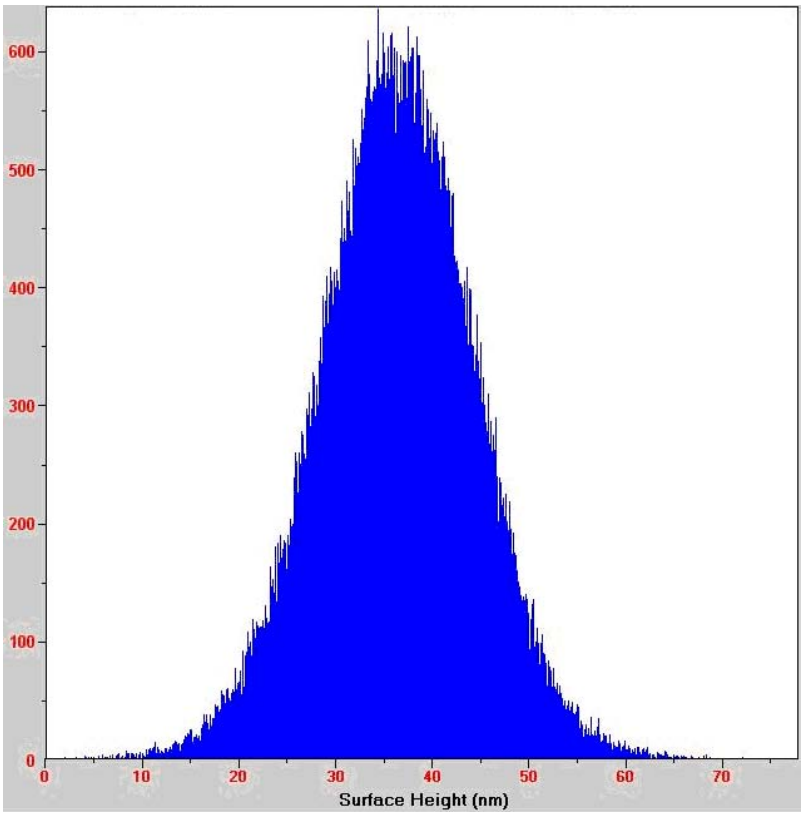


Figure 5.10. Surface topography generated by AFM scanning procedure

The Height Histogram displays the frequency distribution of the Z-height of all points in the image, i.e. the height of the column at some particular "Surface Height" shows how many points of that height are present in the image. The height equal zero is assigned to the lowest point [133]. Surface roughness and structure parameters, pertaining to the Run 2 coatings on glass substrate are given in Tables 5.2 and 5.3.

Comparing the results obtained with regular surface profilometers, it is noted that the average roughness value is extremely low for AFM measurements. $R_a$ was measured as 0.3 $\mu$m with a profilometer, whereas this value corresponds to the average height value in AFM. $R_a$ value was measured to be 6.376 nm with AFM, which is

Table 5.2. Surface roughness parameters measured by AFM imaging

| Parameter | Value (nm) |
|---|---|
| Average Height | 36.18 |
| RMS Deviation | 8.009 |
| Mean Deviation | 6.376 |
| $R_p$ | 41.46 |
| $R_v$ | 36.18 |
| $R_t$ | 77.64 |
| 10 point mean ($R_z$) | 77.64 |

Table 5.3. Descriptions of the parameters given in Table 5.2

| Parameter | Description |
|---|---|
| Average Height | Mean of Z-heights of all the points in the scan with respect to the lowest point [133] |
| RMS Deviation | Roughness average, Rq or RMS is the root mean square measurement of the peaks and valleys deviations or departures from the centerline over the sampling length [16] |
| Mean Deviation | Average deviation from the mean surface plane. Also called as average roughness, $R_a$ [133] |
| $R_p$ | Maximum peak height; maximum height of the profile above the mean line within the sampling length [16] |
| $R_v$ | Maximum valley depth; maximum depth of the profile below the mean line within the sample over the entire set of readings [16] |
| 10 point mean ($R_z$) | Average absolute value of the five highest points and five lowest valleys over the evaluation or assessment length [16] |

almost one fifth of surface profilometer reading. Since the AFM device is not fully utilized, as explained in Section 4.1.1, it wasn't possible to conduct further studies regarding this discrepancy.

The reason however, is probably due to the different quantities being expressed with the same term. Although $R_a$ is defined as the mean deviation from the surface plane, it was also seen in the literature [134] that $R_a$ value was expressed as the mean vertical distance between the valleys and the hills in the surface profilometers. In this case, what is called as average roughness is actually nothing but the average height measured. Correct roughness measure (average roughness, $R_a$) is reached by atomic force microscopy and is noted as 6.376 nm.

Besides Ra, there are two parameters, kurtosis and skewness, which can be used to assess a surface height distribution [135]. Kurtosis is a non-dimensional factor used to represent the shape of the distribution. Graphically, kurtosis indicates whether data are arranged flatly or sharply about a central mean. A Gaussian height distribution has a kurtosis of 3. If $K < 3$, the distribution has few high peaks and low valleys, which means a relatively flat surface. If $K > 3$, the distribution has many high peaks and low valleys, which means a relatively sharp surface [136]. Kurtosis value measured in this study is 0.380, indicating a good measure of flatness.

Skewness measures the symmetry of surface data about a mean data profile. A surface with zero skewness has as many peaks as valleys of the same height and depth. Profiles with sharp spikes have positive skewness, while profiles with deep pits have negative skewness [136]. Skewness value measured in this study is -0.016, indicating the dominance of deep valleys over sharp peaks.

## 5.2. Compositional Results

Novel aspect of the coatings deposited in this study, is the addition of titanium and niobium dopants at the same time. This causes significant changes in the microstructure of the coating, where not only *C*, *N* and *Ti*, *Nb* interaction happens, but also *Ti* and *Nb* interactions are important. In this section, the compositional characterization is carried out by employing XRD and XPS analyzes.

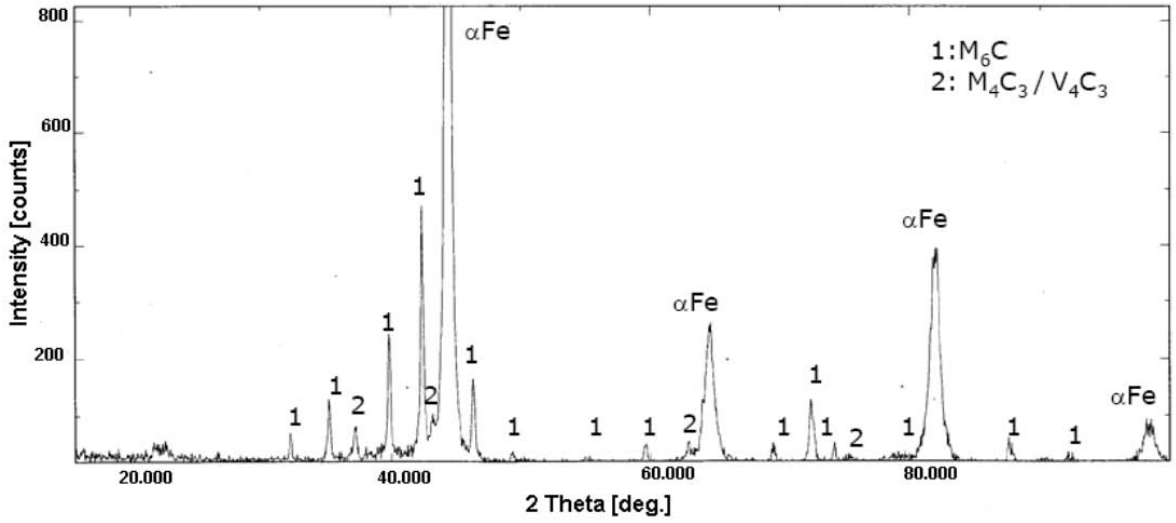


(a) M2 HSS substrate

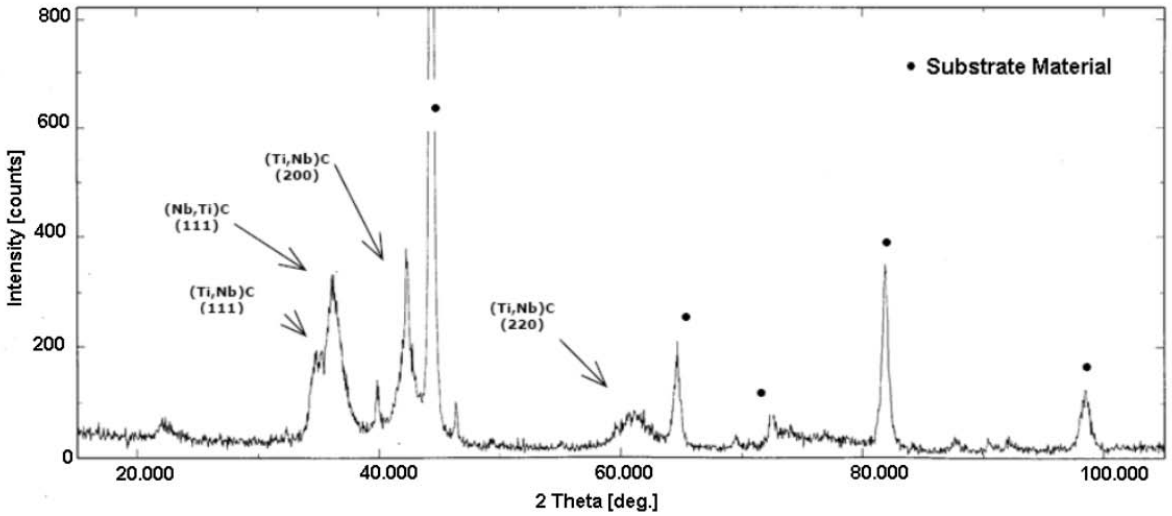


(b) Me(Ti,Nb)-DLC coating

Figure 5.11. XRD of the substrate alone and the substrate-coating couple

### 5.2.1. XRD Results and Discussion

As a result of the XRD analysis, it was desired to determine the chemical composition of the coating material and the substrate (substrate in this case was a M2 high speed steel). The nature of the carbide phases (i.e. directional crystallization preference of various participants of the coatings) were also to be investigated.

In Figure 5.11a, XRD spectra of M2 HSS is supplied, which is assessed in the light of Joint Committee on Powder Diffraction Standards (JCPDS) references. In this

spectra, it is clearly seen that the $\alpha$-ferrite crystal planes have the highest intensity among all other signals. Other than $\alpha$-ferrite signals, $M_6C$, $M_4C$ and $V_4C$ carbide phases are also noted.

When the coating diffraction spectrum was examined, as mentioned in Section 4.2.1, there is a marked interference from the substrate material. Since these signals were determined by the prior substrate XRD survey, signals transmitted by the coating-alone were pinned out. Other than the substrate signals, partial crystallization regarding the DLC phases (still coatings should be regarded as amorphus) are seen in the XRD spectra of coated substrates (see Figure 5.11b).

XRD spectra presents various peaks regarding *TiC*, *NbC* and *TiC(Nb-N)* reflections. *TiC* has distinct features resident at 42.350 deg., 36.3 deg. and 61.150 deg., sorted with respect to their intensities. JCPDS references of these peaks are at 41.708 deg., 35.904 deg. and 60.446 deg. respectively corresponding to $TiC(200)$, $TiC(111)$ and $TiC(220)$ phases. $TiC(220)$ peak presents a strong shift from the JCPDS reference, which is attributed to doping agents (nitrogen and niobium) getting trapped in *TiC* crystals with a significant amount. Still, further studies should be carried out to determine this content quantitatively. Also for *NbC*, there were peaks resident at 34.729 deg. for $NbC(111)$ and 40.314 deg. for $NbC(200)$, which are resident at the reflections on the left of *TiC* peaks.

When the XRD spectra is examined, generally low signal intensities are seen. It could be concluded that the overall structure of the coating is close to an amorphus structure, which is confirmed by the SEM observations noted in section 5.1.1 on page 53.

### 5.2.2. XPS Results

Measurements were performed by using an Al-$K_\alpha$ source with excitation energy 1486.6 eV and 540 W for near surface analysis. XPS measurements were carried out to investigate the carbon hybridization behavior and microstructural investigations of

mainly carbon based environments.

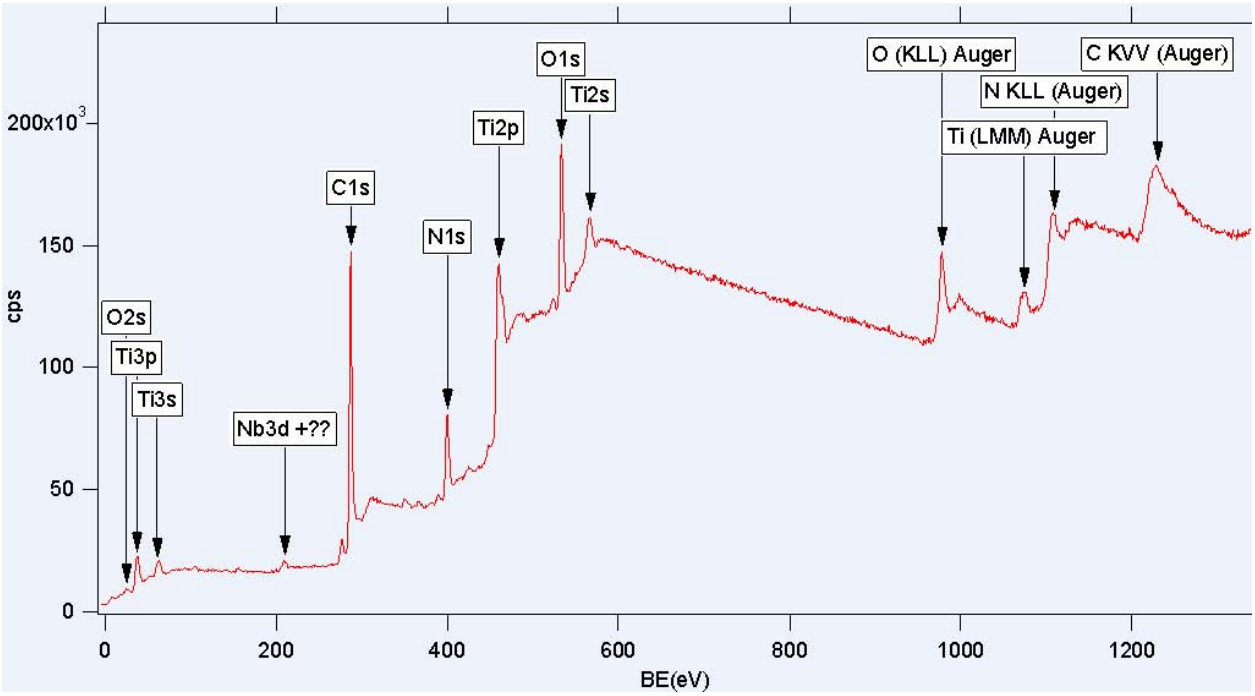


Figure 5.12. XPS Survey of the ME-DLC coating Run 1 (Substrate: M2)

Figure 5.12 shows the spectra of the first run obtained from Gebze Institute of Technology, where a general surface survey was performed. Unlike the studies conducted in METU, this single spectra was taken after a sputtering process; there was no information supplied for the initial state of the coating. There are visible peaks that belong to *Ti*, *Nb* and *C* elements, whereas, there are also significant *O* peaks, indicating an oxygen contamination. Several windows (C1s, N1s, Nb3d, O1s, Ti2p) were rescanned to get detailed information about elemental peaks (see Figure 5.13 a to e). Still the exact phase corresponding to *Nb* was not determined by the scientist. This might be due to the peaks identified with the 3p and 3d orbitals appear to be split into two component peaks, thus the scientist wasn't able to identify the peak individually [137].

Figure 5.14 shows the general survey scan of a Run 1 coating coated on a glass substrate, this time obtained from METU R&D Labs. Figure 5.14a shows the spectra received in the original state of the coating without any process, which possesses the highest carbon content (63.1 at%) among all pre-sputter samples. This measurement

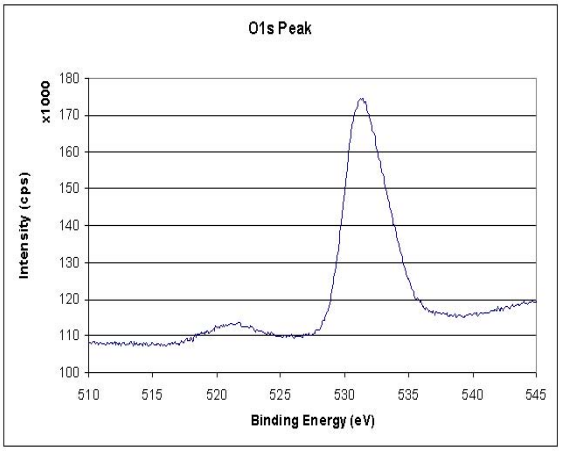


(a) Oxygen peak

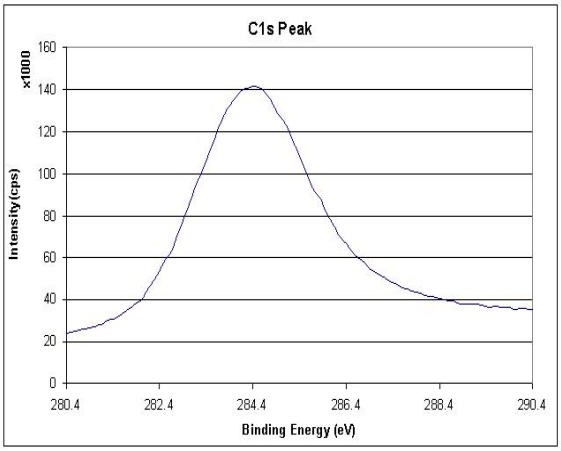


(b) Carbon Peak

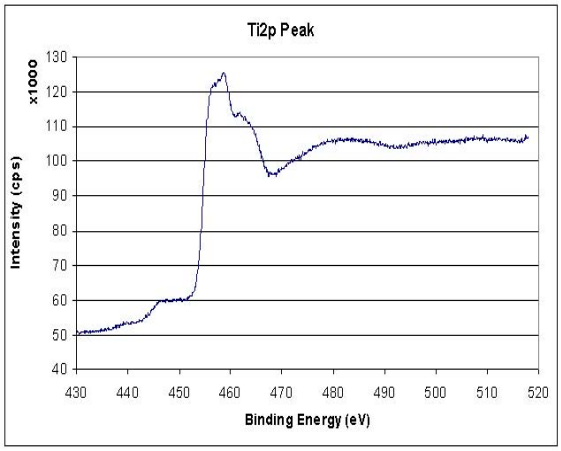


(c) Titanium peak

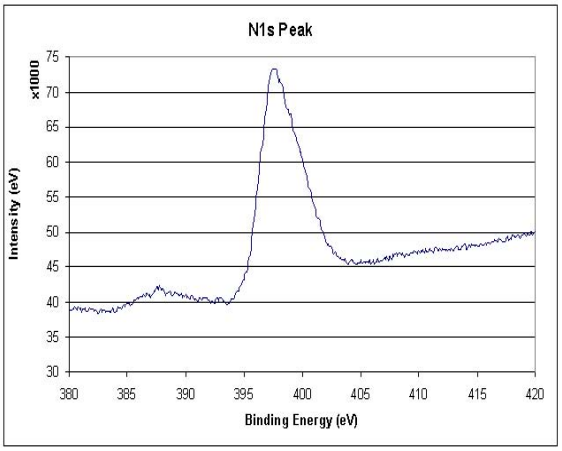


(d) Nitrogen peak

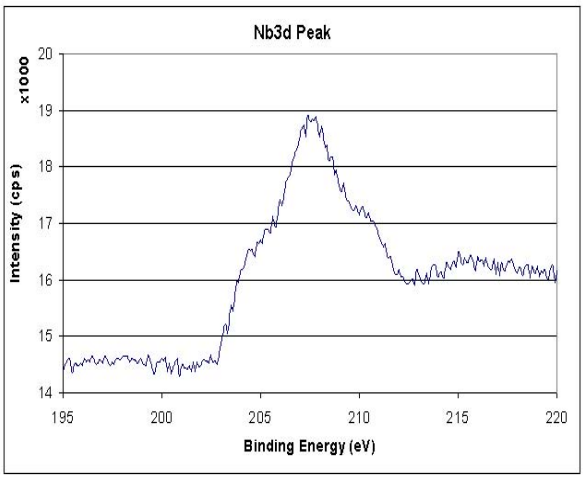


(e) Niobium peak

Figure 5.13. XPS windows for different constituent materials

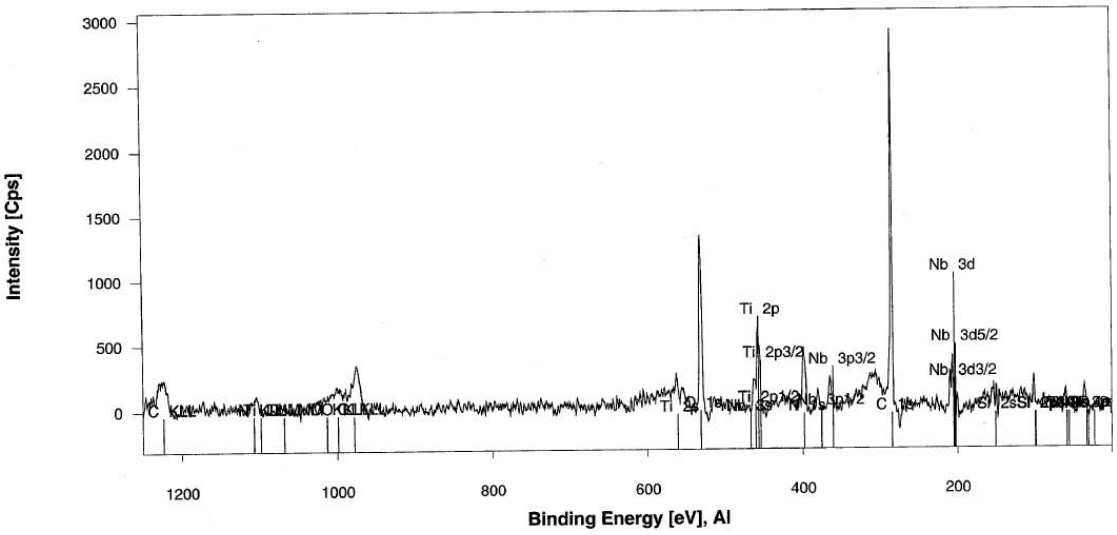


(a) Before Sputter

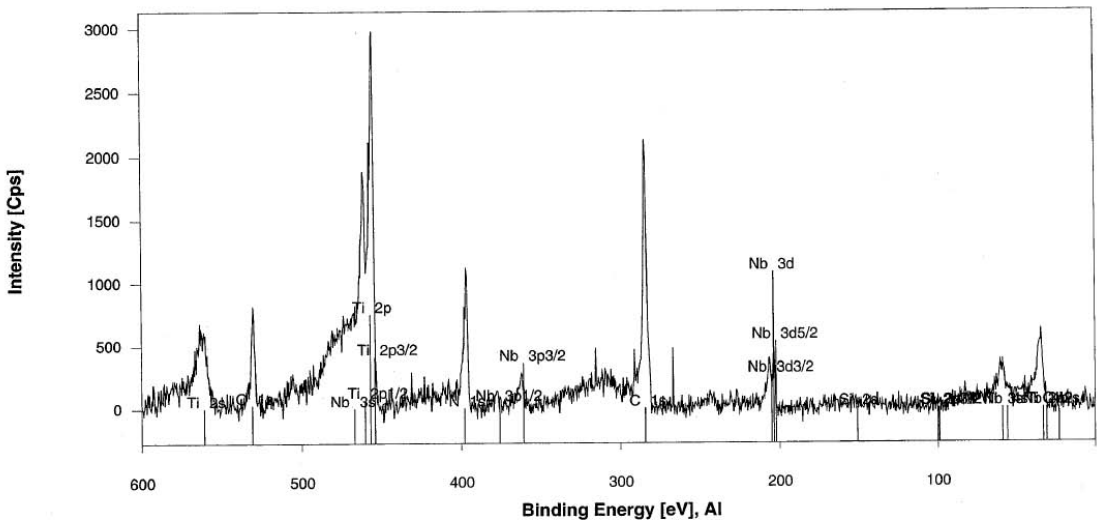


(b) After Sputter

Figure 5.14. XPS of ME-DLC Run 1 coating on glass, before and after sputtering

was taken by applying an excitation of 540 W.

To get rid of hydrocarbons, oxidations and other contaminations, a sputtering procedure was carried out. Sputter agent was Argon and the process took 4 minutes with 2000 eV and an excitation of 10 W. Figure 5.14b denotes the spectra received after sputtering. It should be noted that the spectra of the first figure was taken between 0-1250 eV, whereas the range was decreased to 0-600 eV after sputtering. It was initially seen that carbon peak is the dominant peak. After sputtering, there is a decrease in the relative intensity with a pronounced increase in the titanium peak

intensity. This is thought to be due to the partial removal of DLC layers from the 1.5 $\mu$m coating, giving rise to titanium and niobium signals to be transmitted strongly from the underlying *TiC* and *NbC* layers, along with nitrogen signals coming from *TiN* and *NbN* species.

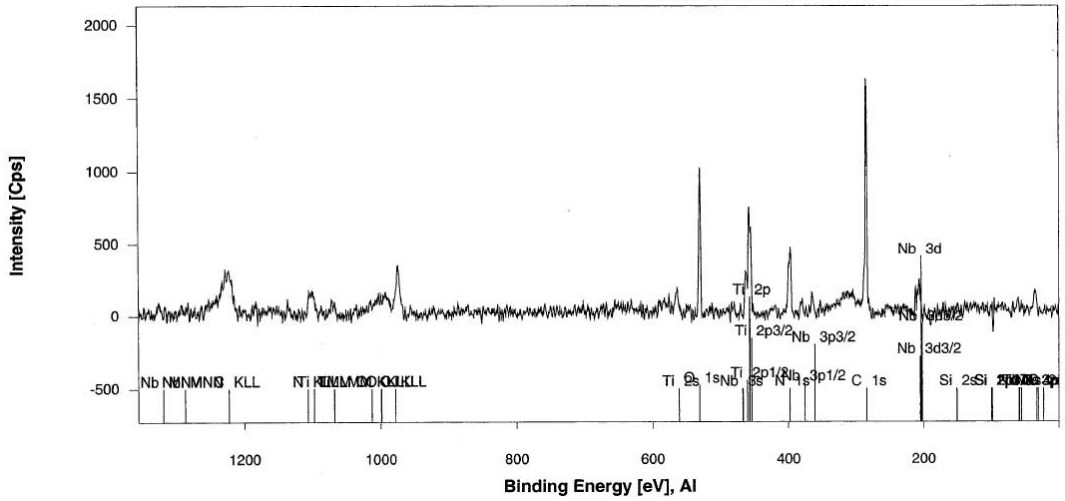


(a) Before Sputter

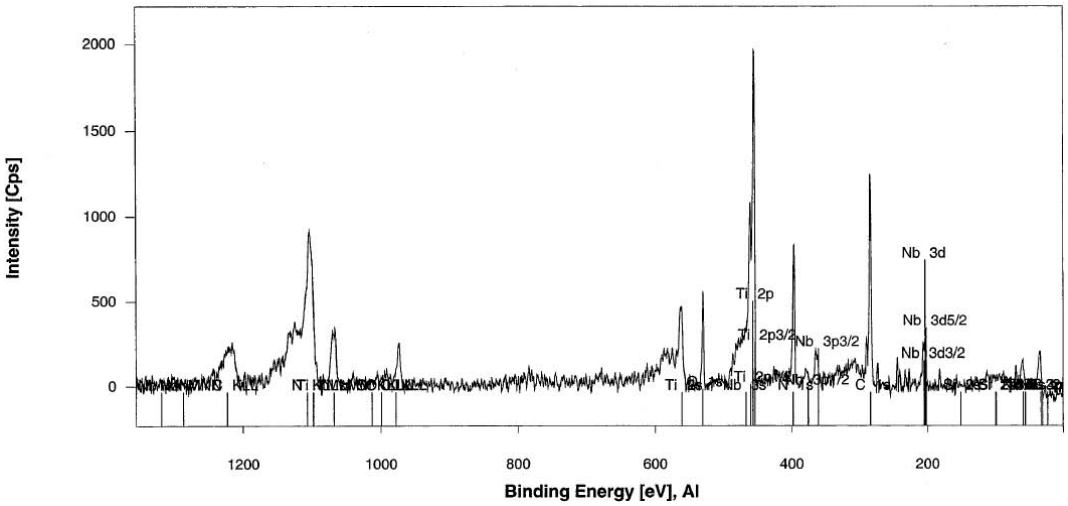


(b) After Sputter

Figure 5.15. XPS of ME-DLC Run 2 coating on Si wafer, before and after sputtering

When the spectra of the *Me(Ti,Nb)-DLC* film coated on a silicon wafer substrate in Run 2 is studied (see Figure 5.15), same patterns were observed as in the Run 1. There was a sound carbon peak initially, whose intensity was decreased along with the sputtering procedure. Again *Ti*, *Nb* and *N* peaks were seen to have enhanced intensities after sputtering. When oxygen peaks were examined, it was noted that

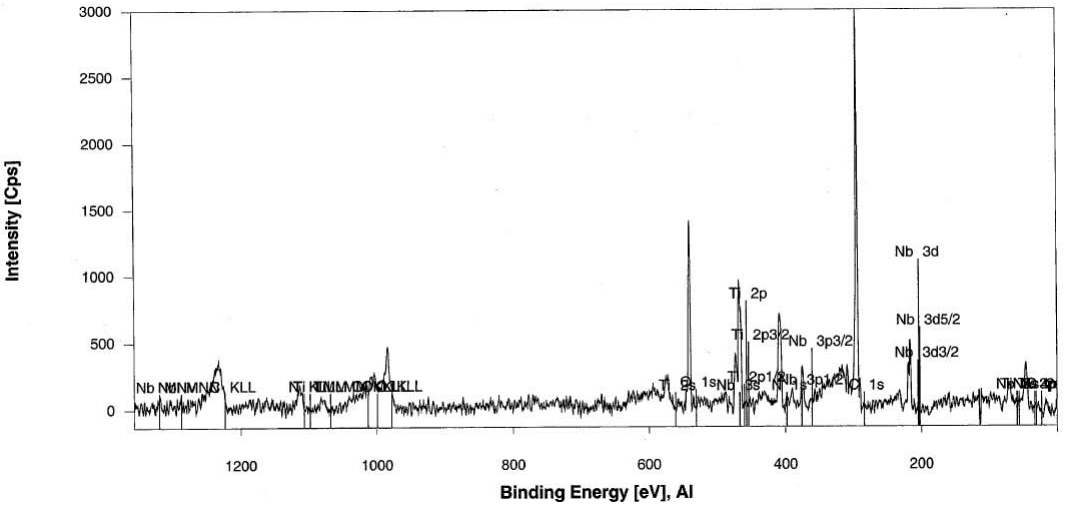


(a) Before Sputter

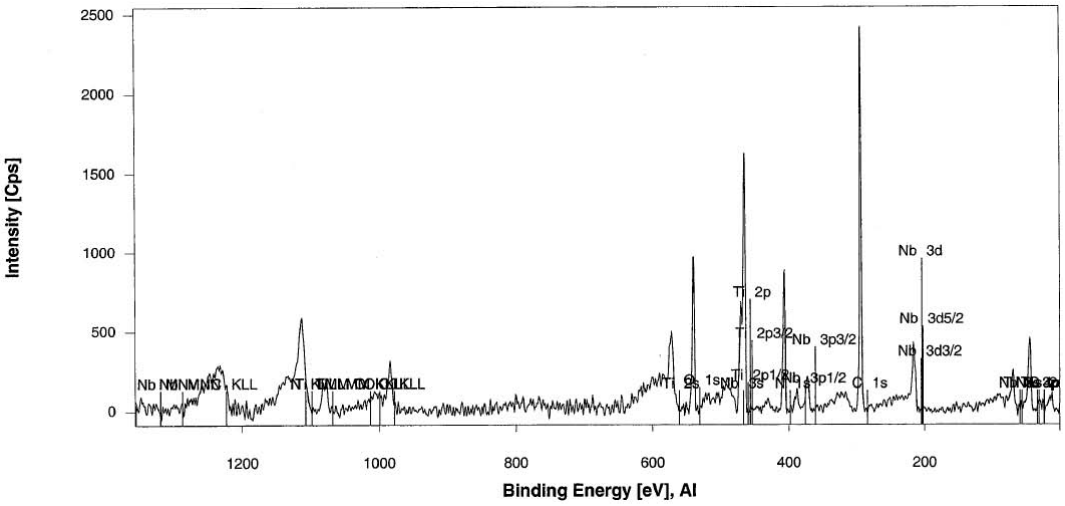


(b) After Sputter

Figure 5.16. XPS of ME-DLC Run 2 coating on glass, before and after sputtering

there existed a significant decrease in contamination with sputtering. This decrease in the intensity was the largest one in all samples examined in XPS. O1s peak, having initially a peak intensity around 1000 cps was reduced almost half its intensity, drawing back to 500 cps level. Still it was not possible to exterminate oxidation contamination, since oxidation became evident again with electron bombardment.

Same conclusions were drawn for coatings on glass substrates for Run 2 (see Figure 5.16. Significance of this coating is that it possessed the highest carbon content among all other coatings, measured as 62 at% even after sputter.

Most important of the XPS windows to determine the character of the DLC film deposited, is the carbon peak under any case. This peak could be used to derive the nature of the carbon bonds and hybridizations, since the locations of the peaks are formed by the superposition of various peaks indicating $sp^2$ and $sp^3$ bonded carbon. It is noted in the literature that [138] the *C–C* $sp^2$ peak is located at 284.4 eV, *C–C* $sp^3$ at 285 eV (noted at 285.2 in [115]), and *C–O* surface contamination at 286.8 eV (again noted at 286.5 in [115]). When carbon windows of XPS spectra after sputter are examined, it is seen that for all 3 deposition samples, the peak is located at exactly 284.4 eV. It is thus correct to say that the DLC coatings developed in this study were composed of almost only graphitic character. Despite the negative effect this character has on the measured hardness values, it does benefit wear resistance by lowering the coefficient of friction and wear rates. These windows are supplied in Figure 5.17

Semi quantitative analysis of XPS outputs are generally performed by carrying extensive peak fit procedures on selected windows. A distinct single peak usually consists of many peaks, whose intensities, mean values and standard deviations are determined by peak fit procedures. There are special softwares designed for the peak fitting of XPS-ESCA spectra only, which are supplied with XPS devices to laboratories. However through this study, GYTE or METU was not able to supply any fits, although peak positions and prospective compounds were supplied. On the other hand, thanks to the guidance of Prof. Dr. Sezai Saraç from Chemistry Department of İstanbul Technical University, qualitative conclusions were drawn from the spectra. Still the peaks require further fitting analyzes for the exact determination of phase compositions and stoichiometry.

There were marked peaks in the spectra indicating compounds of mainly oxide nature. There existed a peak located at 207.4 eV for Run 1 and 206.4 eV in the survey scan for Run 2 belonging to the *Nb* window. When literature [139] was scanned, it was found that this peak corresponded to $NbO_2$ phase. This peak is evident in all survey scans. There were also another peak corresponding to possibly *NbO* phase, located at 203.8 eV for Run 2 (*NbO* noted to be located at 204.1 eV in [139]). If a further peak fit is conducted, a similar peak would be pinned also for the niobium window of

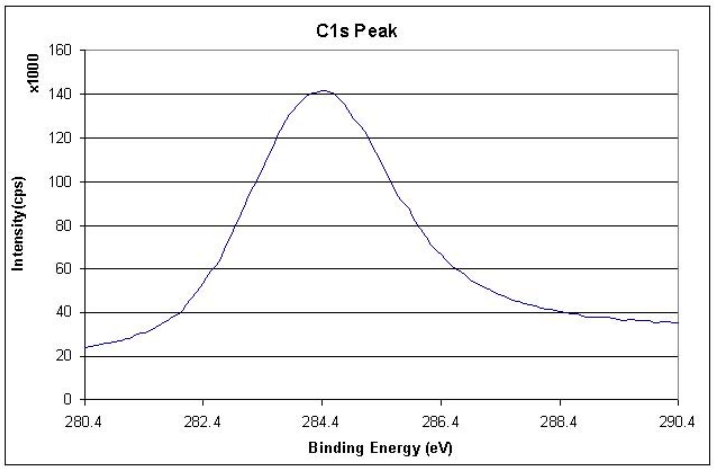


(a) Run1, glass substrate

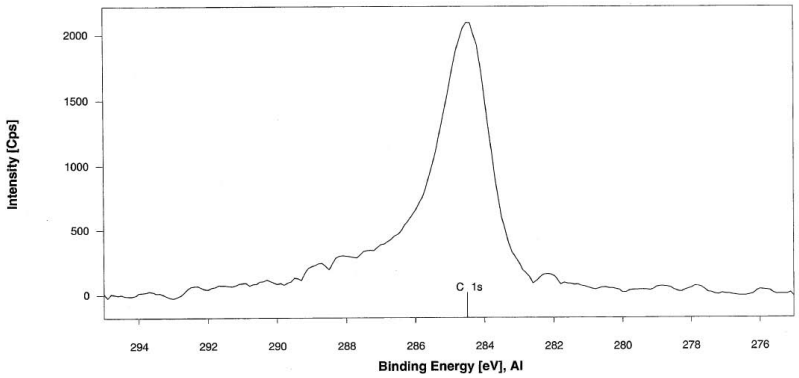


(b) Run 2, Silicon substrate

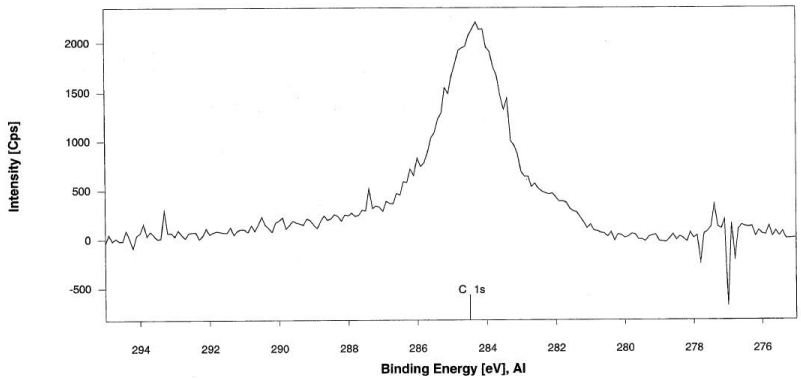


(c) Run 2, glass substrate

Figure 5.17. XPS data regarding the DLC carbon peaks

Run 1, which is a clear superposition of smaller peaks (see Figure 5.13e), possibly a combination of *Nb* 3d/2, *Nb* 3d and *Nb* 5d/2 character.

Likewise a N1s window study was conducted and it was found that before sputter and after sputter peak locations and shapes differed to great extent. Before sputter, there was a flatter peak, composed of the superposed effect of two peaks. In a study

conducted by S. Ismat Shah [140], it was stated that N1s peak for $N$ doped $TiO_2$ species ($TiO_{2-x} - N_x$) was a broad peak extending from 397.4 to 403.7 eV. It was also written that N1s peak for substituted nitrides (ex. $TiN$) is usually a sharp peak, located at 397 eV. Clearly our peak, which is a combination of a sharp peak at 397 eV and a broader peak at the 397.4 to 403.7 eV span, indicates an oxidation contaminated titanium $TiO_2$ phase, along with a sharp signal from substituted nitrides. This signal would be coming from strongly $TiN$ since titanium is the dominant metal dopant, whereas the effect of $NbN$ and other $TiCN$ type compounds should be further investigated. Titanium window should also be peak fitted by the light of table 5.4 to determine the exact compositions of these phases.

Table 5.4. Binding Energies of titanium compounds [17]

| Binding Energy (eV) | 453.9 | 454.9 | 455.1 | 455.8 | 457.8 | 458.8 | 460.0 |
|---|---|---|---|---|---|---|---|
| Phase | $Ti$ | $TiC$ | $TiO$ | $TiN$ | $Ti_2O_3$ | $TiO_2$ | $Ti(2p_{1/2})$ |

X-Ray Spectrometers also have a features to supply information about the elemental composition of the materials. This analysis could be used to determine the composition of the thin film coatings at the surface alone (as thin as 5 nm), or by carrying out sequential sputtering processes and recording the elemental compositions reached, elemental depth profiles could be composed. Since the latter needs technical background and proficiency in this process, elemental profiling process wasn't carried out in GYTE or METU.

In tables 5.5, 5.6 and 5.7, elemental compositions of Me-DLC coatings, before and after the sputtering procedure are supplied. There is a pronounced carbon content in all coatings as expected, which decreased with the sputtering process. This result was anticipated, since the DLC coating deposition was initiated after the completion of carbide phase growth. As the sputter process removed more layers of DLC, underlying carbide phase signals became more powerful in the spectra. Highest decrease in the carbon content (3.4%) was observed for the films of first run. This was related to the

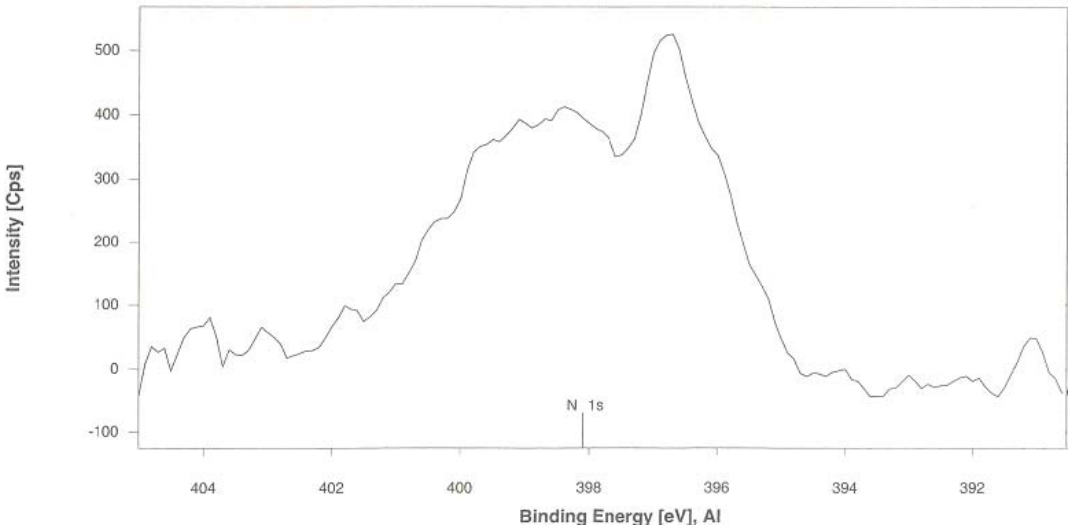


(a) Before Sputter

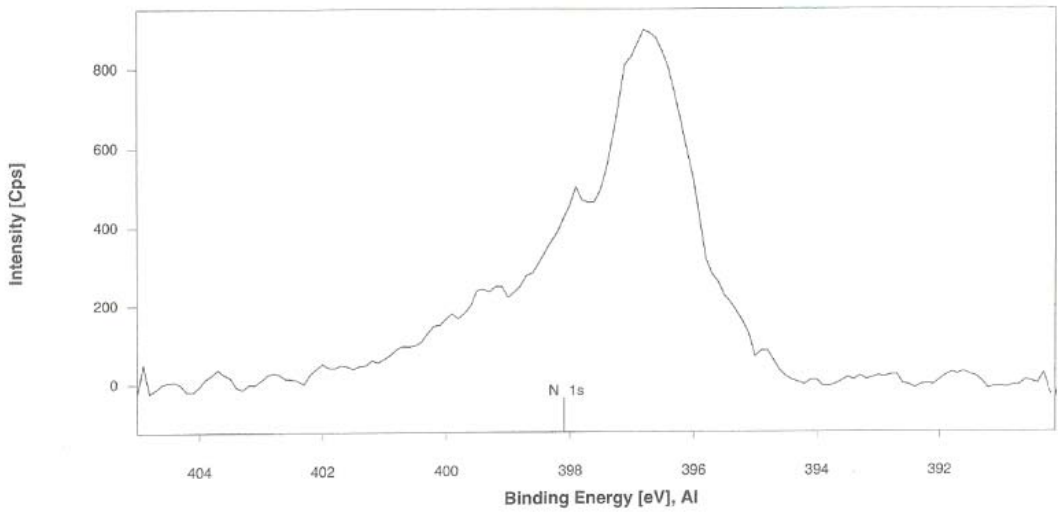


(b) After Sputter

Figure 5.18. XPS data regarding the nitrogen peaks before and after sputter

low thickness of the coatings; same sputtering process and period was able to reach deeper sections for Run 1 than it did for Run 2. Carbon content decreases were noted as 2.8% for coatings on silicon wafer substrate, and 0.7% on glass substrate in the XPS analysis of the second run samples.

The presence of a relatively high concentration of oxygen on the carbon layer surface may be explained by surface contaminations and bonding of oxygen in post reactions with carbon free radicals formed during plasma deposition [141].

Table 5.5. Elemental composition of the DLC on glass substrate (Run 1)

| Before Sputter | | | After Sputter | | |
|---|---|---|---|---|---|
| Element | Atom % | Orbit | Element | Atom % | Orbit |
| C | 63.1 | 1s | C | 59.7 | 1s |
| O | 15.8 | 1s | O | 7.8 | 1s |
| N | 10.0 | 2p | N | 16.2 | 2p |
| Ti | 3.4 | 1s | Ti | 13.1 | 1s |
| Nb | 1.5 | 2p | Nb | 1.3 | 2p |
| Si | 6.1 | 3d | Si | 1.9 | 3d |

Table 5.6. Elemental composition of DLC on silicon wafer substrate (Run 2)

| Before Sputter | | | After Sputter | | |
|---|---|---|---|---|---|
| Element | Atom % | Orbit | Element | Atom % | Orbit |
| C | 60.6 | 1s | C | 57.8 | 1s |
| O | 15.7 | 1s | O | 8.5 | 1s |
| N | 15.2 | 2p | N | 17.8 | 2p |
| Ti | 5.7 | 1s | Ti | 12.9 | 1s |
| Nb | 2.8 | 2p | Nb | 2.9 | 2p |
| Si | 0.0 | 3d | Si | 0.0 | 3d |

Table 5.7. Elemental composition of the DLC on glass substrate (Run 2)

| Before Sputter | | | After Sputter | | |
|---|---|---|---|---|---|
| Element | Atom % | Orbit | Element | Atom % | Orbit |
| C | 62.7 | 1s | C | 62.0 | 1s |
| O | 17.1 | 1s | O | 11.7 | 1s |
| N | 13.6 | 2p | N | 15.9 | 2p |
| Ti | 5.2 | 1s | Ti | 8.8 | 1s |
| Nb | 1.3 | 2p | Nb | 1.5 | 2p |
| Si | 0.0 | 3d | Si | 0.0 | 3d |

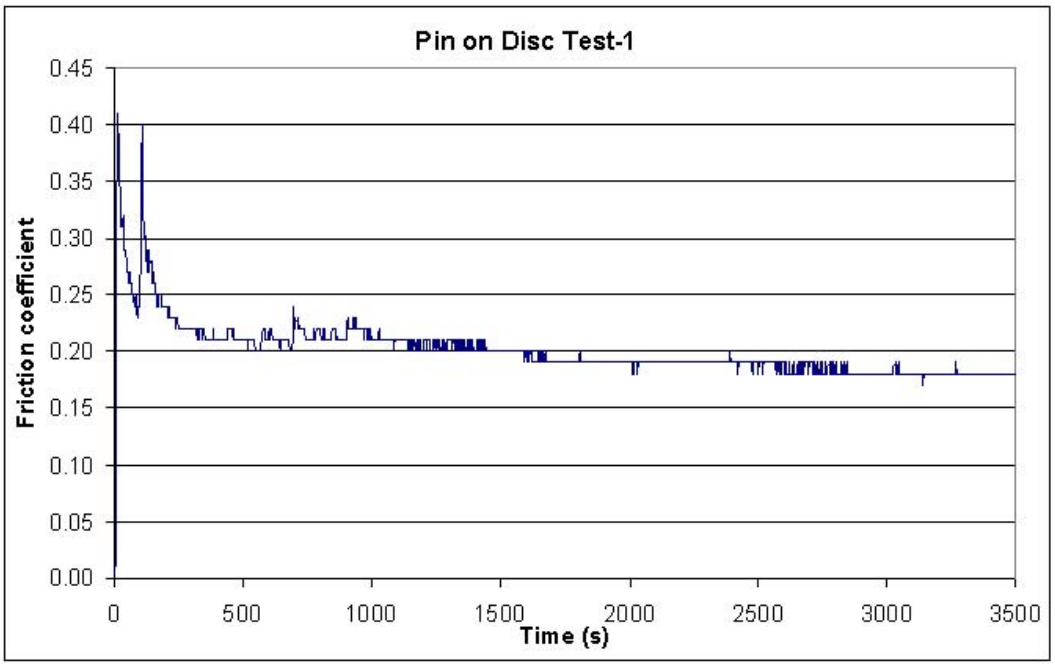


Figure 5.19. Pin on disc test results

## 5.3. Tribological Characterization results

Tribological studies were conducted in the manner explained in the experimental methods chapter, section 4.3, to determine coefficient of friction and scratch adhesion values. Below are the results of the tests, which were both carried out in Atatürk University Labs.

### 5.3.1. Pin on Disc Test Results

Pin-on-disk wear tests were conducted with Teer Corp. POD-2 pin on disc testing equipment. Testing procedure was explained in section 4.3.1 and the operation specifications pertaining this procedure is given in Table 5.8. Resulting time-friction coefficient graph is added in Figure 5.19.

It is noted that the friction coefficients of the coatings ($\mu$) were initially at $\mu$=0.2 level increasing up to $\mu$=0.4 in the first 1-15 seconds. After the smoothening of the wear track and breaking of the adhesive bonds that are evident in the asperities, friction coefficients had a tendency to decrease. However following this period, there was again

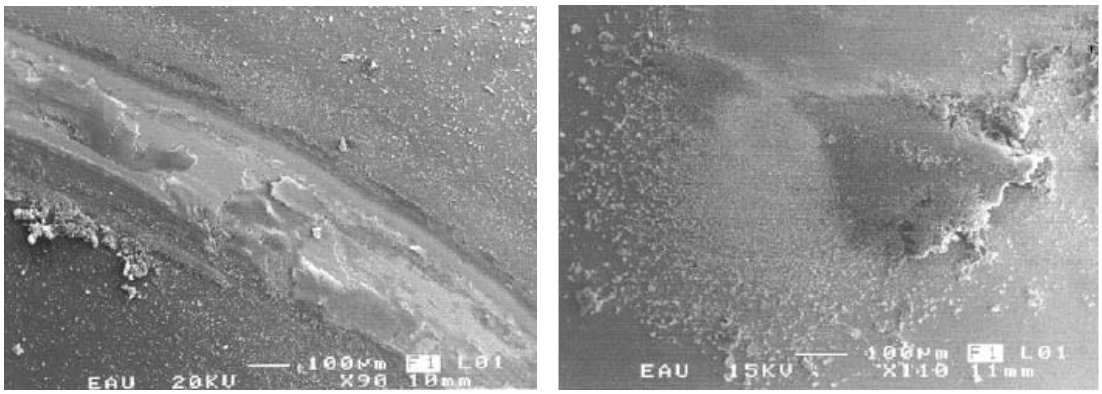


(a) Wear track (b) Pin

Figure 5.20. SEM images of the wear surfaces

a sudden increase in the COF values, presumably due to the formation of wear particles as a result of the abrasive deformation in the system. With the formation of a transfer layer, whose effect is mentioned extensively in the introduction chapter, the coefficients of friction achieved a decreasing but stable trend again. Transfer layer both on the wear track of the coating and the pin surface are depicted respectively in (Figure 5.20a) and (Figure 5.20b). Friction coefficient was observed to settle at $\mu$=0.18 around t=2500s.

Wear particles were investigated with SEM and found to have diameters around 0.5-1 $\mu$m (see Figure 5.21). Size distribution was homogenous, whereas the particles were observed to pile up mainly along the edges of the wear track, as seen in Figure 5.22.

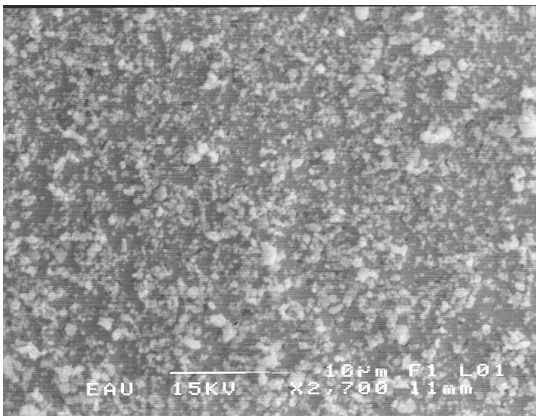


Figure 5.21. Wear particles formed as a result of the abrasive deformation

In the literature, it was stated before that, $Ti$ concentration plays a very important role in the friction coefficients of the $Ti$-$aC$ coatings. When the concentration of $Ti$ was increased, higher friction coefficients and high wear rates were observed [82].

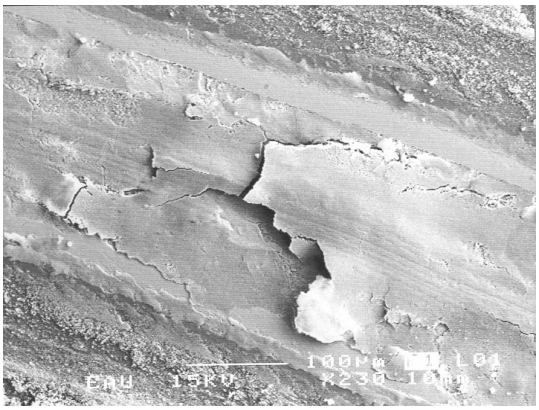

Figure 5.22. SEM image of the transfer layer formed on the track

The friction coefficient attained in this study, still low but not superlow, could be attributed to the high *Ti* content present in both runs (around 13 at.%). It is known that the steady-state friction coefficients range between 0.05-0.25 in ambient humid air for DLC coatings (not doped, against zirconia pins) [48], 0.2 for *Nb-DLC* coatings and 0.25 for *Ti-DLC* coatings [83] (against sapphire pins). Value 0.18, attained in this study against *WC-6%Co* balls, point to a lower coefficient of friction than the expected values.

Another point to note is that the coatings deposited in this study had hydrogen in the composition, which enabled them to operate better in vacuum and non-humid conditions. With further tribotests conducted in ultra high vacuum or under gas atmospheres (such as under $N_2$ atmospheres, where Erdemir et al. reached astonishingly low coefficients of friction with pure DLC films [59]), it is for sure that much lower friction coefficients could be attained.

Next, wear rate calculations were carried out. For a sample study, wear length was calculated as 141.4 meters, with the parameters given in Table 5.8. All equations, pertaining to these calculations were supplied in Section 4.3.1. To calculate the wear volume, initially the wear area is required. For this purpose, wear track crossection derived with the surface profilometer is used.

Figure 5.23 and Figure 5.24 show sample profiles used to measure the wear area. For the samples in Figure 5.24, the left profile gave an area of 88 $\mu m^2$ and on the

Table 5.8. Pin on Disc test procedure specifications

| Parameters | Conditions |
|---|---|
| Load applied (N) | 10 |
| Velocity of the pin (mm/s) | 79 |
| Wear track diameter (mm) | 10 |
| Environment | Humid air |
| Humidity (%RH) | 45-55 |
| Ambient temperature (°C) | 22 |
| Test duration (s) | 3600 |
| WC-6%Co ball diameter (mm) | 5 |

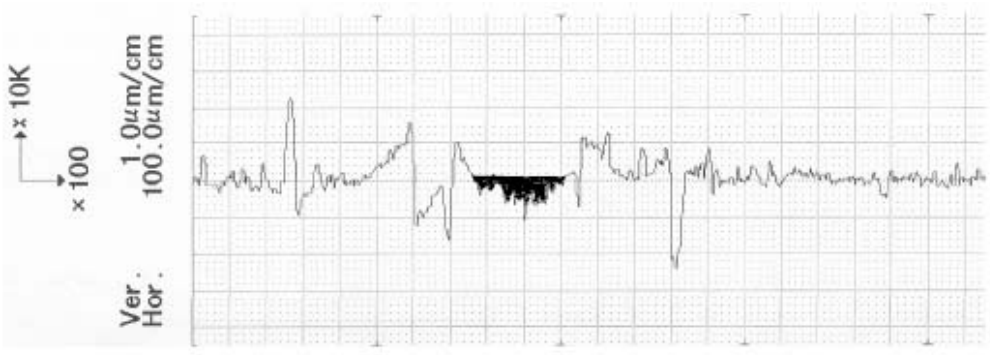


Figure 5.23. Run 1 wear area calculation samples

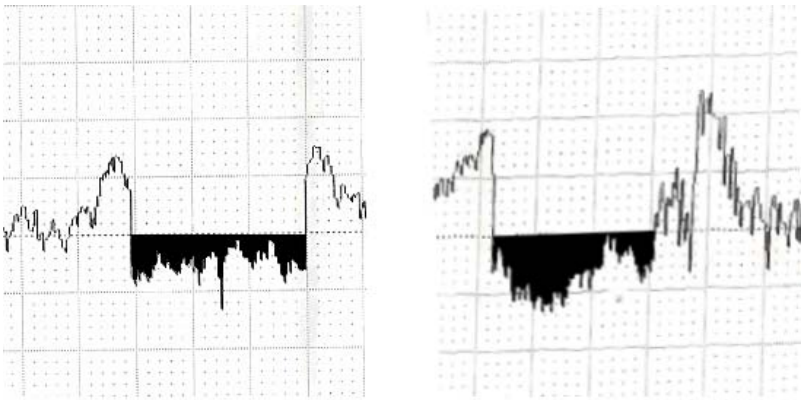

Figure 5.24. Run 2 wear area calculation samples with close-up at wear grooves

right, 74 $\mu m^2$. Wear volume calculations were then done, leading to wear rates. These rates were found to be between $4,9 \times 10^{-5} mm^3 (N.m)^{-1}$ and $5,2 \times 10^{-5} mm^3 (N.m)^{-1}$ for Run 1. Same parameters were found to be $1,955 \times 10^{-6} mm^3 (N.m)^{-1}$ and $1,644 \times$

$10^{-6}mm^3(N.m)^{-1}$ for Run 2.

In the literature, it was stated that a lower wear rate was observed when the Ti concentration is lower than 4 at. %. A strong increasing trend appears when the Ti concentration exceeds 4 at.% [82]. This titanium related wear behavior needs further experiment to be conducted with lower Ti percentages.

The wear rates supplied in the literature for W-DLC coatings are as low as $1 \times 10^{-15}m^3(N.m)^{-1}$ up to $8 \times 10^{-15}m^3(N.m)^{-1}$ against sapphire balls [83]. The same study of Bewilouga et al. indicated wear rates between $2,5 \times 10^{-15}m^3(N.m)^{-1}$ and $6,5 \times 10^{-15}m^3(N.m)^{-1}$ for Ti/C-DLC films and $2,1 \times 10^{-15}m^3(N.m)^{-1}$ and $3,6 \times 10^{-15}m^3(N.m)^{-1}$ for Nb/C-DLC coatings. Results reached in the second run of this study are as $1,955 \times 10^{-15}m^3(N.m)^{-1}$ and $1,644 \times 10^{-15}m^3(N.m)^{-1}$ when converted to $10^{-15}$ scale, which indicate wonderful wear resistance. This result was quite predictable by the high H/E ratios reached in nanoindentation studies. Wear rate of metal free DLC is indicated in the study of Bewilouga et al. to be around $1 \times 10^{-15}m^3(N.m)^{-1}$ [83]; on the other hand the difference between the metal free DLC and (Ti,Nb)-DLC is not enormous, and the benefits such as higher hardness, critical load, etc. lead us to employ Me-DLC instead. For hydrogenated and non hydrogenated coatings, wear rates below ($10^{-6}mm^3(N.m)^{-1}$) are considered as extremely low [49], thus the coatings deposited in this study are considered as exhibiting very low wear rates. Still, there are coatings with wear rates as low as $10^{-8}m^3(N.m)^{-1}$, which are actually ultra hard coatings with hardness values up to 4000HV [142] but they exhibit extremely poor values of adhesion (as low as 15 N) [143].

It is apparent that a significant improvement in wear resistance is obtained when the coating thickness is increased from 1.5 $\mu$m to 2.5 $\mu$m. It was stated in the literature that in erosive or abrasive contacts, a greater overall coating thickness is often needed, especially for coarse and hard third bodies [118].

In a study conducted by Jafee et al. in 1999, the combined effect of surface roughness and coating thickness on adhesion values and wear rates were thoroughly studied

[144]. Researchers divided the resulting behavior into 3 different zones according to roughness values. Coatings deposited fall into region 2, where there is a significant effect of both parameters, described as, "friction varies with both surface roughness and coating thickness within this region. Friction increases with surface roughness and decreases with coating thickness." [144]. Results reached are thus consistent with the literature.

### 5.3.2. Scratch Testing Results

Scratch testing procedure was carried out with the specifications given in Section 4.3.2. Resulting critical load values were measured as 68 N for the first run and 73.5 N for the second. The graphs pertaining to these measurements are added in Figure 5.25.

It is noted that the critical load ($L_c$) value experienced a significant increase in the second run. When the reason of this increase is investigated, same parameters that increased the wear resistance was noted to have a beneficial effect in adhesion strength too. The authors of various studies, such as Valli in 1986 and Steinmann et al. in 1987, found that $L_c$ value decreased with increasing the roughness [103, 104, 105]. When the surface roughness values of Run 1 ($R_a$=0.09$\mu$m) and Run 2 ($R_a$=0.04$\mu$m) are compared, it is expected that an improved $L_c$ would be reached in the second run.

Then the effect of coating thickness was investigated. In the study of Villiger et al. in 1999, it was stated that the coating thickness was the most important coating property which affected the critical loads during the adhesion scratch tests. Higher critical loads for the onset of coating spallation was observed for thicker coatings [145]. Thus, the increase of the coating thickness had a positive effect on the adhesion strength of the coating, as well as the reduced surface roughness.

Another aspect of the beneficial effect of increased thickness on adhesion strength was seen in the case of a hard coating on a softer substrate. The applied loads often exceed the yield strength of the substrate, resulting in plastic deformation and con-

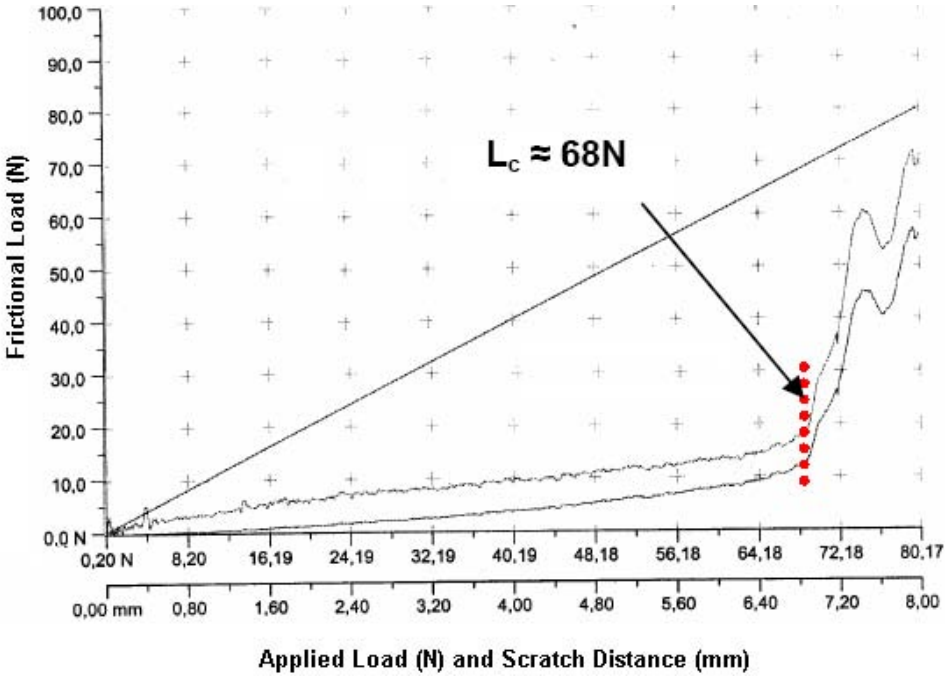


(a) Run 1

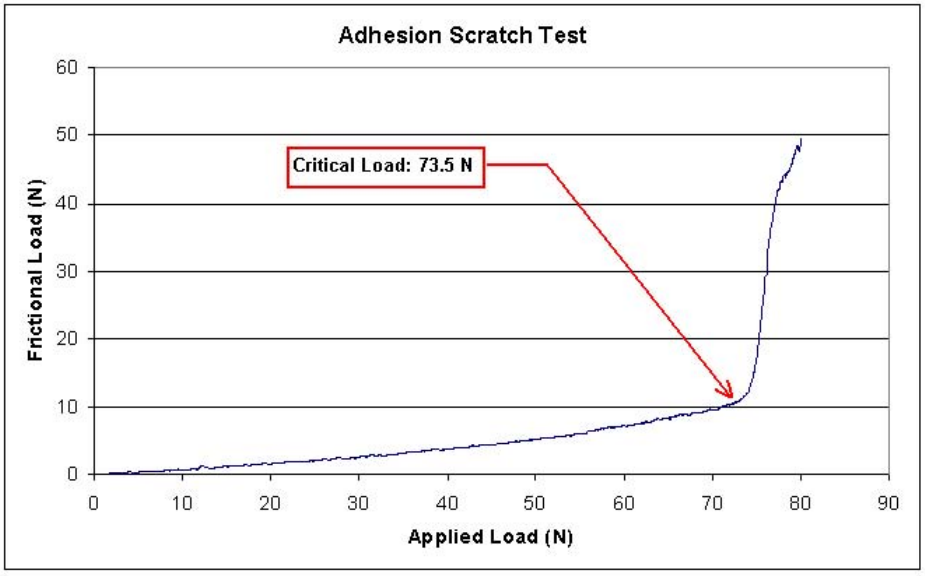


(b) Run 2

Figure 5.25. Adhesion scratch test graphics results

sequently debonding of the coating. Under these circumstances, increasing coating thickness results in higher critical loads for the onset of coating failure due to a "stress shielding" effect, provided that the residual stresses are significantly lower than the applied loads [145].

There is a wide scatter in the critical load values published in the literature for pure DLC films, from 18 N [146] to 48 N [57] and Yang et al. have considered critical loads greater than 50 N as "very good adhesion" [142] in their article. For doped films, DLC with *CrN* dopant gave 22 N - 45 N [72], *Cr-C:H*, 39 N and *Ti-C:H*, 46 N of critical load values. There has been improvement in graded coatings such as *Cr-C:H/CrN* had 57.8 N, *Ti-C:H/TiN* had 55 N and *Zr-C:H/ZrN* had 53.5 N critical load values [82]. Thus, considering the critical load levels reached in the study (up to 73 N), resulting coatings present far more better scratch resistance than the current coatings and also better substrate adhesion. Only coatings superior to the ones developed in this study are Graphit-iC and Dymon-iC coatings, both possessing 98 N of critical load and patented to Teer coatings.

## 5.4. Hardness Measurement Results

Hardness test in this study were conducted not to only reach the hardness values itself, but also it was desired to extract as much as information regarding the coating nature and behavior against plastic deformation. Below are the results of the tests carried out in Boğaziçi University and İTU.

### 5.4.1. Microhardness Results

Tests were conducted under 25, 50, 100, 200, 300, 500 and 1000 gf loads with Shimadzu microhardness test equipment. In Figure 5.26, an optical microscope snapshot of microindents formed with different loads are shown together.

Although the substrate material is fairly hard in this work (750 HV), subject coating is much harder and the hardness evolution is like Case II explained in 4.4.1 on page 47. This effect of decreasing hardness is noted clearly in the load-hardness graphic shown in Figure 5.27. However, reason of this decrease is not solely due to the substrate interference. It is well known that when measured at micrometer scale, hardness shows an indentation size effect (ISE), which is observed by the increase in the measured hardness with decreasing applied indentation load. Reason for this effect

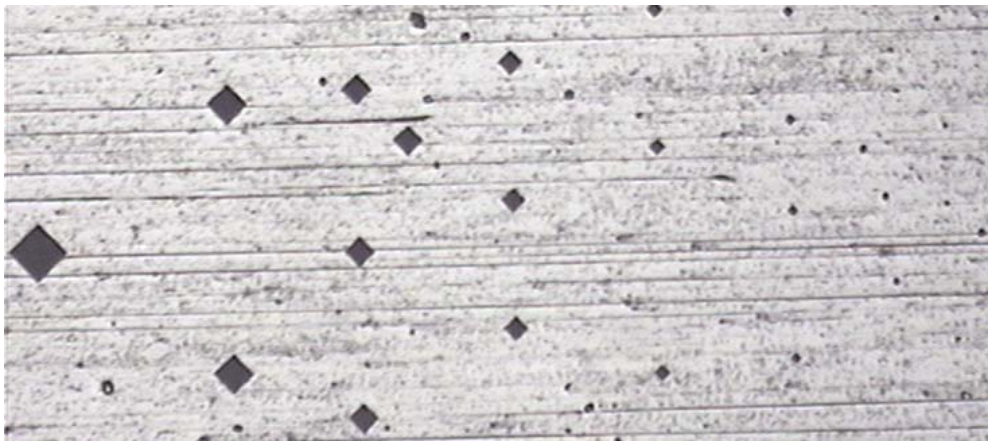

Figure 5.26. Image of microindents under various loads, magnification 10x

would be due to many causes, such as a highly elastic material giving a very small residual impression as a result of the load applied, leading the observer to conclude in a higher hardness value than the actual case [12].

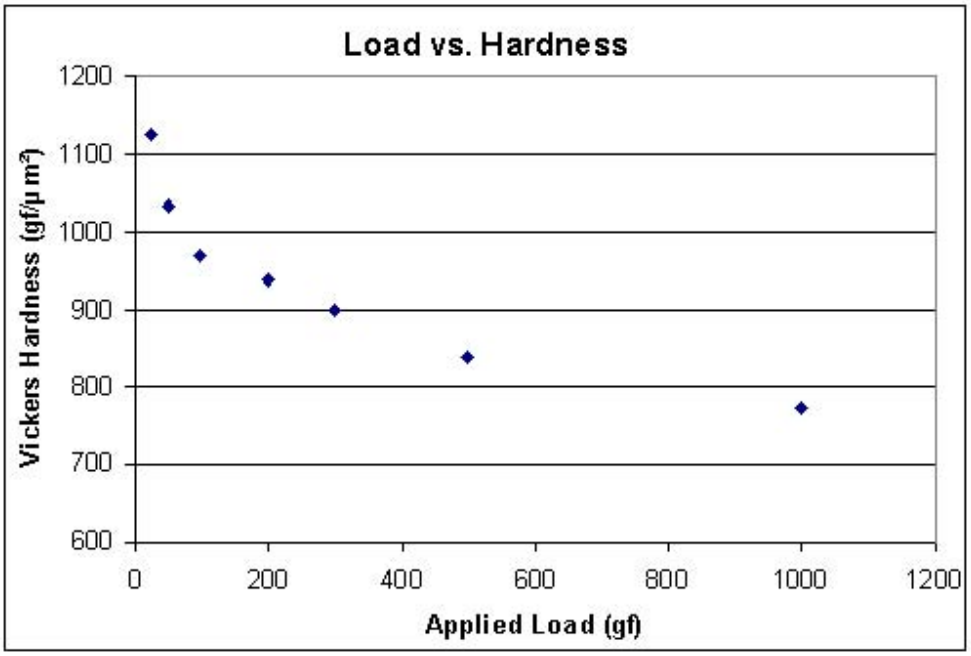


Figure 5.27. Hardness evolution with respect to the applied load for Run 1

When indentation depths in this experiment were analyzed, it was found that the shallowest indent depth was recorded as 0.614 $\mu$m under the application of 25 gf. When coating thickness, being around 1.5-2.5 $\mu$m is considered, this indentation depth is clearly deeper than the allowed measure. Due to this fact, it was concluded that

microhardness measurements would not yield a valid hardness measure for the coatings. Nevertheless, the highest hardness values regarding the coatings was recorded as 1124 HV for Run 1 and as 1206 HV for Run 2 under 25 gf load. For a healthier measurement of hardness, next nanohardness measurement procedures were employed.

### 5.4.2. Nanohardness Results

Results of the measurements are shown in tables 5.9 and 5.10. The symbols used in tables, whose graphical representation was supplied in Section 4.4.2, denote the following values:

HV: Vickers Hardness
$H_{IT}$: Indentation Hardness
$E_{IT}$: Indentation Elastic Modulus
$P_m$: Maximum applied force
$h_{max}$: Maximum indentation depth
$S$: Contact Stiffness
$h_c$: Indentation contact depth
$h_r$: Residual depth
$h_p$: Plastic depth
$A_p$: Projected contact area of the indent [10, 6, 147]

Table 5.9. Results of the nanohardness test for Run 1

| | Hardness (HV) | $H_{IT}$ (Mpa) | $E_{IT}$ (Gpa) |
|---|---|---|---|
| Indent 1 | 1025.00 | 10865.00 | 123.64 |
| Indent 2 | 910.35 | 9644.90 | 118.38 |
| Indent 3 | 896.00 | 9500.80 | 141.15 |
| Average | 943.78 | 10003.57 | 127.72 |
| Std. dev. | 70.70 | 749.49 | 11.92 |

Table 5.10. Results of the nanohardness test for Run 1

| | Indent 1 | Indent 2 | Indent 3 |
|---|---|---|---|
| $P_m$ (mN) | 4.02 | 4.02 | 4.01 |
| $h_{max}$ (nm) | 151.99 | 158.91 | 154.16 |
| $S(mN/nm)$ | 0.0843 | 0.0861 | 0.1014 |
| $h_c$ (nm) | 116.93 | 124.48 | 125.36 |
| $h_r$ (nm) | 104.37 | 112.25 | 114.59 |
| $h_p$ (mN/nm) | 71.44 | 76.60 | 76.86 |
| $A_p$ ($nm^2$) | 369690.81 | 416621.78 | 422233.63 |

Table 5.11. Results of the nanohardness test for Run 2

| | Hardness (HV) | $H_{IT}$ (Mpa) | $E_{IT}$ (Gpa) |
|---|---|---|---|
| Indent a | 1090.3 | 11773 | 142.84 |
| Indent b | 926.62 | 10006 | 141.28 |
| Indent c | 1045.8 | 11292 | 128.04 |
| Indent d | 926.27 | 10002 | 130.22 |
| Indent e | 846.1 | 9136 | 112.37 |
| Average | 967.02 | 10441.80 | 130.95 |
| Std. dev. | 99.14 | 1070.44 | 12.27 |

From formula (4.11), calculations revealed that the Me(Ti,Nb)-DLC films of Run 1 with 1.5 $\mu$m of thickness had an average indentation hardness $H_{IT}$ value of around 10 Gpa and Run 2 with 2.5 $\mu$m of thickness had an average indentation hardness $H_{IT}$ value of 10.44 Gpa. Maximum indentation hardness of the runs were recorded as 10.86 and 11.77 GPa for Run 1 and Run 2 correspondingly. Also by applying formulae (4.12) and (4.13), it was found that coatings of Run 1 had an average indentation elastic modulus $E_{IT}$ value of 127.72 Gpa and Run 2, 130.95 Gpa, maximum of these values measured as, 141.15 and 142.84 GPa. Scatter in these values (i.e. standard deviation) are correlated to the surface roughness of the samples, like stated by (Fischer-Cripps et al., 2006) [120].

Table 5.12. Results of the nanohardness test for Run 2

| | Indent a | Indent b | Indent c | Indent d | Indent e |
|---|---|---|---|---|---|
| $P_m$ (mN) | 4.02 | 6.01 | 4.02 | 4.02 | 8.02 |
| $h_{max}$ (nm) | 128.27 | 169.05 | 132.61 | 137.54 | 213.02 |
| $S(mN/nm)$ | 0.0942 | 0.1237 | 0.0872 | 0.0941 | 0.1219 |
| $h_c$ (nm) | 96.29 | 133.16 | 98.57 | 105.77 | 164.42 |
| $h_r$ (nm) | 85.55 | 120.43 | 86.55 | 94.84 | 147.21 |
| $h_p$ (mN/nm) | 60.76 | 85.95 | 51.14 | 67.5 | 103.02 |
| $A_p$ ($nm^2$) | 341759.78 | 601015.88 | 355759.47 | 401609.63 | 877794.13 |

It is noted in the literature [106] that, $R_a$ value should be less than 5% of the maximum penetration depth as stipulated in the International Standard ISO 14577-4. When the surface roughness of the coated samples are considered, for Run 1, attaining an indentation depth of 1.8 $\mu$m is required to realize surface roughness condition. This depth increases to 2.2 $\mu$m for coatings of Run 2. Obviously attaining these depths is not possible due to the 10% rule, which states that the indentation depth / coating thickness ratio must be lower than 10% to prevent substrate interference [125]. Decision was made towards violating surface roughness condition instead of 10% rule and thus scatter was observed.

Ratio of the indentation hardness to elastic modulus, often called as “plasticity index”, “plastic resistance parameter” or “elastic strain to failure” is an important indicator of coating behavior. Although for a long time hardness has been regarded as the primary material property, the elastic strain to failure, which is related to the H/E ratio, is a more suitable parameter for predicting wear resistance [148], where higher the ratio H/E, better the wear resistance is [149]. These ratios for the current study are supplied in tables 5.13 and 5.14.

Table 5.13. Plastic resistance parameters of Me(Ti,Nb)-DLC coatings, Run 1

| | $H_{IT}$ / $E_{IT}$ |
|---|---|
| Indent 1 | 0,09 |
| Indent 2 | 0,08 |
| Indent 3 | 0,07 |

Table 5.14. Plastic resistance parameters of Me(Ti,Nb)-DLC coatings, Run 2

| | $H_{IT}$ / $E_{IT}$ |
|---|---|
| Indent a | 0.08 |
| Indent b | 0.07 |
| Indent c | 0.09 |
| Indent d | 0.08 |
| Indent e | 0.08 |

When H/E ratios published in the literature are examined [150, 151, 120, 148], it was found that the values attained in this work were close to their results. Values reached in the prior experiments were regarded as promising and the same applies for the coatings of this study. In these studies, diamond was noted to have a H/E ratio of 0.1, amorphus carbon coatings 0.08, and *nc-TiC/a-C:H* 0.087. Thus, our H/E ratio average at 0.08 is said to indicate a good wear resistance.

In the study of Beake et. al. in 2006, it is stated that H/E value also influences the nanoscratch behavior. Coatings with higher H/E showed higher critical loads for elastic–plastic transition and also higher critical loads for the total coating failure occurring in front of the probe [152]. However, this shouldn't be misinterpreted as higher the H/E ratio, better the coating tribology. It is also noted by the researchers that, coatings with higher H/E exhibited an unloading failure, occurring behind the probe at much lower load than the loading failure. Thus, optimizing this stress-related unloading failure cases is far more important for tribological applications [152].

It is also possible to reach the elastic-plastic deformation percentages. The ratio of plastic depth to maximum depth will give the plastic deformation amount, which would prove useful in the characterization of the coating deformation processes by means of ductility. These ratios are given in tables 5.15 and 5.16

Table 5.15. Plastic deformation of Me(Ti,Nb)-DLC coatings, Run 1

| | % Plastic deformation |
|---|---|
| Indent 1 | 47 |
| Indent 2 | 48 |
| Indent 3 | 50 |

Table 5.16. Plastic deformation of Me(Ti,Nb)-DLC coatings, Run 2

| | % Plastic deformation |
|---|---|
| Indent a | 47 |
| Indent b | 51 |
| Indent c | 39 |
| Indent d | 49 |
| Indent e | 48 |

Plastic deformation percentages are calculated using the formula given below, where deformation % is denoting plastic deformation per cent.

$$deformation\% = \frac{h_p}{h_{max}} \tag{5.1}$$

It is seen from the results that the coatings undergo extensive elastic deformation, which goes as high as 61%. Still these coatings are not considered as ductile, which is illustrated in Figure 5.28, where load displacement curves of various solid are depicted

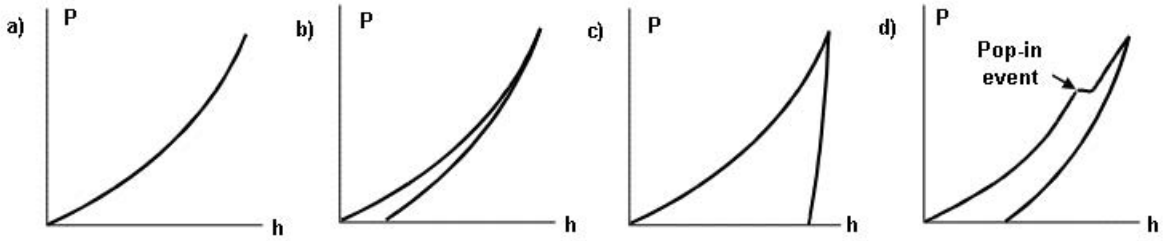


Figure 5.28. P-h curves for a-)elastic, b-)brittle, c-)ductile, d-)brittle solids [12]

[12]. Here, our coatings demonstrate the behavior in b, which is regarded as belonging to brittle solids.

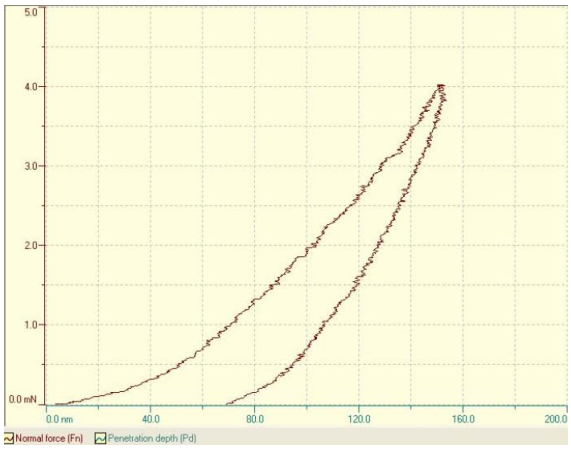


(a) Indent 1

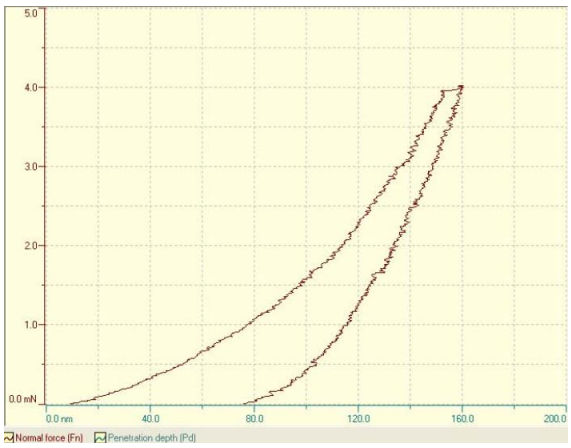


(b) Indent 2

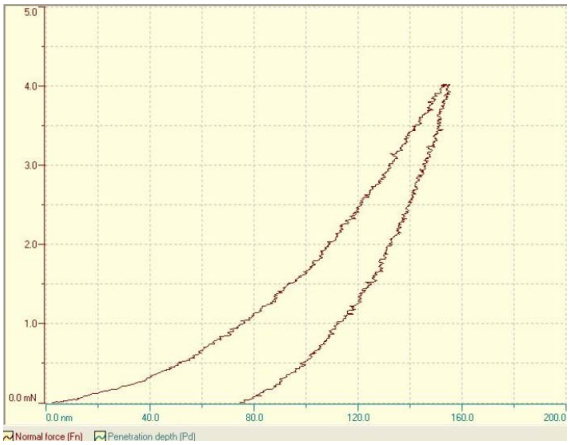


(c) Indent 3

Figure 5.29. Run 1 nanoindentation load-unload graphics

An important point to note in the nanohardness experiments is the ratio of the indentation depth to the thickness of the coating. In order to take healthy measurements, (i.e. free from the substrate effects), as mentioned in section 4.4.1, indentation depth shouldn't be more than the 10% of the total coating thickness [125].

In this work, for the coatings of Run 1 (thickness around 1.5 $\mu$m), the maximum indentation depth occurred around 159 nm and for Run 2 (thickness around 2.5 $\mu$m), the maximum indentation depth occurred around 213 nm. These depths are considered to be in the safe range, although a small overrun (9 nm) was experienced for Run 1.

Figures 5.29 and 5.30 are the load-unload graphics of different indentations, on which the maximum depths (nm) versus the applied forces (mN) are shown.

From load-unload curve shapes, well adhered nature of the coatings are evident. Especially for higher loads (6mN and 8mN), the curves are smooth and defect free, which is one of the main indicators for well adhered structures, as shown in figure 5.32

For lower loads however, especially in the graphs 5.31c and 5.31d, the phenomenon called "pop-in" was observed. This incident is observed as a stepwise line, where a sharp increase in indentation depth occurs at a fixed load and it is related to the generation of nested cracks [153] and also crack propagation [122] of a brittle solid (see Figure 5.28). This effect is observed for loads around 2.1-2.2 mN.

Since this causes an instability and harms the reliability of the coatings, it is tried to be prevented by increasing the bias voltage applied to the coatings [121]. There was no crack associated with the indents as far as we could observe, nevertheless an intense SEM or AFM study would be beneficial.

Lastly, it was proposed by Hainsworth et al. [123] that, by examining P-$\delta^2$ curves, it was possible to characterize the deformation mechanism of a coating [123]. In this study, researchers related the initial straight line segment of the P-$\delta^2$ curves to identify "coating only" behaviors [154].

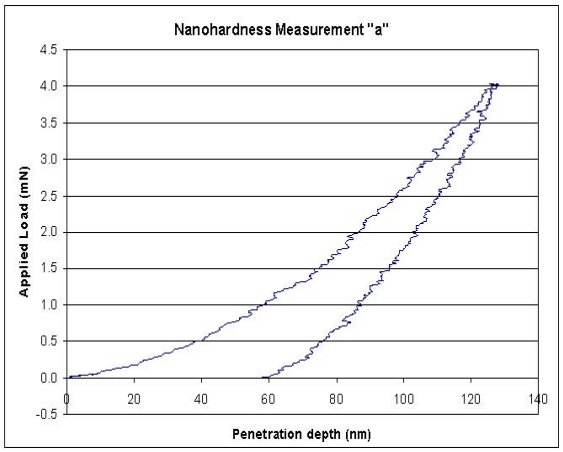


(a) Indent a

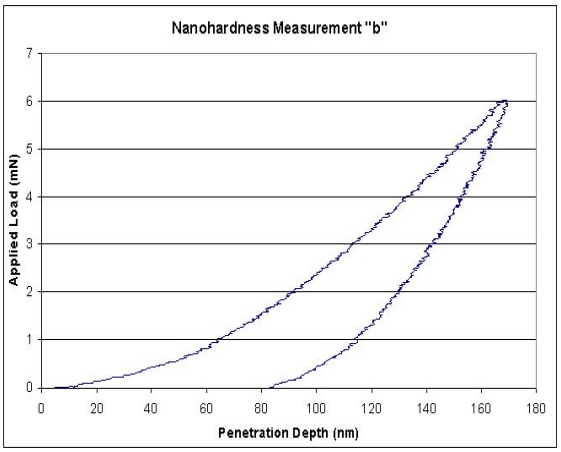


(b) Indent b

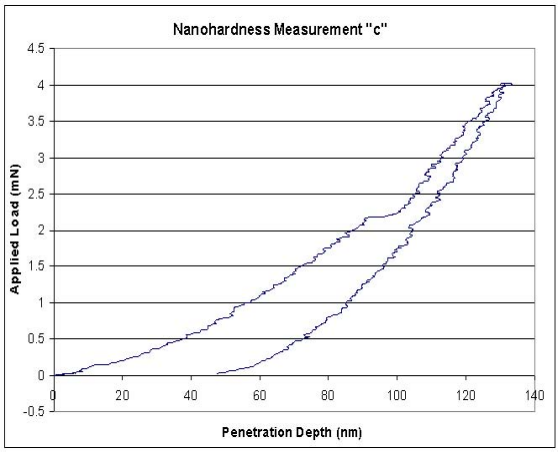


(c) Indent c

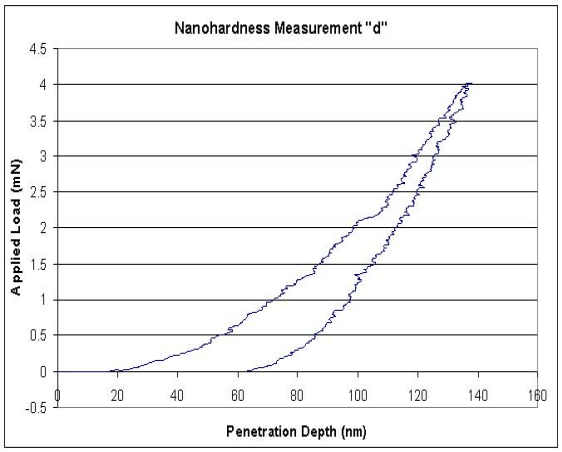


(d) Indent d

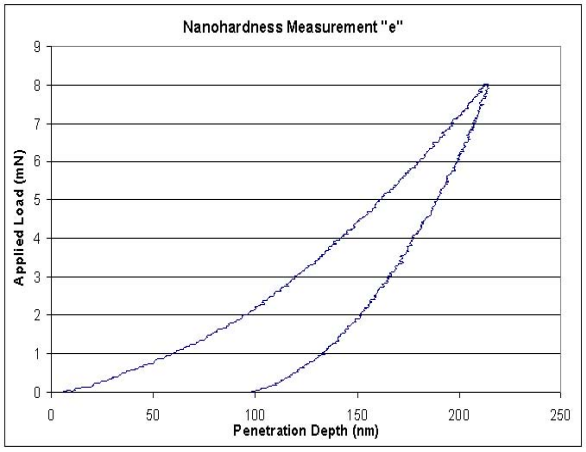


(e) Indent e

Figure 5.30. Run 2 nanoindentation load-unload graphics

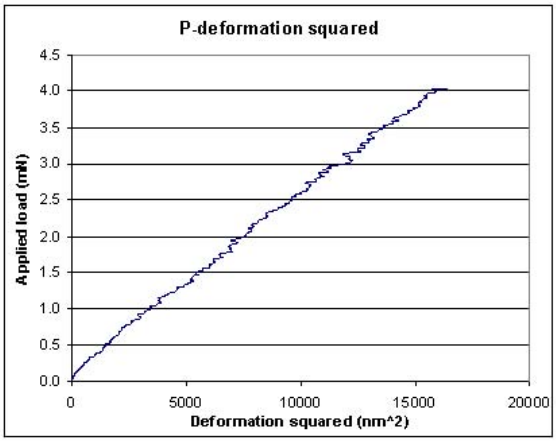


(a) Indent a

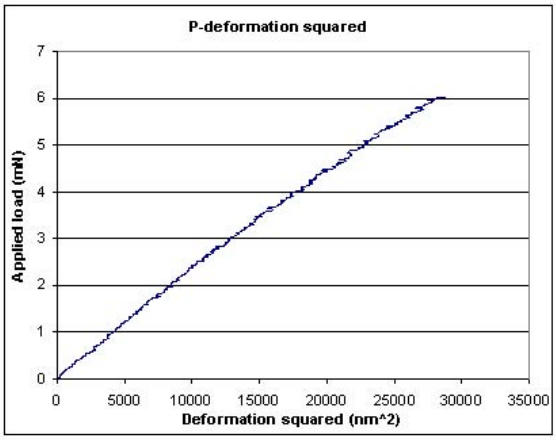


(b) Indent b

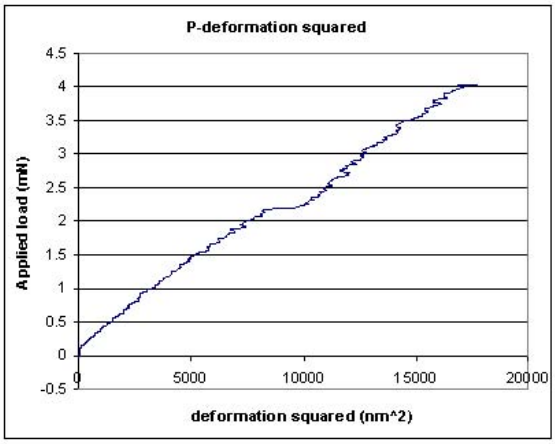


(c) Indent c

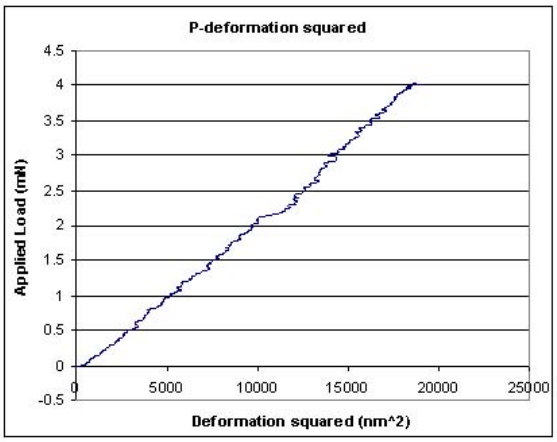


(d) Indent d

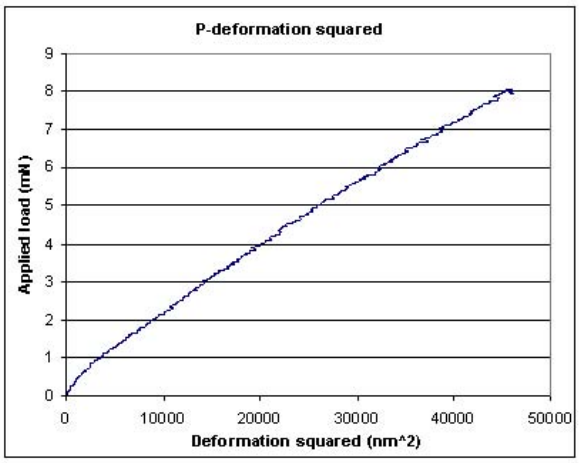


(e) Indent e

Figure 5.31. P-$\delta^2$ graphs of indents a to e for Run 2

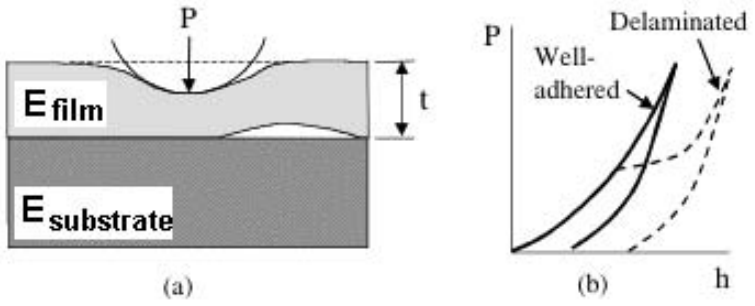


Figure 5.32. Observable features of mechanical failure on a P-h curve [12]

As expected by never violating the 10% indentation depth rule, the P-$\delta^2$ curves observed in this study are completely linear for all cases. Only blunder is the effect of pop-in events, which caused a shift from the linear line, but the slope of the line was not altered. Thus it is true to say that the measured values are "coating only" responses and they reflect the true hardness nature of the coatings.

# 6. CONCLUSION

In this study titanium and niobium doped diamond like carbon coatings were grown, using pulsed-dc closed field unbalanced magnetron sputtering method. Resulting coatings were characterized in four different aspects; structural, compositional, tribological characterization and hardness measurements.

As a result of the structural characterizations, it was found that the resulting coatings grew in a dense manner with columnar structures and domed tops. This type of growth corresponded to Zone I type of Thornton's model, however, voids were not observed in the structure much. Thicknesses of the coatings were measured as 1.5 $\mu$m for the first run and 2.5 $\mu$m for the second.

After the coating deposition, there was a clear increase in the surface roughness (from $R_a$=0.08 $\mu$m to 0.09 $\mu$m in the Run 1, from 0.04 $\mu$m to 0.11 $\mu$m for the Run 2). This was pointing to the fact that the increase in thickness had a significant effect on surface roughness evolution. An additional AFM roughness was also conducted, which yielded a $R_a$ value of 6.376 nm, almost one fifth of surface profilometer reading. Discrepancy is thought to be due to the instruments using the same quantity to express different parameters. Surface characteristics, determined with AFM, showed a kurtosis value of 0.380, indicating a good measure of flatness and a skewness value of -0.016, indicating the dominance of deep valleys over sharp peaks.

Compositional characterization consisted of XRD and XPS studies. XRD spectra presented various peaks regarding *TiC*, *NbC* and *TiC(Nb-N)* reflections. *TiC* had distinct features resident corresponding to $TiC(200)$, $TiC(111)$ and $TiC(220)$ phases. $TiC(220)$ peak presented a strong shift from the JCPDS reference due to doping agents (nitrogen and niobium) that got trapped in *TiC* crystals. Also for *NbC*, there were peaks $NbC(111)$ and $NbC(200)$. It was concluded that the overall structure of the coating was close to an amorphus structure.

XPS analysis showed that the DLC coatings developed in this study were composed of almost only graphitic character, carbon peak located at 284.4 eV. There was a significant effect of oxidation probably due to air exposure and oxidation. Elemental composition of the coatings supported this oxidation effect, since besides the dopants, there was a significant amount of oxygen in the composition.

Tribological characterization showed that the coefficients of friction was around 0.18 against $WC-6\%Co$ pins under 50% RH ambient air. Wear rates were measured around $4,9\times10^{-5}mm^3(N.m)^{-1}$ for Run 1 and around $1,644\times10^{-6}mm^3(N.m)^{-1}$ for Run 2. Wear rates especially in the second run could be classified as very low, indicating a good quality of DLC coatings. The improvement in Run 2 is attributed to the lowered surface roughness values and increased coating thickness. Same parameters causing the improvement in friction behavior, also benefits scratch resistance. Run 1 adhesion critical load was around 68 N, and Run 2, 73.5 N, which are far better than the results published in the literature. Adhesion scratch tests indicate excellent adhesion.

Lastly hardness measurements were done, where nanohardness tests gave healthier results. Maximum indentation hardness of the runs were recorded as 10.86 and 11.77 GPa for Run 1 and Run 2 correspondingly and maximum indentation elastic modulus $E_{IT}$ values were measured as, 141.15 and 142.84 GPa. Coatings exhibited good H/E ratios indicating high wear resistance. This was realized in the adhesion scratch tests. Also the elastic recovery percentages of the coatings were quite high, up to even 61 per cent. Lastly, the P-$\delta^2$ curves of the coatings presented perfect linear trends that support the validity of the test. Linear trend was stated in the literature to reflect coating only behavior.

# 7. FUTURE WORK

There are many parameters that govern a coating process and the effect of each parameter significantly alters the coatings yielded in the end. It was only possible to conduct two runs in this study, where more runs with altered parameters would widen the scope of the study.

Also after the deposition, proper assessment of the results is important. In further studies, technical consultancy of an XPS expert would prove useful to determine the exact phase compositions of the coatings and oxidation products. Also with this expertise, a depth profiling process could be carried out, leading to very valuable information about the coating microstructure evolution.

Lastly, since the coatings of this study have hydrogen in the composition, they operate better in vacuum conditions. Conduction of the tests under vacuum or under $N_2$ gas atmospheres should be carried out to determine the tribological behavior, where better cof values would be attained.

# REFERENCES


1. University, B., "EN 3: Introduction to Engineering and Statics: Friction", http://www.engin.brown.edu/courses/en3/Notes/Statics/friction/friction.htm, 2007.

2. Ströck, M., "Eight Allotropes of Carbon", Free License image: http://en.wikipedia.org/wiki/Image:Eight_Allotropes_of_Carbon.png, 2006.

3. Robertson, J., *Amorphous Carbon: State of the Art*, chap. Deposition mechanism of diamond-like carbon, pp. 32–45, World Scientific Publishing, Singapore, 1998.

4. Thornton, J., "High rate thick film growth", *Ann. Rev. Matter. Sci.*, Vol. 7, pp. 239–260, 1977.

5. Totik, Y., R. Sadeler, H. Altun and M. Gavgali, "The effects of induction hardening on wear properties of AISI 4140 steel in dry sliding conditions", *Materials & Design*, Vol. 24, pp. 25–30, 2003.

6. *Applications Bulletin: Overview of Mechanical Testing Standarts*, Tech. Rep. 18, CSM Instruments Advanced Mechanical Surface Testing, CSM Instruments Rue de la Gare 4 CH-2034 Peseux Switzerland, September 2002.

7. "Scratch Test: Nano, Micro & Macro Ranges", Websource: http://www.csm-instruments.com/new/contenus/e/doc/techniques/Scratch%20theory.pdf, 2007.

8. Philippe, K., "Introduction on depth instrumented indentation testing for hardness and elastic modulus determination", CSM Instruments Workshop on Mechanical Characterization of Coatings and Surfaces-Training and Presentations on Practical Applications, Ankara, Vaksis Ar-Ge ve Muhendislik Ltd. Sti., Ankara, September 28, 2006.

9. Chowdhury, S., M. Laguier, I. Rahman and M. Seratoni, "Nanoindentation combined with scanning force microscope for characterization of mechanical properties of carbon nitride thin films", *Surface and Coatings Technology*, Vol. 177-178, pp. 537–544, 2004.

10. "CSM Instruments: Indentation, Nano & Micro Ranges", http://www.csm-instruments.com/new/contenus/e/doc/techniques/Indentation%20theory.pdf, 2007.

11. Salvadori, M., D. Martins and M. Cattani, "DLC Coating Roughness as a Function of Film Thickness", *Surface and Coatings Technology*, Vol. 200, pp. 5119–5122, 2006.

12. Fischer-Cripps, A., *Nanoindentation*, Springer-Verlag, Secaucus, NJ, USA, Springer-Verlag New York, 2002.

13. Hogmark, S. and M. Olsson, "Wear mechanisms of HSS cutting tools", Websource: http://hssforum.com/Aachen/04_Hogmark.pdf, 15 February 2005, new Developments in High Speed Steel and Surface Engineering.

14. Böhler Edelstahl Gmbh & CO KG, Mariazeller Strasse 25 Postfach 96 A-8605 Kapfenberg/Austria, *Böhler S600 High Speed Steel Product Catalogue*, June 2002.

15. Cluett, J., *Cleanability of Certain Stainless Steel Surface Finishes in the Brewing Process*, Master's thesis, Rand Afrikaans University, Engineering Faculty, Mechanical Engineering Department, October 2001.

16. "Surface Profilometers Specifications on Globalspec search engine", http://process-equipment.globalspec.com/Specifications/Manufacturing_Process-_Equipment/Inspection_Tools_Instruments/Surface_Profilometers, 2007.

17. "Part 5: Ergebnisse der Untersuchungen der Schichteigenschaften", Websource: http://www.micro-controller.com/de/plasma_wissenswertes/part5.html, 2007.

18. Galvan, D., *Nanocomposite Coatings Processing, Structure and Tribological Performance*, Ph.D. thesis, Rijksuniversiteit Groningen, 2007.

19. Hosson, J. D., "Dutch Reserach Database: Surface and Interface Engineering", http://www.onderzoekinformatie.nl/en/oi/nod/onderzoek/OND1300702/, 2007.

20. Overney, R., "Introduction to Tribology: Friction (Updated version: 6/Feb/07)", http://depts.washington.edu/nanolab/ChemE554/Summaries%20ChemE%20554-/Introduction%20Tribology.htm, 2007.

21. Pauleau, Y., *Solid Lubricant Coatings Produced by Physical and Chemical Vapor Deposition Techniques*, Vol. 290 of *E: Applied Sciences*, pp. 475–527, Kluwer Academic Publishers, Chateau de Bonas, Gers, France, July 18-29 1994.

22. Bowden, F. and D. Tabor, *The friction and lubrication of solids*, Vol. I, Clarendon Press, Oxford, England, 1950.

23. Brendle, M. and G. Colin, *Friction and Traction*, chap. The frictional and transfer behaviour of compacted solid lubricants on smooth metallic surfaces, Butterworth, London, 1991.

24. Langlade, C., S. Fayeulle and R. Olier, "New insights into adhesion and lubrication properties of graphite-based transfer films", *Wear*, Vol. 172, pp. 85–92, 1994.

25. Holinski, R., *Industrial Lubrication and Tribology*, Vol. 53, No. 2, pp. 61–65, 2001.

26. He, Z., Z. Wang, W. Wang, A. Fan and Z. Xu, *Surface and Coatings Technology*, Vol. 201, No. 9-11, pp. 5705–5709, 2007.

27. Kroger, F. and H. Vink, *Solid State Phys.*, Vol. 3, p. 307, 1956.

28. O'Keefe, M. and J. Rigsbee, *Spectroscopic Analysis of Engineered Surfaces, Interfaces and Thin Layers*, Vol. 290 of *E: Applied Sciences*, pp. 151–183, Kluwer Academic Publishers, Chateau de Bonas, Gers, France, July 18-29 1994.

29. Arslan, E. and I. Efeoglu, "Effect of heat treatment on *TiN* films deposited by CFUBMS", *Materials Characterization*, Vol. 53, pp. 29–34, 2004.

30. Molarius, J., A. Korhonen, E. Harju and R. Lappalainen, "Comparison of cutting performance of ion-plated NbN, ZrN, TiN and (Ti, Al)N coatings", *Surface and Coatings Technology*, Vol. 33, pp. 117–132, 1987.

31. Mayrhofer, P., C. Mitterer and J. Musil, "Structure-property relationships in single and dual-phase nanocrystalline hard coatings", *Surface and Coatings Technology*, Vol. 174-175, p. 725731, 2003.

32. Barshilia, H., B. Deepthi, A. Prabhu and K. Rajam, "Superhard nanocomposite coatings of TiN/$Si_3N_4$ prepared by reactive direct current unbalanced magnetron sputtering", *Surface and Coatings Technology*, Vol. 201, pp. 329–337, 2006.

33. Gassner, G., P. Mayrhofer and J. Kiefer, "Structure-property relations in *Cr-C/a-C:H* coatings deposited by reactive magnetron sputtering", *Surface and Coatings Technology*, Vol. 2005, pp. 1147–1150, 200.

34. Voevodin, A., J. O'Neill and J. Zabinski, *Thin Solid Films*, Vol. 342, pp. 194–200, 1999.

35. Munro, R., "Material Properties of Titanium Diboride", *Journal of Research of the National Institute of Standards and Technology*, Vol. 105, pp. 709–720, 2000.

36. Zergioti, I., C. Fotakis and G. Haidemenopoulos, "Growth of $TiB_2$ and $TiC$ coatings using pulsed laser deposition", *Thin Solid Films*, Vol. 303, pp. 39–46, 1997.

37. Shen, Y., Y. Lu and Z. Liu, "Microstructure evolution and grain growth of nanocomposite $TiN$-$TiB_2$ films: Experiment and Simulation", *Surface and Coatings Technology*, Vol. 200, pp. 6474–6478, 2006.

38. Babonneau, D., J. Toudert, S. Camelio, F. Pailloux, T. Cabioc'h and T. Gi-

rardeau, "Encapsulation of metallic nanoclusters in carbon and boron nitride thin films prepared by ion-beam sputtering", *Surface and Coatings Technology*, Vol. 200, pp. 6251–6257, 2006.

39. Chen, Y., Y. Chung and S. Li, "Boron Carbide and boron Carbonitride Thin Films as Protective Coatings in Ultra-High Density Hard Disk Drives", *Surface and Coatings Technology*, Vol. 200, No. 4072-4077, 2006.

40. Fenker, M., M. Balzer, R. Büchi, H. Jehn, H. Kappl and J. Lee, *Surface and Coatings Technology*, Vol. 163-164, pp. 169–175, 2003.

41. Barzilai, S., M. Weiss, N. Frage and A. Raveh, *Surface and Coatings Technology*, Vol. 197, pp. 208–214, 2005.

42. Oliveira, C., R. Munoz Riofano and L. Casteletti, "Micro abrasive wear test of niobium carbide layers produced on AISI H13 and M2 steels", *Surface and Coatings Technology*, Vol. 200, pp. 5140–5144, 2006.

43. Callister, J., *Materials Science and Engineering: an Introduction*, John Wiley and Sons, United states of America, 5th edn., 1999.

44. Goldsmith, J., E. Sutter, J. Moore, B. Mishra and M. Crowder, "Microstructure of amorphous diamond-like carbon thin films and changes during wear", *Surface and Coatings Technology*, Vol. 200, pp. 2386–2390, 2005.

45. Erdemir, A. and C. Donnet, *Handbook of Modern Tribology*, chap. Tribology of diamond, diamond-like carbon, and related films, p. 871, CRC Press, 2001.

46. Grill, A., "Tribology of diamond–like carbon and related materials: an updated review", *Surface and Coatings Technology*, Vol. 94-95, pp. 507–513, 1997.

47. Thorwarth, G., C. Hammerl, M. Kuhn, W. Assmann, B. Schey and B. Stritzker, *Surface and Coatings Technology*, Vol. 193, p. 206, 2005.

48. Donnet, C., J. Fontaine, A. Grill and T. Le Mogne, "The role of hydrogen on the friction mechanism of diamond-like carbon films", *Tribology Letters*, Vol. 9, No. 3-4, 2000.

49. Donnet, C. and A. Grill, "Friction control of diamond-like carbon coatings", *Surface and Coatings Technology*, Vol. 94-95, pp. 456–462, 1997.

50. Donnet, C., "Recent progress on the tribology of doped diamond-like and carbon alloy coatings: a review", *Surface and Coatings Technology*, Vol. 100-101, pp. 180–186, 1998.

51. Camino, D., A. Jones, D. Mercs and D. Teer, "High performance sputtered carbon coatings for wear resistant applications", *Vacuum*, Vol. 52, pp. 125–131, 1999.

52. Meneve, J., D. Havermans, K. Vercammen, H. Haefke, Y. Gerbig and E. Pflüger, "Mechanical Properties and Tribological Behaviour of State-of-the-Art Diamond-Like Carbon Coatings", *Advanced Engineering Materials*, Vol. 3, No. 3, pp. 163–166, 2001.

53. Murakawa, M. and S. Takeuchi, *Surface and Coatings Technology*, Vol. 163-164, p. 561, 2003.

54. Dasch, J., C. Ang, C. Wong, Y. Cheng, A. Weiner, L. Lev and E. Konca, "A comparison of five categories of carbon-based tool coatings for dry drilling of aluminum", *Surface and Coatings Technology*, Vol. 200, p. 2970 2977, 2006.

55. Dearnaley, G. and J. Arps, "Biomedical applications of diamond-like carbon (DLC) coatings: A review", *Surface and Coatings Technology*, Vol. 200, pp. 2518–2524, 2005.

56. Aisenberg, S. and R. Chabot, *Appl. Phys.*, Vol. 42, p. 2953, 1971.

57. Stallard, J., D. Mercs, M. Jarratt, D. Teer and P. Shipway, "A study of the tribological behaviour of three carbon-based coatings, tested in air, water and oil

environments at high loads", *Surface and Coatings Technology*, Vol. 177-178, pp. 545–551, 2004.

58. Podgornik, B., S. Jacobson and S. Hogmark, "Influence of EP and AW additives on the tribological behaviour of hard low friction coatings", *Surface and Coatings Technology*, Vol. 165, pp. 168–175, 2003.

59. Erdemir, A., G. Fenske, J. Terry and P. Wilbur, *Surface and Coatings Technology*, Vol. 94-95, pp. 525–530, 1997.

60. Ronkainen, H., S. Varjus and K. Holmberg, "Friction and wear properties in dry, water and oil-lubricated DLC against alumina and DLC against steel contacts", *Wear*, Vol. 222, pp. 120–128, 1998.

61. Shi, B., W. Meng, R. Evans and N. Hershkowitz, *Surface and Coatings Technology*, Vol. 200, pp. 1543 – 1548, 2005.

62. Vercammen, K., J. Meneve, E. Dekempeneer, E. Roberts and M. Eiden, "Study of RF PACVD diamond like carbon coatings deposited at low bias for vacuum applications", R. A. Harris (Editor), *ESA SP-480: 9th European Space Mechanisms and Tribology Symposium*, pp. 309–312, Sep. 2001.

63. Kennedy, F., D. Lidhagen, A. Erdemir, J. Woodford and T. Kato, "Communication: Tribological behavior of hard carbon coatings on steel substrates", *Wear*, Vol. 255, pp. 854–858, 2003.

64. Konca, E., Y. Cheng, A. Weiner, J. Dasch and A. Alpas, "Vacuum tribological behavior of the non-hydrogenated diamond-like carbon coatings against aluminum: Effect of running-in in ambient air", *Surface and Coatings Technology*, Vol. 259, pp. 795–799, 2005.

65. Konca, E., Y. Cheng, A. Weiner, J. Dasch and A. Alpas, "Elevated temperature tribological behavior of non-hydrogenated diamond-like carbon coatings against

319 aluminum alloy", *Surface and Coatings Technology*, Vol. 200, pp. 3996–4005, 2006.

66. Messina, G. and S. Santangelo, "Multi-wavelength Raman investigation of sputtered a-C film nanostructure", *Surface and Coatings Technology*, Vol. 200, pp. 5427–5434, 2006.

67. Ueng, H., C. Guo and K. Dittrich, "Development of a hybrid coating process for deposition of diamond-like carbon films on microdrills", *Surface and Coatings Technology*, Vol. 200, pp. 2900–2908, 2006.

68. Ha, P., D. McKenzie, M. Bilek, E. Doyle, D. McCulloch and P. Chu, "Control of stress and delamination in single and multi-layer carbon thin films prepared by cathodic arc and RF plasma deposition and implantation", *Surface and Coatings Technology*, Vol. 200, pp. 6405–6408, 2006.

69. Wang, D., Y. Chang, C. Chang and Y. Huang, "Deposition of diamond-like carbon films containing metal elements on biomedical Ti alloys", *Surface and Coatings Technology*, Vol. 200, pp. 2175–2180, 2005.

70. Chicot, D., P. Araujo, N. Horny, A. Tricoteaux and J. Lesage, "Application of the interfacial indentation test for adhesion toughness determination", *Surface and Coatings Technology*, Vol. 200, pp. 174–177, 2005.

71. Yu, J., S. Song and L. Weng, "Adhesion improvement of cubic boron nitride films by in situ annealing", *Surface and Coatings Technology*, Vol. 200, pp. 4737–4740, 2006.

72. Lattemann, M., K. Sell, J. Ye, P. Persson and S. Ulrich, "Stress reduction in nanocomposite coatings consisting of hexagonal and cubic boron nitride", *Surface and Coatings Technology*, Vol. 200, pp. 6459–6464, 2006.

73. Tither, G., "Progress in Niobium Markets and Technology", *Niobium-Science and*

*Technology, TMS*, , No. 1-16, 2001.

74. Fan, F., W. Tang, S. Liu, L. Hei, C. Li, G. Chen and F. Lu, "An effort to enhance adhesion of diamond coatings to cemented carbide substrates by introducing Si onto the interface", *Surface and Coatings Technology*, Vol. 200, p. 67276732, 2006.

75. Monaghan, D., D. Teer, P. Logan, I. Efeoglu and R. Arnell, *Surface and Coatings Technology*, Vol. 60, p. 525, 1993.

76. Güttler, J. and J. Reschke, *Surface and Coatings Technology*, Vol. 60, p. 531, 1993.

77. Wändstrand, O., M. Larsson and P. Hedequist, *Surface and Coatings Technology*, Vol. 111, p. 247, 1999.

78. Fryda, M., C. Benndorf, C. Klages and K. Taube, "Structural and Mechanical Properties of Nb Containing Amorphus Hydrogenated Carbon Films (Nb=C:H)", *Diamond and Related Materials*, Vol. 1, No. 5-6, pp. 558–562, 1992.

79. Freyman, C., Y. Chen and Y. Chung, "Synthesis of carbon films with ultra-low friction in dry and humid air", *Surface and Coatings Technology*, Vol. 201, pp. 164–167, 2006.

80. Xiang, Y., W. Cheng-biao, L. Yang, Y. De-yang and F. Zhi-qiang, *Surface and Coatings Technology*, Vol. 200, pp. 6765–6769, 2006.

81. Benchikh, N., F. Garrelie, C. Donnet, K. Wolski, R. Fillit, F. Rogemond, J. Subtil, J. Rouzaud and J. Laval, "Nanostructured coatings of metal containing diamond-like carbon films deposited by femtosecond pulsed laser ablation", *Surface and Coatings Technology*, Vol. 200, pp. 6272–6278, 2006.

82. Yang, B., Z. Huang, C. Liu, Z. Zeng, X. Fan and D. Fu, "Characterization and properties of Ti-containing amorphous carbon nanocomposite coatings prepared by middle frequency magnetron sputtering", *Surface and Coatings Technology*,

Vol. 200, pp. 5812–5818, 2006.

83. Bewilogua, K., C. Cooper, C. Specht, J. Schröder, R. Wittorf and M. Grischke, "Erratum to: Effect of target material on deposition and properties of metal-containing DLC Me-DLC/coatings", *Surface and Coatings Technology*, Vol. 132, pp. 275–283, 2000.

84. Gonczy, S. and N. Randall, "An ASTM Standard for Quantitative Scratch Adhesion Testing of Thin, Hard Ceramic Coatings", *Int. J. Appl. Ceram. Technol.*, Vol. 2, No. 5, pp. 422–428, 2005.

85. El-Rakayby, A. and B. Mills, *Wear*, Vol. 112, pp. 327–340, 1986.

86. Söderberg, S., *Proceedings of Fagersta High Speed Steel Symp.*, pp. 44–57, September 1981.

87. "Think HSS", http://www.lmttools.de-/rd_lmt/Dokumente_Global/Dokumente-LMT/IntroductionEN.pdf, 2007.

88. Van der Voort, G., *Metals Handbook*, chap. "Tool Steels", pp. 256–272, American Society for Metals, Metals Park, 1989.

89. Okolo, B., P. Lamparter, U. Welzel and E. Mittemeijer, "Stress, Texture, and Microstructure in Niobium Thin Films Sputter Deposited onto Amorphous Substrates", *Journal of Applied Physics*, Vol. 95, No. 2, January 2004.

90. R.D., A. and P. Kelly, "Recent advances in magnetron sputtering", *Surface and Coatings Technology*, Vol. 112, No. 1-3, pp. 170–176, 1999.

91. Güttler, D., B. Abendroth and W. Möller, "An Investigation of Target Poisoning During Reactive Magnetron Sputtering Using Ion Beam Analysis and Energy Resolved and Mass Spectroscopy", Websource http://www.uni-leipzig.de/iom/muehlleithen/2006/guettler_muehlleithen_06.pdf, April 2007.

92. Vossen, J. and W. E. Kern, *Thin Film Processes II*, Academic Press, London, 1991.

93. "Closed Field Unbalanced Magnetron Sputtering", http://www.teercoatings.-co.uk/index.php?page=cfubmsip, 2007.

94. Waibel, F. and M. Friz, "Coating Materials & Thin Film Deposition Techniques", Umicore Thin Film Products Technical Library: http://www.thinfilmproducts.umicore.com/library.asp?page=art1, 2006.

95. Bäcker, H., P. Henderson, J. Bradley and P. Kelly, "Time-resolved investigation of plasma parameters during deposition of Ti and $TiO_2$ thin films", *Surface and Coatings Technology*, Vol. 174-175, pp. 909–913, 2003.

96. Schiller, S., K. Goedicke, J. Reschke, V. Kirchoff, S. Schneider and F. Milde, *Surface and Coatings Technology*, Vol. 61, p. 331337, 1993.

97. Wong, M., W. Chia, P. Yashar, J. Schneider, W. Sproul and S. Barnett, *Surface and Coatings Technology*, Vol. 86/87, p. 381387, 1996.

98. Bülbül, F., *Darbeli-DC Manyetik Alanda Sıçrtama Yöntemi ile Kaplanan $TiB_2$ ve Me-DLC Filmlerin Mekanik, Yapısal ve Tribolojik Özelliklerinin Araştırılması*, Ph.D. thesis, Atatürk Üniversitesi Makina Mühendisliği Anabilim Dalı, 2006.

99. Movchan, B. and A. Demshishin, *Fiz. Met. Metalloved.*, Vol. 28, No. 653, 1969.

100. Thornton, J., "Structure and topography of sputtered coatings", *J. Vac. Sci. Technol.*, Vol. 11, No. 4, July/Aug. 1974.

101. Mummery, L., *Surface Texture Analysis-The Handbook*, Hommelwerke GmBH, 1 edn., 1992.

102. Sheeja, D., B. Tay, H. Lam and S. Ng, "Effect of Surface Roughness on the Adhesive and Tribological Characteristics of DLC Coating Prepared on Co-Cr-

Mo Alloy", *International Journal of Modern Physics B*, Vol. 16, No. 06-07, pp. 952–957, 2002.

103. Takadoum, J. and H. Bennani, "Influence of substrate roughness and coating thickness on adhesion, friction and wear of TiN films", *Surface and Coatings Technology*, Vol. 96, pp. 272–282, 1997.

104. Valli, J., *J. Vac. Sci. Technol. A4*, Vol. 6, p. 3007, 1986.

105. Steinmann, P., Y. Tardy and H. Hintermann, *Thin Solid Films*, Vol. 154, p. 333, 1987.

106. *"Applications Bulletin: The Influence of Surface Roughness on Instrumented Indentation Testing"*, Tech. Rep. 23, CSM Instruments Advanced Mechanical Surface Testing, CSM Instruments Rue de la Gare 4 CH-2034 Peseux Switzerland, March 2007.

107. Baglin, J., *Spectroscopic Analysis of Engineered Surfaces, Interfaces and Thin Layers*, Vol. 290 of *E: Applied Sciences*, pp. 111–149, Kluwer Academic Publishers, Chateau de Bonas, Gers, France, July 18-29 1994.

108. Sampson, A., *Scanning Electron Microscopy*, Tech. rep., Advanced Research Systems, http://www.sem.com/analytic/sem.htm, December 2 1996.

109. Boerma, D., *Spectroscopic Analysis of Engineered Surfaces, Interfaces and Thin Layers*, Vol. 290 of *E: Applied Sciences*, pp. 407–452, Kluwer Academic Publishers, Chateau de Bonas, Gers, France, July 18-29 1994.

110. Van der Voort, G. and H. James, *Metals Handbook*, chap. "Wrought Heat Resistant Alloys", pp. 305–312, American Society for Metals, Metals Park, 1989.

111. "Introduction to Auger Electron Spectroscopy (AES)", Websource: http://www.informaticus.org/nano/presentations/AES.ppt, November 1998.

112. Engelhard, M., *Tutorial on X-Ray Photoelectron Spectroscopy (XPS)*, U.S. Department of Energy, Pacific Northwest National Laboratory, 9/12/2002.

113. Lewis, G., "The Conservation of Photons", *Nature*, Vol. 118, p. 874, 1926.

114. Barr, T., *Modern ESCA The Principles and Practice of X-Ray Photoelectron Spectroscopy*, CRC Press, Boca Raton, Florida 33431, 1994.

115. Paik, N., "Raman and XPS studies of DLC films prepared by a magnetron sputter-type negative ion source", *Surface and Coatings Technology*, Vol. 200, pp. 2170–2174, 2005.

116. Shirley, D., *Phys. Rev.*, Vol. B, No. 5, p. 4709, 1972.

117. "POD-2 Tester", http://www.teercoatings.co.uk/index.php?page=pod1, 2007.

118. Holmberg, K. and A. Matthews, "Coatings Tribology", Elsevier, Amsterdam, 1998.

119. "CSM SCRATCH TESTERS: Nano, Micro and Macro range", Product Brochure, CSM Instruments Rue de la Gare 4 CH-2034 Peseux Switzerland, V.1, January 2006.

120. Fischer-Cripps, A., P. Karvankova and S. Veprek, "On the measurement of hardness of super-hard coatings", *Surface and Coatings Technology*, Vol. 200, pp. 5645–5654, 2006.

121. Kassavetis, S., S. Logothetidis and G. Matenoglou, *Surface and Coatings Technology*, Vol. 200, pp. 6400–6404, 2006.

122. Galvan, D., Y. Pei and J. D. Hosson, "Deformation and failure mechanism of nanocomposite coatings under nano-indentation", *Surface and Coatings Technology*, Vol. 200, pp. 6718–6726, 2006.

123. Hainsworth, S., M. McGurk and T. Page, "The effect of coating cracking on the indentation response of thin hard-coated systems", *Surface and Coatings Technology*, Vol. 102, pp. 97–107, 1998.

124. Cekada, M., M. Panjan, P. Panjan and D. Kek-Merl, "Microindentation depth profiling of selected hard coatings", *Surface and Coatings Technology*, Vol. 200, pp. 6554–6557, 2006.

125. Peggs, G. and I. Leigh, *Recommended procedure for micro-indentation Vickers hardness test*, Tech. Rep. Report MOM 62, UK National Physical Laboratory, 1983.

126. Chong, Y., *2003 SURE Report: Nanoindentation measurements of magnetron sputtered thin film*, Tech. rep., Materials Science and Engineering, Physics Department CUHK, 2003.

127. Oliver, W. and G. Pharr, *J. Mater. Res.*, Vol. 7, p. 1564, 1992.

128. Silva, T. D. and J. Moreira, *Phys. Rev., E Stat. Phys. Plasmas Fluids Relat. Interdiscip. Topics*, Vol. 56, p. 4880, 1997.

129. Baraba'si, A. and H. Stanley, *Fractal Concepts in Surface Growth*, Cambridge University Press, 1995.

130. Kardar, M., G. Parisi and Y. Zhang, *Phys. Rev. Lett.*, Vol. 56, p. 889, 1986.

131. Chowdhury, U., *MOCVD Growth for UV Photodetectors and Light Emitting Diodes*, Ph.D. thesis, The University of Texas at Austin, December 2002.

132. "A Practical Guide to Scanning Probe Microscopy", Websource: www.veeco.com/pdfs.php/166, 2007.

133. Garfunkel, E. and D. Potapenko, "Scanning Probe Microscopy: Atomic Force (AFM) and Scanning Tunneling Microscopy (STM)", Websource,

http://dft.rutgers.edu/lab/expts/STM/writeup.pdf, 22 March 2005.

134. "Elektrometal Kaplama Tekniği: Polisaj ve Parlatma", E-book: http://www.galvanoteknik.org/form/dosyalar/03.pdf, December 14 2006.

135. Ma, B., A. Tieu, C. Lu and Z. Jiang, "An experimental investigation of steel surface characteristic transfer by cold rolling", *Journal of Materials Processing Technology*, Vol. 125-126, pp. 657–663, 2002.

136. Poon, C. and B. Bhushan, "Nano-asperity contact analysis and surface optimization for magnetic head slider/disk contact", *Wear*, Vol. 202, pp. 83–89, 1996.

137. Paynter, R., "XPS Theory", http://csacs.mcgill.ca/francais/docs/CHEM634/XPS-_Paynter_t.pdf, 2007.

138. Glaude, A. S., L. Thomas, E. Tomasella, J. Badie and R. Berjoan, "Selective effect of ion/surface interaction in low frequency PACVD of SIC:H films: Part B. Microstructural study", *Surface and Coatings Technology*, Vol. 201, pp. 174–181, 2006.

139. "BE Lookup Table for Signals from Elements and Common Chemical Species", http://www.xpsdata.com/XI_BE_Lookup_table.pdf, May 2007.

140. Ismat, S., "Cleaning Windows: $TiO_2$ for Visible-Light Photodegradation of Pollutant", http://es.epa.gov/ncer/nano/lectures/shah92605.pdf, 26 Sep 2005.

141. Vasilets, V., A. Hirose, Q. Yang, A. Singh, R. Sammynaiken, M. Foursa and Y. Shulga, "Characterization of doped diamond-like carbon films deposited by hot wire plasma sputtering of graphite", *Applied Physics A*, Vol. 19, No. 8, pp. 2079–2084, 2004.

142. Yang, S., D. Camino, A. Jones and D. Teer, "Deposition and tribological behaviour of sputtered carbon hard coatings", *Surface and Coatings Technology*, Vol. 124, pp. 110–116, 2000.

143. Ulrich, S., H. Holleck, H. Leiste, L. Niederberger, E. Nold, K. Sell, M. Stüber, J. Yea, C. Ziebert, P. Pesch and S. Sattel, "Nano-scale, multi-functional coatings in the material system BCNH", *Surface and Coatings Technology*, Vol. 200, pp. 7–13, 2005.

144. Jafee, H. and K. Lawrence, "An investigation of the effect of surface roughness and coating thickness on the friction and wear behaviour of a commercial $MoS_2$-metal coating on AISI 400 C steel", *Wear*, Vol. 237, pp. 283–287, 2000.

145. Villiger, P., C. Sprecher and J. Peters, "Parameter optimisation of Ti-DLC coatings using statistically based methods", *Surface and Coatings Technology*, Vol. 116-119, pp. 585–590, 1999.

146. Sergici, A. and N. Randall, "Scratch Testing of Coatings", *Advanced Materials & Processes*, April 2006.

147. Herbert, E., G. Pharr, W. Oliver, B. Lucas and J. Hay, "On the measurement of stress–strain curves by spherical indentation", *Thin Solid Films*, Vol. 398-399, pp. 331–335, 2001.

148. Pei, Y., D. Galvan, J. D. Hosson and A. Cavaleiro, "Nanostructured TiC/a-C coatings for low friction and wear resistant applications", *Surface and Coatings Technology*, Vol. 198, pp. 44–50, 2005.

149. Leyland, A. and A. Metthews, *Surface and Coatings Technology*, Vol. 177-178, p. 317, 2004.

150. Zhou, F., K. Adachi and K. Kato, "Comparisons of tribological property of a-C, a-CNx and BCN coatings sliding against SiC balls in water", *Surface and Coatings Technology*, Vol. 200, pp. 4471–4478, 2006.

151. Pauschitz, A., A. Schalko, T. Koch, C. Eisenmenger-Sittner, S. Kvasnica and R. Manish, *Bull. Mater. Sci.*, Vol. 26, No. 6, pp. 585–591, October 2003.

152. Beake, B., V. Vishnyakov, R. Valizadeh and J. Colligon, "Influence of mechanical properties on the nanoscratch behaviour of hard nanocomposite TiN/Si3N coatings on Si", *J. Phys. D: Appl. Phys.*, Vol. 39, pp. 1392–1397, 2006.

153. Page, T. and S. Hainsworth, *Surface and Coatings Technology*, Vol. 61, pp. 201–208, 1993.

154. Hainsworth, S. and T. Page, *Mat. Res. Soc. Symp. Proc.*, Vol. 436, pp. 171–176, 1997.